

RADIATIVE PROPERTIES OF EMERGING MATERIALS AND  
RADIATION HEAT TRANSFER AT THE NANOSCALE

A Dissertation  
Presented to  
The Academic Faculty

By  
Ceji Fu

In Partial Fulfillment  
Of the Requirements for the Degree  
Doctor of Philosophy in the  
School of Mechanical Engineering

Georgia Institute of Technology  
November 2004

RADIATIVE PROPERTIES OF EMERGING MATERIALS AND  
RADIATION HEAT TRANSFER AT THE NANOSCALE

Approved by:

Dr. Zhuomin Zhang, Advisor  
*Woodruff School of Mechanical Engineering*

Dr. Peter J. Hesketh  
*Woodruff School of Mechanical Engineering*

Dr. William P. King  
*Woodruff School of Mechanical Engineering*

Dr. Phillip N. First  
*School of Physics*

Dr. David B. Tanner  
*Department of Physics, University of Florida*

Date Approved      November 11, 2004

## ACKNOWLEDGMENTS

I wish to express my genuine gratitude to my Ph.D. advisor, Professor Zhuomin Zhang, for offering me an opportunity to work in his lab and for his guidance in my research. In the past several years, his confidence and insight have helped me to grow not only in the technical arena, but also in personal attributes.

I would like to sincerely thank my Ph.D. committee members, Professors Peter Hesketh, William King, Phillip First, and David Tanner, for providing valuable suggestions on various aspects of my research and for reviewing this dissertation. I have learned Solid State Physics from Professors Tanner and First, and benefited greatly from their help and warm encouragement.

My heartfelt appreciation goes to all my former and current lab mates whom I have had the opportunity to interact and work with during my Ph.D. study. I especially want to thank Dr. Qunzhi Zhu for his continuous help in and beyond my research. Drs. Donghai Chen, Yihui Zhou, and Yu-jiun Shen offered me their friendly encouragements. I enjoyed the collaboration with Linxia Gu, Keunhan Park, and Bong Jae Lee. I also would like to thank Jorge Garcia, Yu-bin Chen, Hyunjin Lee, Vinh Khuu, and Jonathon Barletta for the pleasant interactions I had with them and for helping me improve my English.

I am deeply grateful to my parents, my wife, and my brother for the constant love and support they have provided me through all these years.

## TABLE OF CONTENTS

|   |     |
|---|-----|
| Acknowledgments   | iii |
| Table of Contents   | iv  |
| List of Tables  | vi  |
| List of Figures   | vii |
| List of Symbols and Abbreviations   | xi  |
| Summary   | xv  |
| Chapter 1 Introduction  | 1   |
| Chapter 2 Basic Theories  | 6   |
| 2.1 The Concept and Basic Optical Properties of an NIM  | 6   |
| 2.2 The Modified Matrix Formulation   | 13  |
| 2.3 The Mechanism of Photon Tunneling   | 17  |
| 2.4 Fundamentals of the Fluctuational Electrodynamics   | 19  |
| Chapter 3 Photon Tunneling in Multilayer Structures including Negative Index Materials                                | 26  |
| 3.1 The Case of Perfect Index Matching  | 27  |
| 3.2 A Non-Ideal Lossless NIM  | 30  |
| 3.3 The Effect of the NIM Layer on the Hemispherical Transmittance  | 37  |
| 3.4 Considering the Dispersion and Loss of an NIM   | 41  |
| 3.5 Employing NIMs in a Multilayer Structure of More than Four Layers   | 49  |
| Chapter 4 A Coherent Thermal Emission Source by Pairing a Layer of Negative $\epsilon$ with a Layer of Negative $\mu$ | 57  |

|  |     |
|--|-----|
| 4.1 Gratingless Coherent Thermal Emission Source   | 60  |
| 4.2 Surface Polariton Dispersion Relations at the Interface of the Bilayer   | 61  |
| 4.3 Predicted Results  | 64  |
| Chapter 5 The Brewster Angle with a Negative Index Material  | 73  |
| 5.1 The Brewster of a Lossless NIM   | 74  |
| 5.2 Physical Explanations Based on the Ewald-Oseen Extinction Theorem  | 82  |
| Chapter 6 Prediction and Optimization of Nanoscale Radiation Heat Transfer<br>Considering Different Doping Levels of Silicon | 91  |
| 6.1 The Dielectric Function of Silicon   | 92  |
| 6.2 Energy Density of Thermally Emitted EM Fields from a Flat Surface  | 98  |
| 6.3 Net Energy Flux between Silicon and Silicon  | 100 |
| 6.4 Net Energy Flux between Silicon and Silicon Carbide or Metal   | 110 |
| Chapter 7 Conclusions and Recommendations for Future Work  | 114 |
| References   | 118 |
| Vita   | 127 |

## LIST OF TABLES

|           |   |    |
|-----------|---|----|
| Table 2.1 | Conversion of values between angular frequency ( $\omega$ ) and frequency ( $\nu$ ), wave number ( $\eta$ ), and wavelength ( $\lambda$ ) | 25 |
| Table 3.1 | Comparison of the SPP frequencies $\omega_{spp}$ calculated from the dispersion relations with those obtained from the matrix formulation | 47 |

## LIST OF FIGURES

|            |  |    |
|------------|--|----|
| Figure 2.1 | Illustration of the directions of the vector $\mathbf{k}$ and energy flux $\mathbf{S}$ of an EM wave in (a) an NIM and (b) a PIM   | 8  |
| Figure 2.2 | Schematic of reflection and refraction at the interface of two media: (a) from a PIM to a PIM; (b) from a PIM to an NIM  | 10 |
| Figure 2.3 | An NIM slab of $n = -1$ acting as a lens: the distances $l_1, l_2$ and the NIM thickness $d$ satisfying $l_2 = d - l_1$  | 11 |
| Figure 2.4 | Schematic illustration of an $N$ -layer structure  | 14 |
| Figure 2.5 | Photon tunneling in a three-layer structure: (a) Schematic of the structure and (b) Transmittance by photon tunneling  | 18 |
| Figure 2.6 | Illustration of (a) thermal radiation from a body of temperature $T$ and (b) Coordinate system used in the problem of radiation heat transfer between two semi-infinite media                          | 20 |
| Figure 3.1 | Photon tunneling enhanced by an NIM layer: (a) Schematic of a four-layer structure and (b) The transmittance as a function of $(d_3 - d_2)/\lambda$ of the structure with optical parameters indicated | 28 |
| Figure 3.2 | The evanescent fields in media 2 and 3 (for $s$ -polarization): (a) $d_3 = d_2$ ; (b) $d_3 < d_2$ ; (c) $d_3 > d_2$  | 29 |
| Figure 3.3 | The polarized transmittance versus the incidence angle $\theta_1$ for $d_2/\lambda = 1, 2/3$ , and $1/2$ , where $n_3 = -0.99$ and $d_3 = d_2$   | 32 |
| Figure 3.4 | The polarized transmittance versus $d_3/d_2$ for $n_3 = -0.99, -0.98$ and $-0.95$ , where $d_2/\lambda = 1$ and $\theta_1 = 45^\circ$  | 33 |
| Figure 3.5 | $d_{3,\max}/d_2$ versus $n_3$ for different $d_2/\lambda$ and $\theta_1$ : (a) $s$ -polarization; (b) $p$ -polarization  | 35 |
| Figure 3.6 | The peak transmittance as a function of $n_3$ for different $d_2/\lambda$ and $\theta_1$ : (a) $s$ -polarization; (b) $p$ -polarization  | 36 |
| Figure 3.7 | The hemispherical transmittance of the layered structure versus $(d_3 - d_2)/\lambda$ with an NIM layer of $n_3 = -1$  | 38 |

|             |  |    |
|-------------|--|----|
| Figure 3.8  | The hemispherical transmittance of the layered structure, without the NIM layer, as a function of $d_2/\lambda$  | 39 |
| Figure 3.9  | The hemispherical transmittance versus $d_3/d_2$ for $n_3 = -0.99$ :<br>(a) $d_2/\lambda = 1$ ; (b) $d_2/\lambda = 1/2$  | 40 |
| Figure 3.10 | Refractive index $n$ and extinction coefficient $\kappa$ of a dispersive and dissipative NIM   | 42 |
| Figure 3.11 | Spectral transmittance of a four-layer structure at $45^\circ$ incidence angle: (a) $s$ -polarization; (b) $p$ -polarization   | 43 |
| Figure 3.12 | Dispersion curves of SPPs excited at the interface of a semi-infinite vacuum and a semi-infinite NIM   | 45 |
| Figure 3.13 | Peak transmittance of the 4-layer structure versus the thickness of the NIM: (a) $s$ -polarization; (b) $p$ -polarization  | 48 |
| Figure 3.14 | The transmittance spectra of a 5-layer structure for $\gamma = 0.0025\omega_p$ : in (a) and (b), the vacuum gap (VG) is equally divided into two layers sandwiching the NIM layer; in (c) and (d), the NIM layer is equally divided into two layers that sandwich the VG | 50 |
| Figure 3.15 | The transmittance of multilayer structures with different numbers of layers: (a) $s$ -polarization, (b) $p$ -polarization  | 53 |
| Figure 3.16 | The transmittance and absorptance of multilayer structures: (a) $s$ -polarization, (b) $p$ -polarization   | 55 |
| Figure 4.1  | Coherent thermal emission from a SiC grating: (a) the grating geometry, (b) measured directional spectral emissivity at three wavelengths (from Greffet et al., 2002)  | 59 |
| Figure 4.2  | A coherent thermal emission source: (a) schematic of the source, (b) the dispersion relations of surface polaritons  | 63 |
| Figure 4.3  | The directional spectral emissivity $\varepsilon_\omega$ of the bilayer structure for $s$ -polarization  | 66 |
| Figure 4.4  | The directional spectral emissivity $\varepsilon_\omega$ of the bilayer structure for $p$ -polarization  | 67 |
| Figure 4.5  | The dispersion curves of a three-layer structure of $p$ -polarization, where the negative $\mu$ layer is sandwiched by two negative $\varepsilon$ layers   | 70 |



|            |   |     |
|------------|---|-----|
| Figure 4.6 | The directional spectral emissivity $\varepsilon_\omega$ of the three-layer structure for $p$ -polarization   | 71  |
| Figure 5.1 | The regime map for the Brewster angle of a lossless NIM   | 78  |
| Figure 5.2 | The reflectance $R$ at the interface of vacuum and an NIM: The four panels correspond to the four regimes in the regime map   | 79  |
| Figure 5.3 | Contour plot with curves of constant Brewster angle in the $X$ - $Y$ plane  | 81  |
| Figure 5.4 | Emitted electric field amplitudes for a TM wave incident from vacuum into a dielectric: (a) $\varepsilon_2 = 4$ and $\mu_2 = 1$ ; (b) $\varepsilon_2 = 8$ and $\mu_2 = 0.5$       | 87  |
| Figure 5.5 | Emitted electric field amplitudes for a TM wave incident from vacuum into a lossless NIM: (a) $\varepsilon_2 = -4$ and $\mu_2 = -1$ ; (b) $\varepsilon_2 = -8$ and $\mu_2 = -0.5$ | 88  |
| Figure 5.6 | Emitted electric field amplitudes for a TM wave incident from vacuum into a lossless NIM with $\varepsilon_2 = -0.125$ and $\mu_2 = -2$   | 89  |
| Figure 6.1 | The electron scattering time of silicon changes with temperature and dopant concentration   | 96  |
| Figure 6.2 | The absorption coefficient of (a) intrinsic and (b) doped silicon   | 97  |
| Figure 6.3 | The energy density emitted from a silicon surface of 1000 K at different heights above the surface  | 98  |
| Figure 6.4 | Estimated density of modes for $z = 10$ nm above the surface of an intrinsic silicon and an n-type silicon at 1000 K  | 100 |
| Figure 6.5 | The energy flux between two semi-infinite intrinsic silicon media: (a) the net spectral energy flux (b) the net total energy flux   | 102 |
| Figure 6.6 | The effect of doping on the net (a) spectral energy density and (b) total energy density between the two silicon media  | 103 |
| Figure 6.7 | The change of the (a) real part and (b) imaginary part of the dielectric function of silicon at different temperatures  | 106 |
| Figure 6.8 | The parameter $\Phi$ drawn as a function of $\omega$ for different dopant concentrations of silicon   | 107 |

|             |   |     |
|-------------|---|-----|
| Figure 6.9  | Net energy flux obtained for small $d$ with both media being n-type silicon with dopant concentration between $10^{20}$ and $10^{21} \text{ cm}^{-3}$ | 108 |
| Figure 6.10 | The effect of temperature on the radiation energy flux between two doped silicon  | 109 |
| Figure 6.11 | The net (a) spectral energy flux and (b) total energy flux between silicon and silicon carbide  | 111 |
| Figure 6.12 | The net total energy flux between silicon and aluminum  | 113 |

## LIST OF SYMBOLS AND ABBREVIATIONS

|                         |   |   |
|-------------------------|---|---|
| $c$                     | = | speed of light in vacuum, $2.998 \times 10^8$ m/s   |
| $d$                     | = | layer thickness, m  |
| $\mathbf{E}$            | = | electric field vector, V/m  |
| $e$                     | = | electron charge, $1.602 \times 10^{-19}$ C  |
| $F$                     | = | fractional area of the unit cell occupied by the split ring                                 |
| $\overline{\mathbf{G}}$ | = | dyadic Green function, 1/m  |
| $\mathbf{H}$            | = | magnetic field vector, A/m  |
| $i$                     | = | $\sqrt{-1}$   |
| $\mathbf{j}$            | = | fluctuating electric current density, A/m <sup>2</sup>                                      |
| $\mathbf{K}$            | = | parallel wave vector component , 1/m  |
| $\mathbf{k}$            | = | wave vector, 1/m  |
| $k_B$                   | = | Boltzmann constant, $1.38 \times 10^{-23}$ J/K  |
| $k_x$                   | = | wave vector component in the $x$ -direction, 1/m  |
| $k_{SP}$                | = | wavevector of surface polaritons, 1/m   |
| $k_z$                   | = | wave vector component in the $z$ -direction, 1/m  |
| $\mathbf{M}$            | = | transfer matrix or magnetization vector (A/m)   |
| $m$                     | = | effective mass, kg  |
| $m_0$                   | = | electron rest mass, $9.109 \times 10^{-31}$ kg  |
| $N$                     | = | free carrier/dopant concentration or density of states, cm <sup>-3</sup> or m <sup>-3</sup> |

|                |   |   |
|----------------|---|---|
| NIM            | = | negative index material                               |
| $n$            | = | real part of $\tilde{n}$                              |
| $\tilde{n}$    | = | complex refractive index                              |
| $\mathbf{P}$   | = | propagation matrix or polarization vector ( $C/m^2$ ) |
| PIM            | = | positive index material                               |
| Q              | = | Q factor of a coherent thermal emission               |
| $q''_{net}$    | = | net energy flux, $W/m^2$                              |
| $q''_{\omega}$ | = | spectral energy flux, $J/m^2 \cdot rad$               |
| $R$            | = | reflectance   |
| $r$            | = | reflection coefficient                                |
| $\mathbf{S}$   | = | Poynting vector, $J/s$                                |
| SPP            | = | surface plasmon polariton                             |
| $T$            | = | temperature or transmittance                          |
| $t$            | = | transmission coefficient or time (s)                  |
| $u$            | = | spectral energy density, $J \cdot s/m^3 \cdot rad$    |
| VG             | = | vacuum gap  |

#### Greek Symbols

|          |   |   |
|----------|---|---|
| $\Theta$ | = | mean energy of an oscillator, J           |
| $\Pi_e$  | = | the first Hertz vector ( $V \cdot m^2$ )  |
| $\Pi_e$  | = | the second Hertz vector ( $A \cdot m^2$ ) |
| $\alpha$ | = | absorption coefficient, $1/m$             |
| $\beta$  | = | evanescent wave decaying factor, $1/m$    |

|                   |   |   |
|-------------------|---|---|
| $\chi$            | = | susceptibility  |
| $\epsilon$        | = | relative (electric) permittivity or dielectric function                           |
| $\epsilon_0$      | = | permittivity of vacuum, $8.854 \times 10^{-12}$ F/m                               |
| $\epsilon_\omega$ | = | directional spectral emissivity   |
| $\gamma$          | = | damping term, rad/s   |
| $\kappa$          | = | imaginary part of $\tilde{n}$   |
| $\lambda$         | = | wavelength, m   |
| $\lambda_p$       | = | wavelength corresponding to the plasma frequency, m                               |
| $\mu$             | = | relative (magnetic) permeability  |
| $\mu_0$           | = | permeability of vacuum, $4\pi \times 10^{-7}$ H/m                                 |
| $\theta$          | = | angle, degree   |
| $\sigma$          | = | Stefan-Boltzmann constant, $5.67 \times 10^{-8}$ W/m <sup>2</sup> ·K <sup>4</sup> |
| $\tau$            | = | carrier scattering time, s  |
| $\omega$          | = | angular frequency, rad/s  |
| $\omega_0$        | = | resonance frequency, rad/s  |
| $\omega_c$        | = | center frequency of narrow emission band, rad/s                                   |
| $\omega_p$        | = | plasma frequency, rad/s   |
| $\omega_{spp}$    | = | surface plasmon polariton resonance frequency, rad/s                              |
| $\Delta\omega$    | = | full width at half maximum of narrow emission band, rad/s                         |

#### Subscripts

$A$  = acceptor

|        |   |                      |
|--------|---|----------------------|
| $D$    | = | donor                |
| $d$    | = | defect               |
| $e$    | = | electron or electric |
| $evan$ | = | evanescent mode      |
| $h$    | = | hole                 |
| $l$    | = | lattice              |
| $p$    | = | $p$ -polarization    |
| $prop$ | = | propagating mode     |
| $m$    | = | magnetic             |
| $s$    | = | $s$ -polarization    |

#### Superscripts

|     |   |                   |
|-----|---|-------------------|
| $p$ | = | $p$ -polarization |
| $s$ | = | $s$ -polarization |

## SUMMARY

A negative index material (NIM), which possesses simultaneously a negative permeability and a negative permittivity, is an emerging material that has caught the attention of many scientists and engineers after it was first demonstrated in 2001. It has been shown that NIMs have some remarkable properties such as a negative phase velocity and negative refraction and hold enormous promise for applications such as perfect lens and optical communications. This dissertation is centered on investigating the unique aspects of the radiative properties of negative index materials (NIMs). Photon tunneling, which relies on evanescent waves to transfer radiation energy, has important applications for radiative transfer in thin-film structures, microscale thermophotovoltaic devices, and scanning thermal microscopes. With multilayer thin-film structures, photon tunneling is shown to be greatly enhanced by using NIM layers. The enhancement is attributed to the excitation of surface or bulk polaritons, which depends on the thicknesses of the NIM layers according to the phase matching condition. A new kind of coherent thermal emission source is proposed by pairing a negative permittivity (but positive permeability) layer with a negative permeability (but positive permittivity) layer. The merits of such a coherent thermal emission source are that coherent thermal emission occurs not only for  $p$ -polarization, but also for  $s$ -polarization, without the use of grating structures. By analyzing the polariton dispersion relation, a method for control of the emission frequency and emission angle is provided. The power reflectance from NIM can be zero for both polarizations, that is, there exist Brewster angles for both polarizations under certain conditions. The criteria for zero reflectance or the Brewster angle are

determined analytically and presented in a regime map. The findings on the unique radiative properties of NIMs may help develop advanced energy conversion devices. Motivated by the recent advancement in scanning probe microscopy, the last part of this dissertation focuses on the prediction of the radiation heat transfer between two closely spaced semi-infinite media. The objective is to investigate the dopant concentration of silicon on the near-field radiation heat transfer. It is found that the radiative energy flux can be significantly augmented by using heavily doped silicon for the two media separated at nanometric distances. Large enhancement of radiation heat transfer at the nanoscale may have an impact on the development of near-field thermal probing and nanomanufacturing techniques.



# CHAPTER 1

## INTRODUCTION

The experimental demonstration (Shelby et al., 2001) of negative refraction using a metamaterial has resulted in a surge of interest in the study of negative index materials (NIMs) whose refractive index is negative ( $n < 0$ ) in certain spectral region. The concept of negative refractive index was first postulated by Veselago (1968) for a hypothetical material having simultaneously a negative electric permittivity  $\epsilon$  and a negative magnetic permeability  $\mu$ . However, the fact that a negative  $\mu$  is never found in naturally occurring materials hinders any practical considerations of an NIM for some 30 years. Pendry et al. (1996 and 1999) suggested the construction of metamaterials using periodic unit structures, which can be appropriately designed to have desired electric and magnetic responses. For example, split-ring resonators can be used to achieve a negative  $\mu$  and thin metallic wire structures can be used to achieve a negative  $\epsilon$  with a plasma frequency much lower than that of a typical metal. By tuning the structure parameters, Shelby et al. (2001) first demonstrated experimentally the existence of a negative refractive index at X-band microwave frequencies in a metamaterial made of repeated unit cells of interlocking copper wires and split-ring resonators. Several alternative approaches have been proposed, including the use of photonic crystals (Notomi, 2000; Gralak et al., 2000; Luo et al., 2002) and nanowire pairs (Podolskiy et al., 2002), for development of NIMs in the infrared or higher frequency regions. A recent study (Yen et al., 2004) scaled down the split-ring resonators to observe a negative  $\mu$  behavior at 0.8 – 1.2 THz (375 – 250  $\mu\text{m}$

wavelength). These studies open the door for potential realization of NIMs in the infrared and visible regions someday.

The main reason of studying NIMs is because these materials possess many unique optical properties and, if successfully constructed, will have enormous applications in imaging, lithography, and optical communications. The phase velocity of an electromagnetic (EM) wave in an NIM medium is opposite to its energy flux, resulting in a reversed Doppler effect. Light refracted from a conventional positive index material (PIM) into an NIM will bend to the same side of the surface normal as the incident beam (a phenomenon called negative refraction) and a flat slab of NIM can focus light (Veselago, 1968). Pendry (2000) showed that an NIM slab with  $\epsilon = \mu = -1$  ( $\epsilon$  and  $\mu$  are the relative values with respect to those of free space) performs the dual function of correcting the phase of the propagating components and amplifying the evanescent components, which normally exist only in the near field of the object. The combined effects could make a perfect lens that eliminates the limitation on image resolution imposed by diffraction for conventional lenses. Other potential applications range from novel Bragg reflectors (Gerardin and Lakhtakia, 2002) to phase-compensated cavity resonators (Engheta, 2002), forward couplers in transmission lines (Liu et al., 2002), and waveguides (Qing and Chen, 2004b).

As an emerging material, many other important properties and potential applications of an NIM remain unexploited. One of the objectives of this dissertation is to explore some properties and applications of NIMs related to radiation heat transfer. Photon tunneling, which relies on evanescent waves to transfer energy between an emitter and a receiver, has important applications in photon scanning tunneling

microscopy (Reddick et al., 1989; Shen et al., 2000) and in micro/nanoscale radiation heat transfer (Pendry, 1999; Whale and Cravalho, 2002; Narayanaswamy and Chen, 2003). In order for photon tunneling to be significant, the emitter and the receiver must be brought in close proximity to each other because evanescent waves exhibit the characteristic of exponential decay. If an NIM slab can amplify evanescent waves as shown by Pendry (2000), one may ask whether an NIM slab can be used to enhance photon tunneling. A nonmagnetic material that supports surface polaritons can have higher spectral, directional emissivity ( $p$ -polarized) if a grating is etched on the surface of the material (Hesketh et al., 1986 and 1988; Greffet et al., 2002; Kreiter, 1999). This is due to the coupling of surface polaritons with thermal radiation by the grating. Thermal emission from such a source exhibits coherent properties and may have potential applications in “radiative cooling” and in infrared photovoltaic devices (Greffet et al., 2002). Using negative  $\mu$  materials, is it possible to build a coherent thermal emission source of both  $s$ - and  $p$ -polarizations without gratings? The unique property of Brewster’s angle has been applied in many devices such as polarizers (Kaplan and Hanssen, 1999; Sihvola and Lindell, 1993) and transmission windows (Yang et al., 2003). In an NIM, one may wonder what criterion Brewster’s angle obeys. All these questions will be extensively addressed in this dissertation.

A relevant topic studied in this dissertation is on the nanoscale radiation heat transfer between closely spaced surfaces, especially with doped silicon. Radiation heat transfer at the nanoscale can achieve a much higher energy flux by photon tunneling than that predicted from the Stefan-Boltzmann law. Therefore, it has important applications in nanoscale energy conversion devices (Whale and Cravalho, 2002; Narayanaswamy and

Chen, 2003) and in near-field scanning thermal microscopy (Williams and Wickramasinghe, 1986; Xu et al., 1994; Müller-Hirsch et al., 1999; Pendry, 1999). Most of the theoretical work has been performed on the prediction of the net heat flux between two parallel metallic plates using a DC conductivity in a Drude model for the materials' dielectric function (Polder and Van Hove, 1971; Caren, 1974; Loomis and Maris, 1994; Pendry, 1999). Nanoscale radiation heat transfer between non-metallic materials has also been studied (Whale and Cravalho, 2002; Mulet et al., 2002; Narayanaswamy and Chen, 2003). Nevertheless, little work has investigated the problem of nanoscale radiation heat transfer when silicon is involved.

The interest in studying nanoscale radiation heat transfer with silicon emerges because silicon is the most extensively used material in MEMS/NEMS and many other microelectronic devices. Radiation heat transfer in these devices may be important when their characteristic dimensions are on nanoscale levels. More importantly, the development of atomic force microscope (AFM) cantilevers with integrated heaters and tips with nanoscale sharpness made of silicon (King et al., 2001) can be used to study radiative energy exchange between two objects separated by a vacuum gap from 10 nm to 1 nm. The heated AFM cantilever tip can control the temperature of a highly local source in controlled close proximity to a temperature sensor. This allows direct measurements of the net heat transfer between the tip and the temperature sensor. Nanoscale radiation heat transfer between two objects strongly depends on the optical properties of the materials. Because the optical properties of silicon are functions of temperature and dopant concentration, it is imperative to study the dependence of the net heat flux of the optical properties of silicon at different dopant concentrations and temperatures. Furthermore, an

optimized dopant concentration may exist that will yield the largest net heat flux for prescribed emitter and receiver temperatures. The theoretical understanding gained from this research will facilitate the design of experiments that utilize near-field heat transfer to enhance heating or cooling at the nanoscale.

The organization of this dissertation is as follows. Chapter 2 presents some basic theories on which the work in subsequent chapters is based, including the concept and basic optical properties of an NIM, the matrix formulation for calculating the radiative properties of layered structures, the mechanism of photon tunneling, and the fundamentals of the fluctuational electrodynamics. In Chapter 3, enhancement of photon tunneling using layers of an NIM is studied, considering different cases such as the perfect index matching case, a non-ideal and lossless NIM, and a dispersive and lossy NIM in different arrangements of multilayer structures. A coherent thermal emission source is proposed in Chapter 4. It is constructed using a layer having a negative permittivity but a positive permeability paired with a layer having a positive permittivity but a negative permeability. Conditions for coherent thermal emission and a method for easy control of the emission wavelength and emission angle are discussed. In Chapter 5, the Brewster angle involving NIMs is examined. The criteria for the Brewster angle are determined analytically and presented in a regime map. The prediction of the radiation heat transfer between two semi-infinite media separated at nanometric distances, at least one of which is silicon, is presented in Chapter 6. The effect of dopant concentration in silicon on the energy flux is emphasized. Finally, Chapter 7 summarizes the conclusions and the recommended future work.

## CHAPTER 2

### BASIC THEORIES

This chapter presents a summary of the basic theories to be used in subsequent chapters. The optical properties of NIMs are described. The modified matrix formulation is then provided for the calculation of radiative properties of multilayers, including both PIMs and NIMs. The mechanism of photon tunneling and its applications are explained, because it is the key to near-field radiation heat transfer. The fundamentals of the fluctuational electrodynamics are presented that will be used to compute the nanoscale radiation heat transfer in Chapter 6.

#### **2.1. The Concept and Basic Optical Properties of an NIM**

A negative index material (NIM) is a material that has a negative refractive index ( $n < 0$ ). A negative  $n$  was first postulated by Veselago (1968) for a hypothetical material having a negative electric permittivity  $\epsilon$  and negative magnetic permeability  $\mu$ . It was found that electromagnetic (EM) waves can propagate in such a medium, but in a very unique way. The phase velocity of an EM wave is opposite to its energy flux. This particular behavior can be demonstrated from Maxwell's equations. For a plane wave propagating in an NIM, the following two relations should be satisfied according to the two Maxwell's curl equations (Yeh, 1988)

$$\mathbf{k} \times \mathbf{E} = \omega \mu \mu_0 \mathbf{H} \quad (2.1)$$

and 
$$\mathbf{k} \times \mathbf{H} = -\omega \epsilon \epsilon_0 \mathbf{E} \quad (2.2)$$

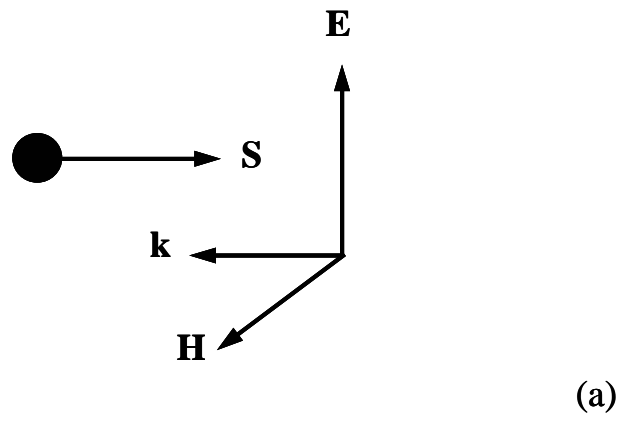
where  $\mathbf{E}$  is the electric field,  $\mathbf{H}$  the magnetic field,  $\mathbf{k}$  the wavevector,  $\varepsilon$  and  $\mu$  the relative electric permittivity and relative magnetic permeability of the NIM, and  $\varepsilon_0$  and  $\mu_0$  the absolute electric permittivity and absolute magnetic permeability of vacuum, respectively. Because both  $\varepsilon_0$  and  $\mu_0$  are positive, the vectors  $\mathbf{E}$ ,  $\mathbf{H}$  and  $\mathbf{k}$  will form a left-handed triplet if  $\varepsilon$  and  $\mu$  are both negative whilst in a conventional positive index material (PIM) with both positive  $\varepsilon$  and  $\mu$ , the three vectors form a right-handed triplet. The energy flux of the EM wave is given by the time-averaged Poynting vector

$$\mathbf{S} = \frac{1}{2} \text{Re}(\mathbf{E} \times \mathbf{H}^*) \quad (2.3)$$

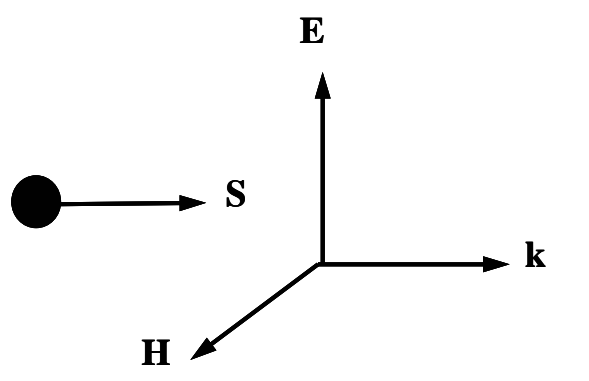
where  $\text{Re}$  takes the real part of  $\mathbf{E} \times \mathbf{H}^*$ , and the asterisk denotes the complex conjugate. Because  $\varepsilon$  and  $\mu$  are not involved in Equation (2.3),  $\mathbf{E}$ ,  $\mathbf{H}$ , and  $\mathbf{S}$  always form a right-handed triplet regardless of the signs of  $\varepsilon$  and  $\mu$ . Note that the wavevector  $\mathbf{k}$  represents the EM wave's phase velocity propagation direction. Therefore, the EM wave's phase velocity is opposite to its energy flux in an NIM while the phase velocity is in the same direction as the energy flux in a PIM, which is schematically shown in Figure 2.1. The opposite phase velocity of an EM wave with respect to its energy flux will result in the Doppler Effect and the Cerenkov Effect being reversed (Veselago, 1968). Note that Figure 2.1 also provides a simple way to understand the negative  $n$  in an NIM. The wavevector  $\mathbf{k}$  with respect to the direction  $\mathbf{S}$  can be written as

$$\mathbf{k} = \pm \frac{\omega}{c} \sqrt{\varepsilon\mu} \hat{\mathbf{s}} = \frac{\omega}{c} n \hat{\mathbf{s}} \quad (2.4)$$

where  $\omega$  denotes the angular frequency and  $c$  the speed of light in vacuum;  $\hat{\mathbf{s}}$  is a unit vector representing the director of  $\mathbf{S}$ . Because the wavevector  $\mathbf{k}$  in an NIM is opposite to



(a)



(b)

Figure 2.1 Illustration of the directions of the vector  $\mathbf{k}$  and energy flux  $\mathbf{S}$  of an EM wave in (a) an NIM and (b) a PIM.



$\hat{\mathbf{s}}$ , the refractive index  $n$  must be taken as the *negative square root of the product of  $\epsilon\mu$* , i.e.,  $n = -\sqrt{\epsilon\mu}$ . On the contrary,  $\mathbf{k}$  in a PIM is along with  $\hat{\mathbf{s}}$ , the refractive index  $n$  must be taken as the *positive square root of the product of  $\epsilon\mu$* , that is,  $n = +\sqrt{\epsilon\mu}$ .

Another particular behavior of an NIM happens when a beam is incident from a PIM onto an NIM (or vice versa). The refracted beam in the second medium will bend to the same side of the surface normal as the incident beam, a phenomenon called the negative refraction (Veselago, 1968; Shelby et al., 2001). Because the boundary conditions at the interface require that the parallel components of  $\mathbf{E}$  and  $\mathbf{H}$ , and the normal components of  $\epsilon\mathbf{E}$  and  $\mu\mathbf{H}$  be continuous across the interface, the parallel component of wavevector  $\mathbf{k}$  conserves in both media while its normal component changes sign when the passage of a beam is from a PIM to an NIM. These differences, as compared with the case of a beam incident from a PIM onto a PIM, are clearly illustrated in Figure 2.2, where  $\theta_1$  and  $\theta_2$  are called the incidence angle and the refraction angle, respectively (only the case of  $p$ -polarization is shown, the same phenomenon holds for  $s$ -polarization). Furthermore, in order for Snell's law to hold in the same form as  $n_1 \sin \theta_1 = n_2 \sin \theta_2$  for both the cases shown in Figures 2.2(a) and 2.2(b),  $\theta_2$  in Figure 2.2(b) has to be taken as a negative value.

An important application of the negative refraction phenomenon is the imaging capability of an NIM slab, which is demonstrated in Figure 2.3. Assume an NIM slab of  $n = -1$  and thickness  $d$  is placed in vacuum. An object that is located at a distance of  $l_1$  in front of the first surface of the NIM slab is possible to have an image at a distance  $l_2$  behind the second surface of the NIM as long as  $l_1$ ,  $l_2$ , and  $d$  satisfy the relation  $l_2 = d - l_1$ . Therefore, negative refraction makes the NIM slab act as a lens to focus light emitted at

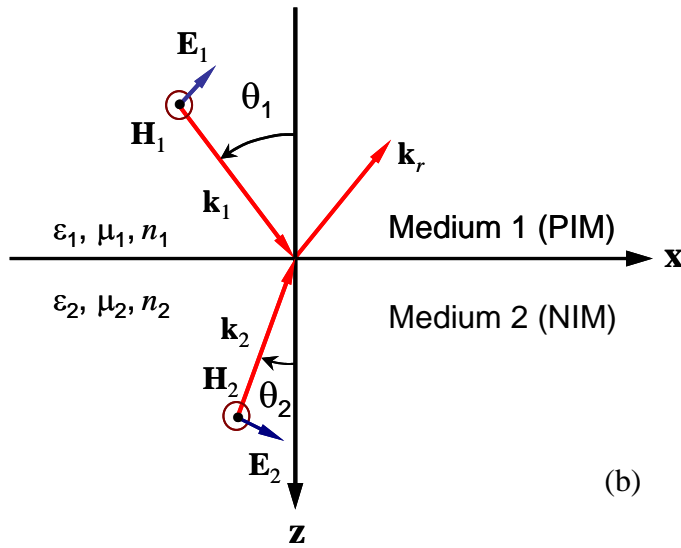
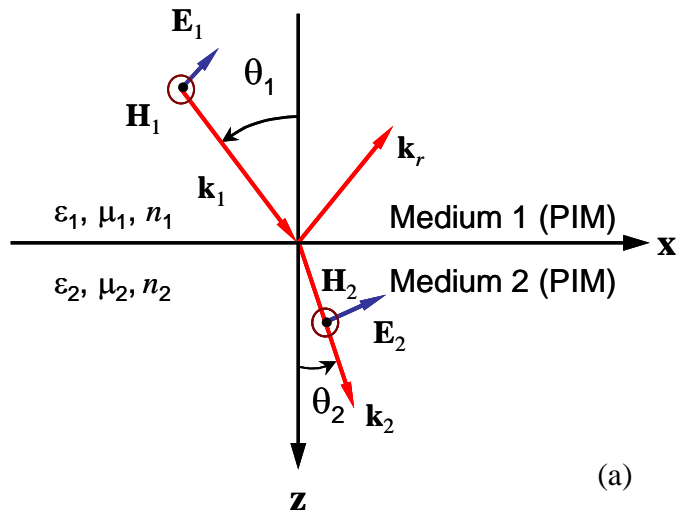


Figure 2.2 Schematic of reflection and refraction at the interface of two semi-infinite media: (a) from a PIM to a PIM; (b) from a PIM to an NIM. In (b), the refracted wavevector points opposite to the direction of energy flux. The incidence is for  $p$ -polarization and the positive sense for all angles is counter-clockwise.

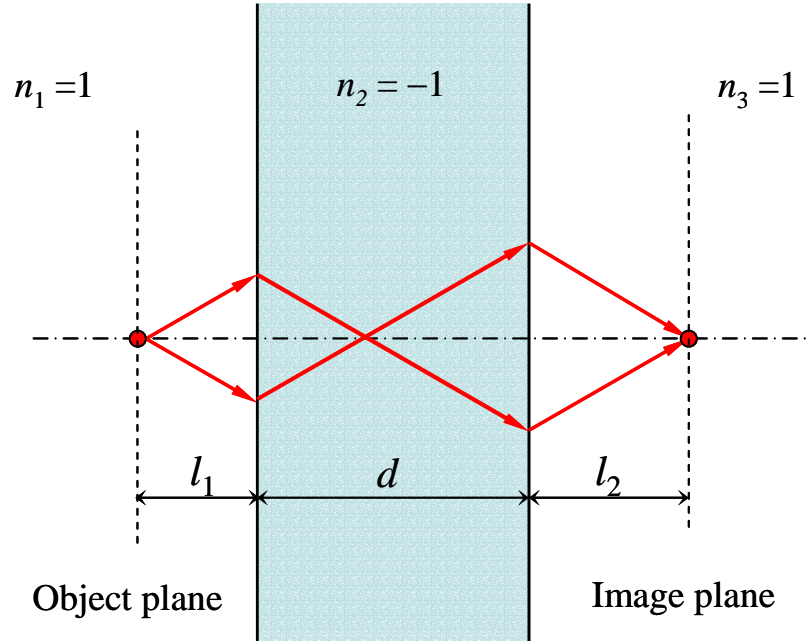


Figure 2.3 An NIM slab of  $n = -1$  serving as a lens: the distances  $l_1$ ,  $l_2$  and the NIM thickness  $d$  satisfy  $l_2 = d - l_1$ .

the object plane to the image plane. Pendry (2000) further showed that such a lens is a perfect lens because it eliminates the limitations on image resolution imposed by diffraction for conventional lenses. It should be noted that despite doubt cast by some researchers on the concept of a “perfect lens” (Garcia and Nieto-Vesperinas, 2002) and even on negative refraction (Valanju et al., 2002), both hypotheses of negative refraction and the ability to focus light by a slab of NIM have been verified by analytical (Ziolkowski and Heyman, 2001; Zhang and Park, 2004), numerical (Smith and Schultz, 2002; Markoš and Soukoulis, 2002; Pacheco et al., 2002) and experimental methods (Houck et al., 2003; Parazzoli et al., 2003; Cubukcu et al., 2003). Other unique phenomena that result from negative refraction include multiple images (Pokrovsky and

Efros, 2003), a negative beam shift upon reflection (Kong et al., 2002) and a negative Goos-Hänchen shift upon total internal reflection (Berman, 2002; Lakhtakia, 2003; Qing and Chen, 2004a).

The basic optical properties discussed above are only for a lossless NIM and the frequency-dependence of  $\varepsilon$  and  $\mu$  was not considered. However, it has been shown that  $\varepsilon$  and  $\mu$  of an NIM must be inherently dependent on frequency (Veselago, 1968; Smith and Kroll, 2000). For a metamaterial of negative refractive index built with metallic meshes and split-ring resonators, it is been shown that the relative permittivity and permeability of the metamaterial can be expressed as functions of the angular frequency  $\omega$  as follows (Pendry et al., 1996 and 1999):

$$\varepsilon(\omega) = 1 - \frac{\omega_p^2}{\omega^2 + i\gamma_e\omega} \quad (2.5)$$

and

$$\mu(\omega) = 1 - \frac{F\omega^2}{\omega^2 - \omega_0^2 + i\gamma_m\omega} \quad (2.6)$$

where  $\omega_p$  is the effective plasma frequency,  $\omega_0$  is the effective resonance frequency,  $\gamma_e$  and  $\gamma_m$  are the damping terms, and  $F$  is the fractional area of the unit cell occupied by the split ring. From Equations (2.5) and (2.6), both negative  $\varepsilon$  and  $\mu$  are realized within a frequency range between  $\omega_0$  and  $\omega_p$  for an adequately small  $\gamma_e$  and  $\gamma_m$ . Here, the values of  $\omega_0$ ,  $\omega_p$ ,  $\gamma_e$ ,  $\gamma_m$  and  $F$  depend on the geometry of the unit cell that constructs the metamaterial. Therefore, the metamaterial is both dispersive and dissipative. The refractive index will be complex for a dissipative medium, which is generally determined from the following relation

$$\tilde{n}^2(\omega) = [n(\omega) + i\kappa(\omega)]^2 = \varepsilon(\omega)\mu(\omega) \quad (2.7)$$

Here,  $n(\omega)$  is the real part of the complex refractive index  $\tilde{n}(\omega)$ ,  $\kappa(\omega)$  is called the extinction coefficient and must not be less than zero for any passive medium imposed by the principle of causality (Born and Wolf, 1999). Equation (2.7) used to calculate  $\tilde{n}(\omega)$  of a dissipative NIM will result in a negative  $n(\omega)$  and a positive  $\kappa(\omega)$ . Such a complex refractive index can still be used in Equation (2.4) and explained by Figure 2.1(a). The positive  $\kappa(\omega)$  explains energy loss of an EM wave along its energy flux direction  $\hat{s}$  while the negative  $n(\omega)$  account for the reversed phase velocity with respect to  $\hat{s}$ .

## 2.2 The Modified Matrix Formulation

Multilayer thin-film structures will be studied in this thesis and the matrix formulation is a standard and convenient tool for calculating the radiative properties of multilayer structures (Born and Wolf, 1999; Yeh, 1988; Kong, 1990; Zhang et al., 2003). A complete derivation of the matrix formulation needs to be shown in order to clearly see the essence of this method. Furthermore, some modifications are necessary for the matrix formulation to be applicable to absorbing media and with NIMs. Even in some recent publications involving NIMs (Gerardin and Lakhtakia, 2002; Zhang and Fu, 2002; Fu and Zhang, 2003; Ramakrishna et al., 2003; Gao and Tang, 2004), the equations were either not provided or given under restricted conditions. Therefore, a modified matrix formulation that is applicable to more general conditions is described in this section.

A multilayer structure containing  $N$  layers is shown in Figure 2.4. Each layer is assumed isotropic and homogeneous and can be fully described by a relative permittivity  $\varepsilon_l$  and a relative permeability  $\mu_l$  ( $l = 1, 2, \dots, N$ ). For a monochromatic plane wave

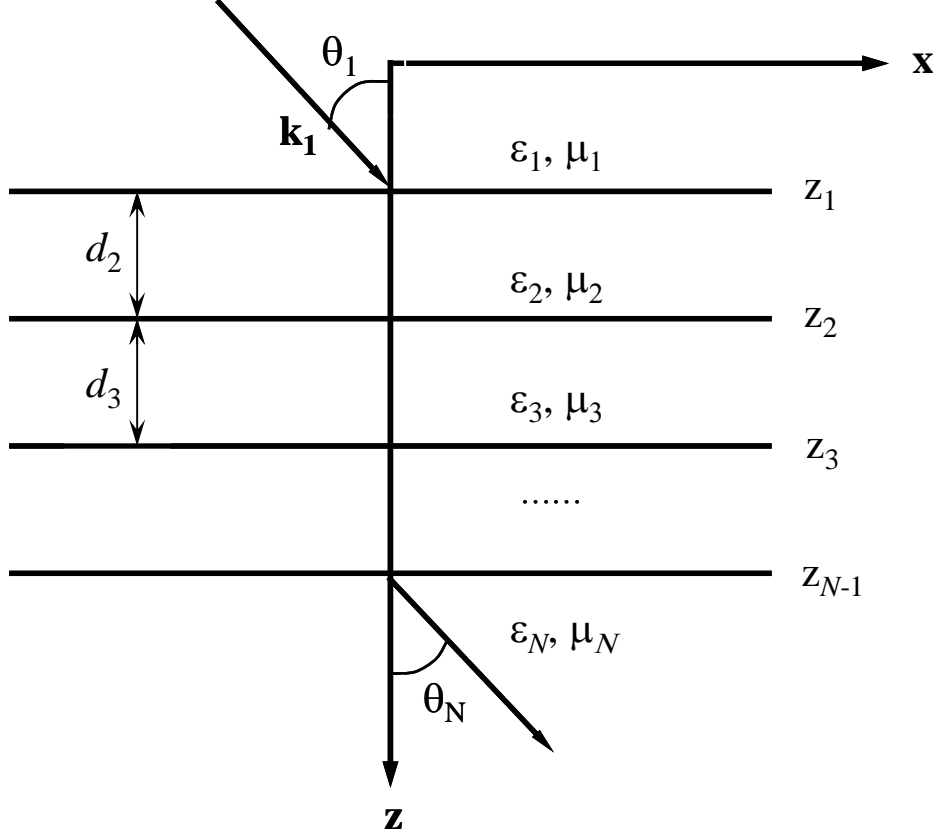


Figure 2.4 Schematic illustration of an  $N$ -layer structure.

originating from layer 1, which is assumed to be lossless, phase matching condition requires that  $k_{lx} \equiv k_x = \omega n_1 \sin \theta_1 / c$  where  $\omega$  is the wave angular frequency,  $n_1$  the refractive index of layer 1,  $\theta_1$  the incidence angle and  $c$  the speed of light in vacuum. Starting with the  $s$ -polarization case, where the electric field is parallel to the  $y$ -axis, the electric field in the  $l$ th layer can be written as  $E_l(z)e^{i(k_x x - \omega t)}$  with (Yeh, 1988; Zhang et al., 2003)

$$E_1(z) = A_1 e^{ik_{1z}z} + B_1 e^{-ik_{1z}z}$$

and 
$$E_l(z) = A_l e^{ik_{lz}(z-z_{l-1})} + B_l e^{-ik_{lz}(z-z_{l-1})}, \quad l = 2, 3, \dots, N \quad (2.8)$$

where  $A_l$  and  $B_l$  are the amplitudes of the forward and backward waves at the interface, respectively,  $z_l = z_{l-1} + d_l$  ( $l = 2, 3, \dots, N-1$ ) with  $d_l$  the layer thickness. The magnetic field can be obtained from the electric field using Maxwell's equations. Here the expression of the wave component  $k_{lz}$  is calculated from  $k_x^2 + k_{lz}^2 = \epsilon_l \mu_l \omega^2 / c^2$  with its imaginary part not less than zero. Applying boundary conditions at the interface, the field amplitudes of adjacent layers relate as

$$\begin{pmatrix} A_l \\ B_l \end{pmatrix} = \mathbf{P}_l \mathbf{D}_l^{-1} \mathbf{D}_{l+1} \begin{pmatrix} A_{l+1} \\ B_{l+1} \end{pmatrix}, \quad l = 1, 2, \dots, N-1 \quad (2.9)$$

In Equation (2.9),  $\mathbf{P}_l$  is the propagation matrix given by

$$\mathbf{P}_l = \mathbf{I} = \begin{pmatrix} 1 & 0 \\ 0 & 1 \end{pmatrix}, \quad l = 1$$

and

$$\mathbf{P}_l = \begin{pmatrix} e^{-ik_{lz}d_l} & 0 \\ 0 & e^{ik_{lz}d_l} \end{pmatrix}, \quad l = 2, 3, \dots, N-1 \quad (2.10)$$

$\mathbf{D}_l$  is called the dynamical matrix and  $\mathbf{D}_l^{-1}$  is its inverse. For  $s$ -polarization,  $\mathbf{D}_l$  is given in terms of  $k_{lz}$  and  $\mu_l$  as follows

$$\mathbf{D}_l = \begin{pmatrix} 1 & 1 \\ \frac{k_{lz}}{\mu_l} & -\frac{k_{lz}}{\mu_l} \end{pmatrix}, \quad l = 1, 2, \dots, N \quad (2.11)$$

By successively applying Equation (2.9) to all the layers, one obtains

$$\begin{pmatrix} A_1 \\ B_1 \end{pmatrix} = \mathbf{M} \begin{pmatrix} A_N \\ B_N \end{pmatrix} \quad (2.12)$$

where

$$\mathbf{M} = \begin{pmatrix} M_{11} & M_{12} \\ M_{21} & M_{22} \end{pmatrix} = \prod_{l=1}^{N-1} \mathbf{P}_l \mathbf{D}_l^{-1} \mathbf{D}_{l+1} \quad (2.13)$$

The electric field transmission and reflection coefficients are obtained by setting  $B_N = 0$ , because the last layer is semi-infinite and thus no backward wave. Simple algebraic manipulation gives the expressions of the coefficients as

$$t = A_N / A_1 = 1 / M_{11} \quad (2.14)$$

and 
$$r = B_1 / A_1 = M_{21} / M_{11} \quad (2.15)$$

The transmittance  $T$  of the multilayer structure is defined as the ratio of the  $z$ -component of the Poynting vector  $\mathbf{S}$  for the transmitted wave to that for the incident wave. Combining Equations (2.14) and (2.3), and using Equation (2.1) to calculate the magnetic field from the electric field Equation (2.8), a general expression of the transmittance is given as

$$T = \frac{\text{Re}(k_{Nz}^* / \mu_N^*)}{\text{Re}(k_{1z}^* / \mu_1^*)} t t^* = \frac{\text{Re}(k_{Nz}^* / \mu_N^*)}{\text{Re}(k_{1z}^* / \mu_1^*)} \left| \frac{1}{M_{11}} \right|^2 \quad (2.16)$$

Similarly, the reflectance  $R$  is defined as the ratio of the  $z$ -component of the Poynting vector  $\mathbf{S}$  for the reflected wave to that for the incident wave, which is written as

$$R = r r^* = \left| \frac{M_{21}}{M_{11}} \right|^2 \quad (2.17)$$

For  $p$ -polarization, the magnetic field is parallel to the  $y$ -axis. Equation (2.8) can be written in terms of the magnetic field  $H$ . The same procedure can be used to derive the transmission and reflection coefficients for the magnetic field. Equations (2.9), (2.10), (2.12), and (2.13) are the same, but the dynamic matrix  $\mathbf{D}_l$  given in Equation (2.12) must be replaced by



$$\mathbf{D}_l = \begin{pmatrix} 1 & 1 \\ \frac{k_{lz}}{\varepsilon_l} & -\frac{k_{lz}}{\varepsilon_l} \end{pmatrix}, \quad l = 1, 2, \dots, N \quad (2.18)$$

The transmittance  $T$  for  $p$ -polarization is

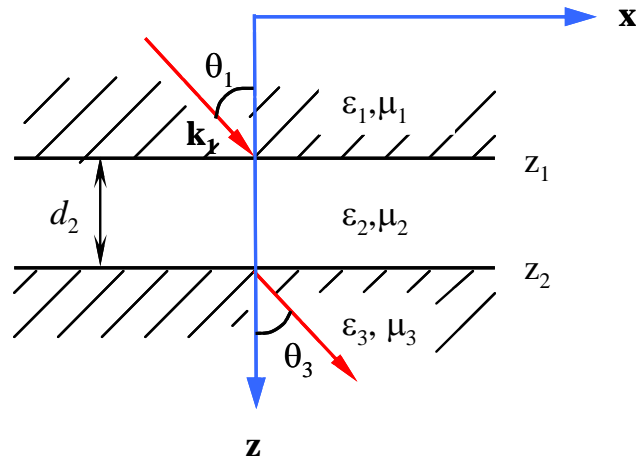
$$T = \frac{\operatorname{Re}(k_{Nz}/\varepsilon_N)}{\operatorname{Re}(k_{1z}/\varepsilon_1)} t t^* = \frac{\operatorname{Re}(k_{Nz}/\varepsilon_N)}{\operatorname{Re}(k_{1z}/\varepsilon_1)} \left| \frac{1}{M_{11}} \right|^2 \quad (2.19)$$

whereas the expression for the reflectance  $R$  is the same as given in Equation (2.17). It should be pointed out that the reflectance is ill-defined when the first medium is lossy because of the coupling between the reflected and incident waves (Zhang, 1997). However, Equations (2.8) to (2.19) are applicable if the last medium is lossy.

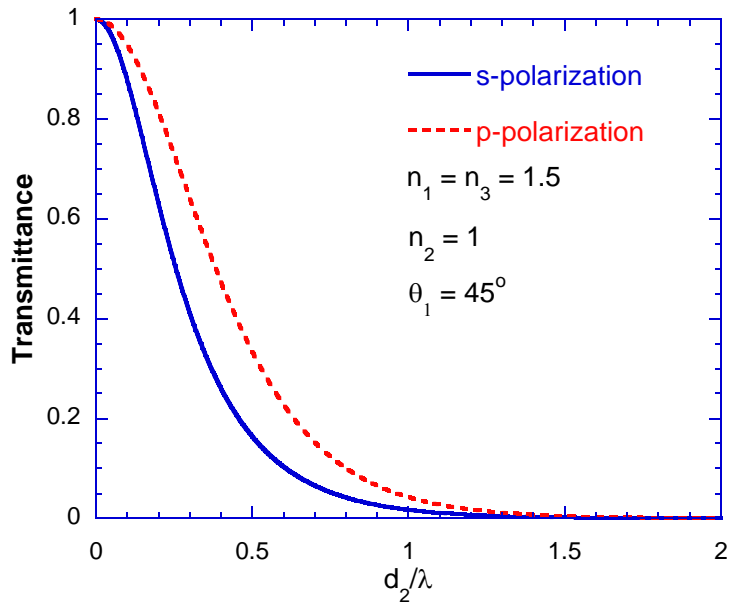
### 2.3 The Mechanism of Photon Tunneling

The mechanism of photon tunneling is related to total internal reflection. Total internal reflection occurs when a beam is incident from an optically denser material to another material at incidence angles greater than the critical angle determined by the ratio of the refractive indices of the two materials. Under this condition, no energy is transfer into the second medium, but there exist electromagnetic fields (evanescent waves) that decay exponentially away from the interface. When a third medium with sufficiently large refractive index is placed close to the first medium such that the second medium becomes a thin layer, photons can tunnel through the second medium into the third. This phenomenon is called photon tunneling, or radiation tunneling. The tunneled energy, however, is significant only when the thickness of the second medium is comparable or smaller than the wavelength of the incident beam. To be illustrative, consider the case shown in Figure 2.5(a) where a beam is incident from a semi-infinite medium (medium

1) with incidence angle  $\theta_1$ . The thickness of the second medium is  $d_2$  and the third medium is another semi-infinite medium. The transmittance of the three-layer structure can be calculated using the matrix formulation. Assume that both medium 1 and



(a)



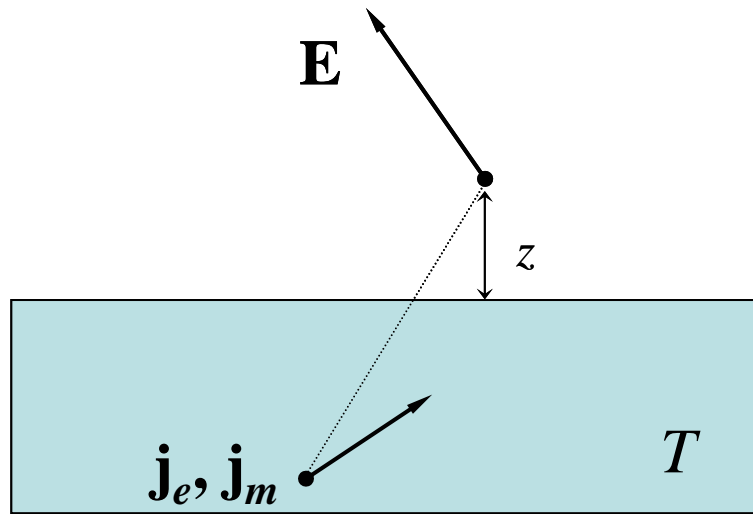
(b)

Figure 2.5 Photon tunneling in a three-layer structure: (a) Schematic of the structure and (b) Transmittance by photon tunneling.

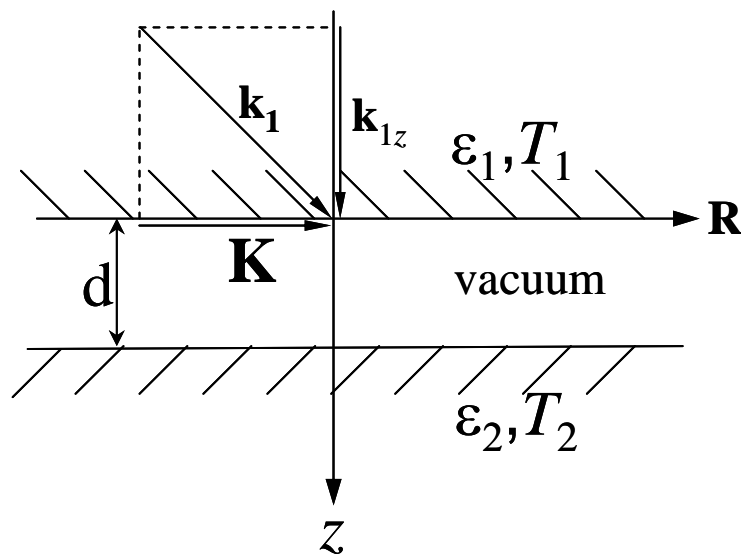
medium 3 are nonmagnetic and with the same refractive index  $n_1 = n_3 = 1.5$  and medium 2 is a vacuum gap,  $\theta_1$  should be greater than the critical angle  $\theta_c = \sin^{-1}(1/n_1) \approx 42^\circ$  for photon tunneling to occur. Setting  $\theta_1 = 45^\circ$ , the transmittance of the three-layer structure is shown in Figure 2.5(b) as a function of  $d_2/\lambda$ , where  $\lambda$  is the wavelength of the incident wave, and for both  $s$ - and  $p$ -polarizations. For a given wavelength  $\lambda$ , the strong dependence of the transmittance on the second layer thickness  $d_2$  is clearly seen. The rapid decrease of  $T$  with increasing  $d_2$  is because evanescent waves from the first interface decay exponentially with  $d_2$  inside the second medium. The exponential decay makes  $T$  insignificant for  $d_2 > \lambda$ . But under conditions that  $d_2 \ll \lambda$ , energy transfer by photon tunneling is tremendously significant and is the key in photon scanning tunneling microscopy (Reddick et al., 1990; Shen et al., 2000) and in micro/nanoscale radiation heat transfer (Pendry, 1999; Whale and Cravalho, 2002; Narayanaswamy and Chen, 2003).

## 2.4 Fundamentals of the Fluctuational Electrodynamics

The importance of photon tunneling for micro/nanoscale radiation heat transfer has been discussed above. Here the question is how to calculate the net heat flux between two thermally emitting bodies at different temperatures and separated by small spacing. From a classic point of view, thermal emission from a body of temperature  $T$  covers all the frequencies from zero to infinity and propagates in any directions viewed by the emitting surface. The famous Stefan-Boltzmann law has been the standard tool to calculate the net heat transfer between two radiating bodies with the separation distance



(a)



(b)

Figure 2.6 Illustration of (a) the mechanism of thermal radiation from a body of temperature  $T$  and (b) Coordinate system used in of the calculation of near-field heat transfer between two semi-infinite media separated by a vacuum gap of thickness  $d$ .

much greater than the characteristic emission wavelength given by Wien's displacement law (Siegel and Howell, 2002). The regime in which radiation heat transfer can be calculated by the Stefan-Boltzmann law is categorized as the far-field regime. The Stefan-Boltzmann law breaks down when the separation distance between two radiating bodies become comparable or smaller than the characteristic wavelength, which is in the near-field regime, due to wave interfere effect and photon tunneling (Born and Wolf, 1999).

The fluctuational electrodynamics is used in this thesis to calculate near-field radiation heat transfer. The fundamentals of this method are explained in the following paragraphs.

Thermal radiation from a body of temperature  $T$  is schematically illustrated in Figure 2.6(a). It is electromagnetic radiation from fluctuating electric and magnetic current densities  $\mathbf{j}_e(\mathbf{r}, t)$  and  $\mathbf{j}_m(\mathbf{r}, t)$ , which is caused by random thermal fluctuation in the body.  $\mathbf{j}_e(\mathbf{r}, t)$  and  $\mathbf{j}_m(\mathbf{r}, t)$  expressed in the frequency space can be done by Fourier transformation, denoted by  $\mathbf{j}_e(\mathbf{r}, \omega)$  and  $\mathbf{j}_m(\mathbf{r}, \omega)$  here. The electric field  $\mathbf{E}$  and magnetic field  $\mathbf{H}$  of the thermal radiation are related to the sources  $\mathbf{j}_e(\mathbf{r}, \omega)$  and  $\mathbf{j}_m(\mathbf{r}, \omega)$  by Maxwell's equations as (Rytov, 1987)

$$\nabla \times \mathbf{E} = i\omega\mu_0\mu\mathbf{H} - \mathbf{j}_m(\mathbf{r}, \omega) \quad (2.20)$$

and 
$$\nabla \times \mathbf{H} = -i\omega\varepsilon_0\varepsilon\mathbf{E} + \mathbf{j}_e(\mathbf{r}, \omega) \quad (2.21)$$

For nonmagnetic materials,  $\mu = 1$  and  $\mathbf{j}_m = 0$ . The rest of the derivation will only for nonmagnetic materials for simplicity and for the reason that magnetic materials are not considered in this thesis as thermal sources. Therefore, the subscript "e" will be neglected

in the current density. From Equations (2.20) and (2.21), the electric field  $\mathbf{E}(\mathbf{r}, \omega)$  and magnetic field  $\mathbf{H}(\mathbf{r}, \omega)$  can be expressed using the dyadic Green function as

$$\mathbf{E}(\mathbf{r}, \omega) = i\omega\mu_0 \int_V \overline{\overline{\mathbf{G}}}(\mathbf{r}, \mathbf{r}', \omega) \cdot \mathbf{j}(\mathbf{r}', \omega) d\mathbf{r}' \quad (2.22)$$

$$\mathbf{H}(\mathbf{r}, \omega) = \int_V \nabla_{\mathbf{r}} \times \overline{\overline{\mathbf{G}}}(\mathbf{r}, \mathbf{r}', \omega) \cdot \mathbf{j}(\mathbf{r}', \omega) d\mathbf{r}' \quad (2.23)$$

where  $\overline{\overline{\mathbf{G}}}(\mathbf{r}, \mathbf{r}', \omega)$  is the dyadic Green function of the electric field at point  $\mathbf{r}$  from a source at point  $\mathbf{r}'$  and  $V$  denotes the volume of the emitting body.

The energy density of the emitted electromagnetic field can be calculated from (Mandel and Wolf, 1995; Joulain et al., 2000)

$$u(\mathbf{r}, \omega) = \varepsilon_0 \langle \mathbf{E}(\mathbf{r}, \omega) \cdot \mathbf{E}^*(\mathbf{r}, \omega) \rangle + \mu_0 \langle \mathbf{H}(\mathbf{r}, \omega) \cdot \mathbf{H}^*(\mathbf{r}, \omega) \rangle \quad (2.24)$$

where  $\langle \rangle$  denotes the average of an ensemble of realizations of the random currents. Note that the definition of the energy density above is 4 times the conventional definition because the frequencies considered here are only for positive values such that the signals are analytic (Mandel and Wolf, 1995; Joulain et al., 2000). Substituting Equations (2.22) and (2.23) into Equation (2.24), the ensemble average will be taken on the spatial correlation function of the fluctuating currents. This quantity is given by the fluctuation-dissipation theorem (Rytov, 1987)

$$\langle j_m(\mathbf{r}', \omega) j_n^*(\mathbf{r}'', \omega) \rangle = \frac{\omega \varepsilon_0 \varepsilon''(\omega) \Theta(\omega, T)}{\pi} \delta_{mn} \delta(\mathbf{r}' - \mathbf{r}'') \quad (2.25)$$

where  $\varepsilon''(\omega)$  is the imaginary part of the dielectric function of the emitting body,  $\delta_{mn}$  is the Kronecker delta function,  $\delta(\mathbf{r}' - \mathbf{r}'')$  is the Dirac delta function, and  $\Theta(\omega, T)$  is given by  $\hbar\omega / [\exp(\hbar\omega / k_B T) - 1]$ .

For the emitted energy flux, it is expressed as (Loomis and Maris, 1994; Mulet, et al., 2002)

$$\langle \mathbf{S}(\mathbf{r}, \omega) \rangle = 2 \langle \text{Re}[\mathbf{E}(\mathbf{r}, \omega) \times \mathbf{H}^*(\mathbf{r}, \omega)] \rangle \quad (2.26)$$

Again, the ensemble average will be taken on the spatial correlation function of the fluctuating currents when Equations (2.22) and (2.23) are substituted into Equation (2.26).

In the case that thermal emission is from a semi-infinite medium 1 to a semi-infinite medium 2 with a vacuum gap of thickness  $d$  in between and the two interfaces are smooth and are parallel to each other, as shown schematically in Figure 2.6(b), the dyadic Green function can be taken as (Sipe, 1987; Shchegrov et al., 2000; Mulet et al., 2002)

$$\mathbf{G}(\mathbf{r}, \mathbf{r}', \omega) = \frac{i}{8\pi^2} \int \frac{1}{k_{1z}} (\hat{\mathbf{s}} t_{12}^s \hat{\mathbf{s}} + \hat{\mathbf{p}}_2 t_{12}^p \hat{\mathbf{p}}_1) \times \exp(ik_{2z}z - ik_{1z}z') \exp[i\mathbf{K}(\mathbf{R} - \mathbf{R}')] d\mathbf{K} \quad (2.27)$$

where  $\mathbf{r} = \mathbf{R} + z\hat{\mathbf{z}}$  with  $\mathbf{R}$  parallel to the surfaces, the wavevector  $\mathbf{k}_j = K\hat{\mathbf{K}} + k_{jz}\hat{\mathbf{z}}$ , the unit vectors  $\hat{\mathbf{s}} = \hat{\mathbf{K}} \times \hat{\mathbf{z}}$  and  $\hat{\mathbf{p}}_j = (K\hat{\mathbf{z}} - k_{jz}\hat{\mathbf{K}})/k_j$ ,  $k_j = \omega\sqrt{\epsilon_j}/c$ , and  $k_{jz} = \sqrt{k_j^2 - K^2}$ , and  $t_{12}^s$  and  $t_{12}^p$  are the transmission coefficients from medium 1 to medium 2 for the  $s$ - and  $p$ -polarizations, respectively. Note that if thermal emission is only from medium 1 to vacuum, then  $t_{12}^s$  and  $t_{12}^p$  are simply replaced with the Fresnel coefficients of transmission from medium 1 to vacuum for the  $s$ - and  $p$ -polarizations. Inserting Equation (2.27) into Equations (2.22) and (2.23) and together with Equations (2.24) and (2.25), the energy density emitted from a semi-infinite medium into vacuum can be expressed as (Joulain et al., 2000)

$$\begin{aligned}
u(z, \omega) &= u_{prop}(z, \omega) + u_{evan}(z, \omega) \\
&= \frac{\Theta(\omega, T)\omega}{\pi^2 c^2} \int_0^{\omega/c} \frac{KdK}{k_{vz}} \frac{(2 - |r_{v1}^s|^2 - |r_{v1}^p|^2)}{2} \\
&\quad + \frac{\Theta(\omega, T)}{\pi^2 \omega} \int_{\omega/c}^{\infty} \frac{e^{-2\text{Im}(k_{vz})z} K^3 dK}{|k_{vz}|} \frac{(\text{Im}(r_{v1}^s) + \text{Im}(r_{v1}^p))}{2} \quad (2.28)
\end{aligned}$$

where  $k_{vz}$  is  $z$ -component of the wavevector in vacuum given by  $k_{vz} = \sqrt{(\omega^2 / c^2) - K^2}$ ,  $r_{v1}^s$  and  $r_{v1}^p$  are the reflection coefficients from vacuum to medium 1,  $u_{prop}(z, \omega)$  and  $u_{evan}(z, \omega)$  are the contributions to the energy density from propagating waves and evanescent waves, respectively.  $u(z, \omega)$  in Equation (2.28) does not depend on  $x$  and  $y$  because the emitting surface of medium1 is assumed infinite in these two directions. The spectral energy flux from medium 1 to medium 2 is calculated from Equation (2.26) as

$$q''_{\omega,1-2} = \langle S_z(d_+, \omega) \rangle |_{T_1} \quad (2.29)$$

Using the dyadic Green function, it has been shown that (Mulet et al., 2002)

$$\begin{aligned}
q''_{\omega,1-2} &= \frac{4}{\pi^2} \int_0^{\infty} \Theta(\omega, T_1) |e^{ik_{vz}d}|^2 KdK \\
&\quad \times \left[ \frac{|k_{vz}|^2}{|1 - r_{v1}^s r_{v2}^s e^{2ik_{vz}d}|^2} \frac{\text{Re}(k_{1z}) \text{Re}(k_{2z})}{|(k_{vz} + k_{1z})(k_{vz} + k_{2z})|^2} \right. \\
&\quad \left. + \frac{|k_{vz}|^2}{|1 - r_{v1}^p r_{v2}^p e^{2ik_{vz}d}|^2} \frac{\text{Re}(\varepsilon_1 k_{1z}^*) \text{Re}(\varepsilon_2 k_{2z}^*)}{|(\varepsilon_1 k_{vz} + k_{1z})(\varepsilon_2 k_{vz} + k_{2z})|^2} \right] \quad (2.30)
\end{aligned}$$



Note that  $q''_{\omega,1-2}$  in Equation (2.30) includes the contributions from both propagating waves and evanescent waves (photon tunneling). A similar expression can be obtained to evaluate  $q''_{\omega,2-1}$ . The net total energy flux is the integration of  $q''_{\omega,1-2} - q''_{\omega,2-1}$  over all frequencies from 0 to infinity,

$$q''_{net} = \int_0^{\infty} (q''_{\omega,1-2} - q''_{\omega,2-1}) d\omega \quad (2.31)$$

Equation (2.31) will be used to compute the radiation heat transfer in both far-field and near-field. It should be noted that angular frequency  $\omega$  is chosen for convenience in the dielectric function and the fluctuational electrodynamics formulation. Table 2.1 provides the conversion of units so that the results can be understood in terms of frequency, wave number, or wavelength.

Table 2.1 Conversion of values between angular frequency ( $\omega$ ) and frequency ( $\nu$ ), wave number ( $\eta$ ), and wavelength ( $\lambda$ )

|  |                       |                       |                       |                       |
|--|-----------------------|-----------------------|-----------------------|-----------------------|
| $\omega$ (rad/s)                                       | $10^{12}$             | $10^{13}$             | $10^{14}$             | $10^{15}$             |
| $\nu = \omega/2\pi$ (Hz)                               | $1.592 \cdot 10^{11}$ | $1.592 \cdot 10^{12}$ | $1.592 \cdot 10^{13}$ | $1.592 \cdot 10^{14}$ |
| $\eta = \omega \cdot 0.01/2\pi c$ ( $\text{cm}^{-1}$ ) | 5.305                 | 53.05                 | 503.5                 | 5035                  |
| $\lambda = 2\pi c \cdot 10^6/\omega$ ( $\mu\text{m}$ ) | 1885                  | 188.5                 | 18.85                 | 1.885                 |

### CHAPTER 3 PHOTON TUNNELING IN MULTILAYER STRUCTURES INCLUDING NEGATIVE INDEX MATERIALS

It has been shown in Chapter 2 that photon tunneling can be important for radiation energy transfer between two closely spaced media. But the energy transfer by photon tunneling is significant only for the separation distance between the two media being comparable or smaller than the characteristic wavelength due to the exponential decay of evanescent waves in the spacing between the two media. It has been shown (Pendry, 2000) that an NIM slab with  $\epsilon = \mu = -1$  for a lens not only performs the function of correcting the phase of the propagating components, but can amplify the evanescent components of the signal from an object. The combined effects could make the NIM a perfect lens that eliminates the limitations on image resolution imposed by diffraction for conventional lenses. Motivated by the idea of a perfect lens, it is easy to think that an NIM can be used to improve photon tunneling efficiency.

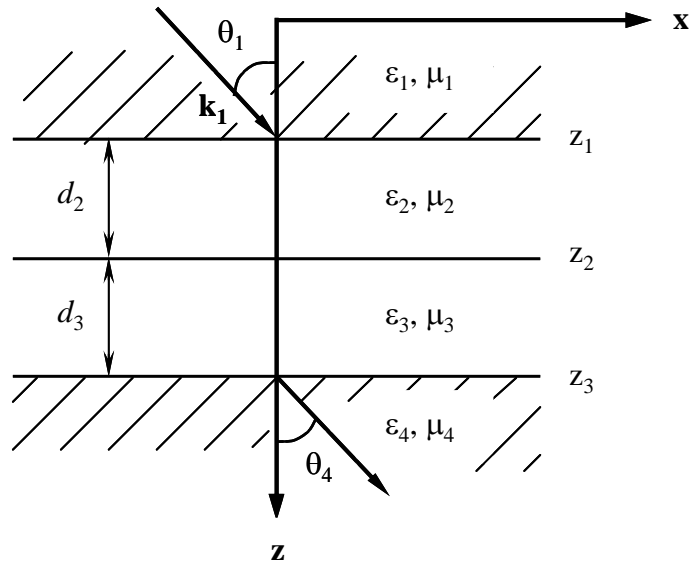
In this chapter, the problem of energy transmission by photon tunneling is studied. It is assumed that photon tunneling is between two semi-infinite dielectrics with flat surfaces and separated by a vacuum gap. In order to see whether the photon tunneling efficiency is enhanced by an NIM, an NIM layer is assumed to insert into the vacuum gap that separate the two dielectrics. Different values of  $\epsilon$  and  $\mu$  of the NIM will be studied including the perfect lens case ( $\epsilon = \mu = -1$ ), a non-ideal lossless NIM and frequency-dependence and loss of  $\epsilon$  and  $\mu$ . Different arrangements and number of NIM layers will also be investigated. For the purpose of convenience, the modified matrix formulation,

which has been described in Chapter 2, will be employed to calculate the transmittance of the multilayer structure.

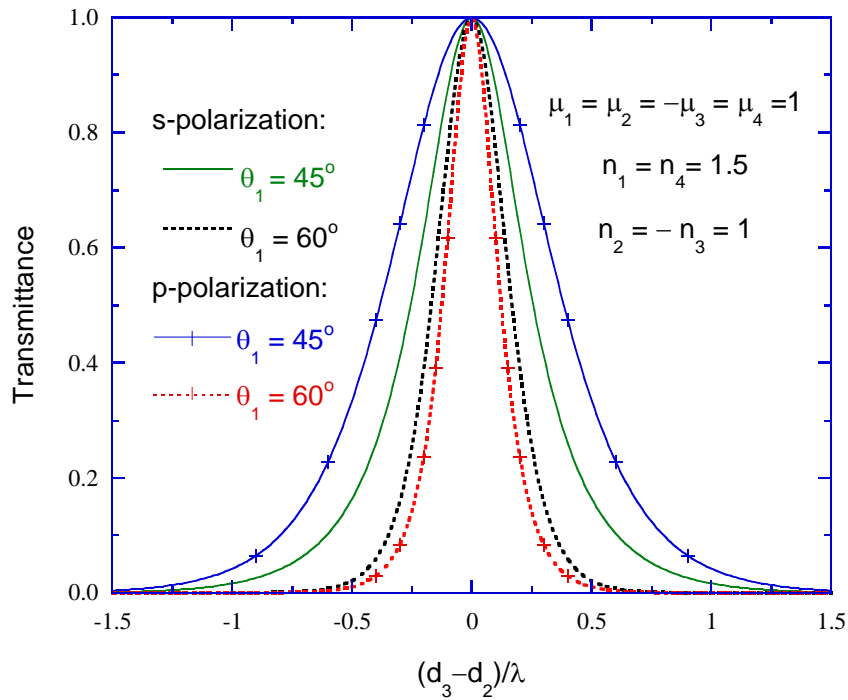
### 3.1 The Case of Perfect Index Matching

The perfect lens proposed by Pendry (2000) is an NIM slab of  $\varepsilon = \mu = -1$ , which results in the refractive index  $n = -1$ . In order to see the effect of an NIM slab on photon tunneling, consider the following four-layer ( $N = 4$ ) structure as shown in Figure 3.1(a). The first and last media are semi-infinite dielectric with  $\varepsilon_1 = \varepsilon_4 = 2.25$  ( $n_1 = n_4 = 1.5$ ). There are two intermediate layers: layer 2 is a vacuum gap of thickness  $d_2$  and layer 3 is made of an NIM of thickness  $d_3$ . In the present study,  $\varepsilon_3 = \mu_3 = -1$ . For radiation from medium 1, the incidence angle should be greater than the critical angle  $\theta_c = \sin^{-1}(1/n_1) \approx 42^\circ$  in order for photon tunneling to occur. Note that without the NIM layer, the structure restores to the case of Figure 2.5(a) and the transmittance for the incidence angle  $\theta_1 = 45^\circ$  has been shown in Figure 2.5(b).

When the NIM layer is employed, the transmittance of this layered structure is recalculated and plotted in Figure 3.1(b).  $\lambda$  in the figure is assumed the wavelength where  $\varepsilon_1 = \mu_1 = -1$ . Very different result is found. The transmittance reaches a maximum of unity at  $d_3 = d_2$  and decreases rapidly as the difference between  $d_3$  and  $d_2$  increases. The maximum transmittance, however, is independent of the incidence angle  $\theta_1$ . This means as long as the condition  $d_3 = d_2$  is satisfied, the maximum transmittance of unity is obtained regardless of the values of  $d_2$ ,  $d_3$ , and  $\theta_1$ . Therefore, the NIM layer can significantly enhance the transmittance (Zhang and Fu, 2002).



(a)



(b)

Figure 3.1 Photon tunneling enhanced by an NIM layer: (a) Schematic of a four-layer structure and (b) The transmittance as a function of  $(d_3 - d_2)/\lambda$  of the structure with optical parameters indicated.

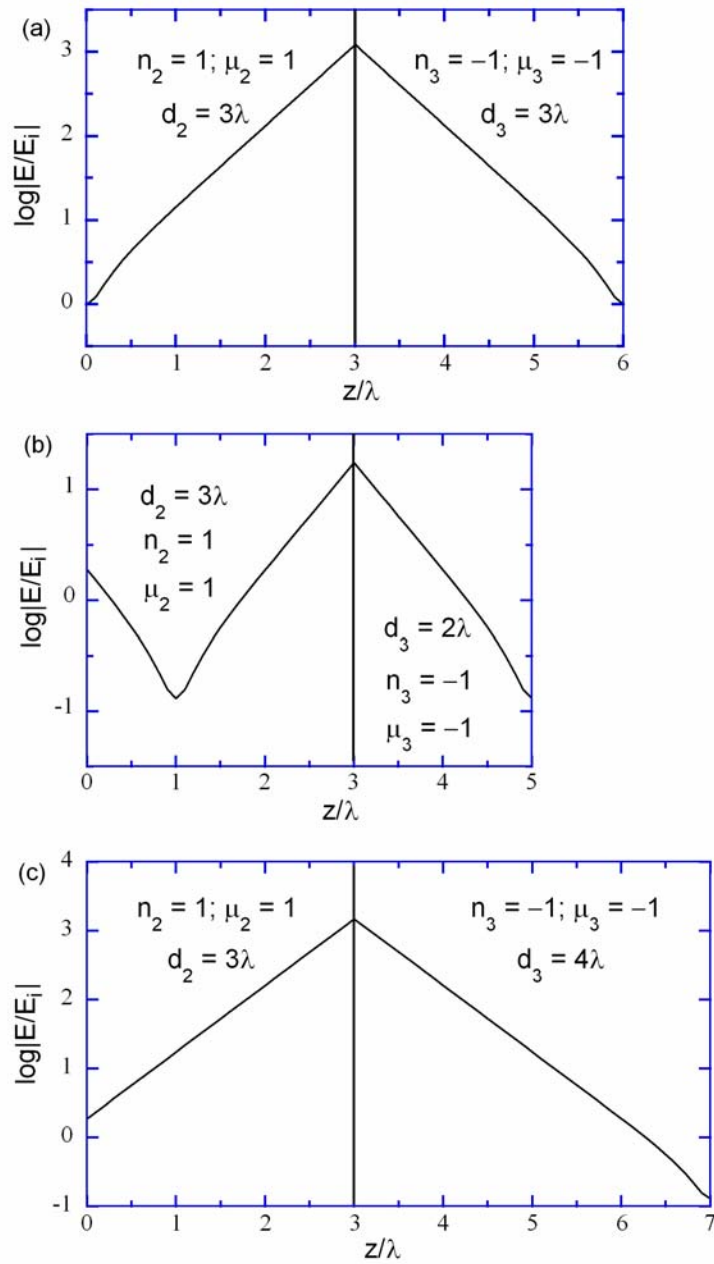


Figure 3.2 The evanescent fields in media 2 and 3 (for TE wave), with  $n_1 = n_4 = 1.5$ ,  $\mu_1 = \mu_4 = 1$ , and an incidence angle  $\theta_1 = 45^\circ$ : (a)  $d_3 = d_2$ ; (b)  $d_3 < d_2$ ; (c)  $d_3 > d_2$ .

To understand whether the evanescent wave decays or grows in the NIM, the field strength  $|E(z)|$  has been calculated from Equation (2.8) using the coefficients obtained from Equation (2.9). The results, normalized to the incident electric field strength  $|E_i|$ , are shown in Figure 3.2 for  $d_2 = 3\lambda$  and  $d_3 = 3\lambda, 2\lambda$ , and  $4\lambda$ . In Figure 3.2 (a), the field strength increases in medium 2 and reaches a peak at the interface between media 2 and 3. However, it decreases in the NIM (medium 3). The symmetry with respect to the interface makes the field strength at  $z = 6\lambda$  the same as that at  $z = 0$ . The shape is the same when the materials of media 2 and 3 are interchanged. Hence, it is the combination of the NIM with a matching PIM that causes the amplitude of evanescent waves to first increase and then decrease by the same amount. When  $d_3 \neq d_2$ , the field strength at the interface between media 3 and 4 is much lower than that at the interface between media 1 and 2. Hence, the transmittance decreases as the difference between  $d_3$  and  $d_2$  increases (see Figure 3.1). The field strength for a  $p$ -polarized wave exhibits the same trend as that for an  $s$ -polarized wave with somewhat different values.

### 3.2 A Non-Ideal Lossless NIM

In order to better understand the capability of an NIM to enhance photon tunneling, a non-ideal lossless NIM has also been studied. For easier discussion, the transmission coefficient  $t$  calculated from Equation (2.15) for a four-layer structure can be expanded and expressed in a compact form as (Fu and Zhang, 2003)

$$t = \frac{8}{\xi_1 e^{-i\Psi_1} + \xi_2 e^{i\Psi_1} + \xi_3 e^{-i\Psi_2} + \xi_4 e^{i\Psi_2}} \quad (3.1)$$

In the above equation, the phase angles  $\psi_1$  and  $\psi_2$  are the same for both s- and p-polarizations, which can be expressed as

$$\psi_1 = k_{2z}d_2 + k_{3z}d_3 \quad (3.2a)$$

and 
$$\psi_2 = k_{2z}d_2 - k_{3z}d_3 \quad (3.2b)$$

For s-polarization, the coefficients in Equation (2.11) are

$$\xi_1 = \left(1 + \frac{k_{2z}\mu_1}{k_{1z}\mu_2}\right) \left(1 + \frac{k_{3z}\mu_2}{k_{2z}\mu_3}\right) \left(1 + \frac{k_{4z}\mu_3}{k_{3z}\mu_4}\right) \quad (3.3a)$$

$$\xi_2 = \left(1 - \frac{k_{2z}\mu_1}{k_{1z}\mu_2}\right) \left(1 + \frac{k_{3z}\mu_2}{k_{2z}\mu_3}\right) \left(1 - \frac{k_{4z}\mu_3}{k_{3z}\mu_4}\right) \quad (3.3b)$$

$$\xi_3 = \left(1 + \frac{k_{2z}\mu_1}{k_{1z}\mu_2}\right) \left(1 - \frac{k_{3z}\mu_2}{k_{2z}\mu_3}\right) \left(1 - \frac{k_{4z}\mu_3}{k_{3z}\mu_4}\right) \quad (3.3c)$$

and 
$$\xi_4 = \left(1 - \frac{k_{2z}\mu_1}{k_{1z}\mu_2}\right) \left(1 - \frac{k_{3z}\mu_2}{k_{2z}\mu_3}\right) \left(1 + \frac{k_{4z}\mu_3}{k_{3z}\mu_4}\right) \quad (3.3d)$$

For p-polarization, the coefficients can be obtained by replacing the  $\mu$ 's in Equation (3.3) with the corresponding  $\varepsilon$ 's. Note that Equations (3.1) – (3.3) are derived directly from the matrix formulation without any further assumptions so that they are applicable to both propagating waves and evanescent waves and the transmittance  $T$  is still Equation (2.16) for s-polarization and Equation (2.19) for p-polarization.

The four-layer structure studied in this section is the same as that in section 3.1 except that the refractive index of the NIM layer (the third layer) is assumed to have a small deviation from  $-1$ . For convenience,  $\mu_3$  is assumed equal to  $-1$  and the effect of changing  $n_3$  (equivalent to changing  $\varepsilon_3$  because  $\mu_3 = -1$ ,  $\varepsilon_3 = -n_3^2$ ) about  $-1$  on the

transmittance is investigated. The effects of  $d_2/\lambda$  and  $d_3/d_2$  are also investigated to see if there exist optimized combinations that result in maximum tunneling transmittance.

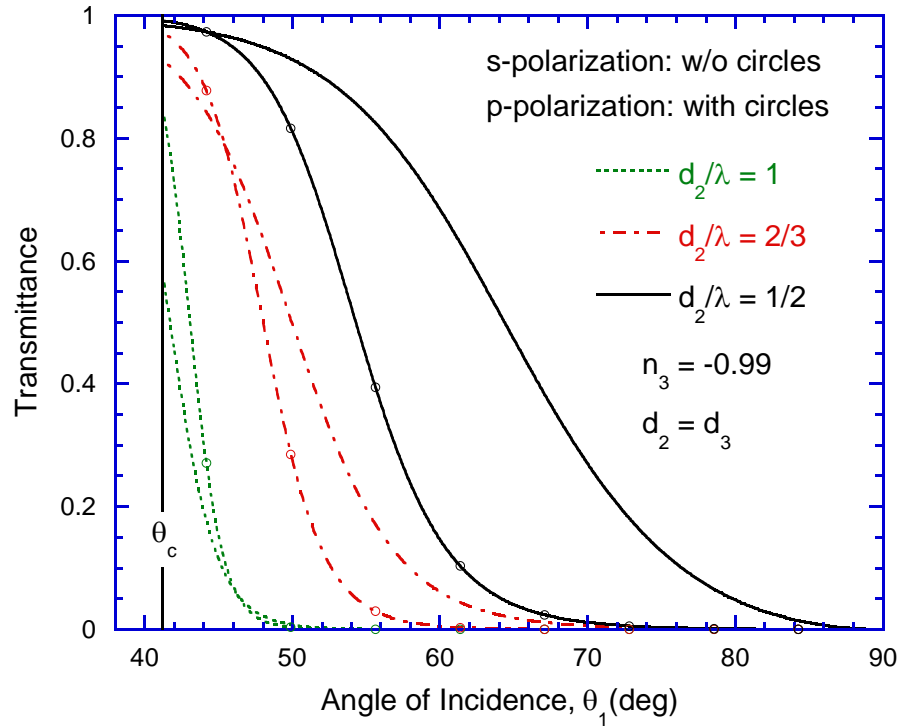


Figure 3.3 The polarized transmittance versus the incidence angle  $\theta_1$  for  $d_2/\lambda = 1, 2/3,$  and  $1/2$ , where  $n_3 = -0.99$  and  $d_3 = d_2$ .

When  $n_3 = -0.99$ , the transmittance by photon tunneling is shown in Figure 3.3 as a function of the angle of incidence for different  $d_2/\lambda$  values when  $d_3$  is equal to  $d_2$ . A slight deviation of  $n_3$  from  $-1$  will cause a significant reduction in the transmittance, especially at large incidence angles and for short wavelength (as compared to  $d_2$ ). The reduction of transmittance indicates that part of the energy is reflected back to medium 1. It is reasonable to expect that when  $n_3 \neq -n_2$ , the transmittance may not be maximum



when  $d_3 = d_2$ . To demonstrate this, the transmittance as a function of the ratio  $d_3/d_2$  is shown in Figure 3.4 for different  $n_3$  values. Here, the incidence angle is equal to  $45^\circ$  and the wavelength is equal to  $d_2$ . When  $d_3 = 0$ , the results approach the corresponding cases without the NIM layer, in which case, the transmittance decreases rapidly as  $d_2$  increases for any given wavelength. Obviously, the use of a NIM can increase the transmittance. From Figure 3.4, it can be seen that the peak transmittance occurs at  $d_3$  values much different from  $d_2$ . However, the peak transmittance is much smaller than unity when  $n_3 = -0.95$ .

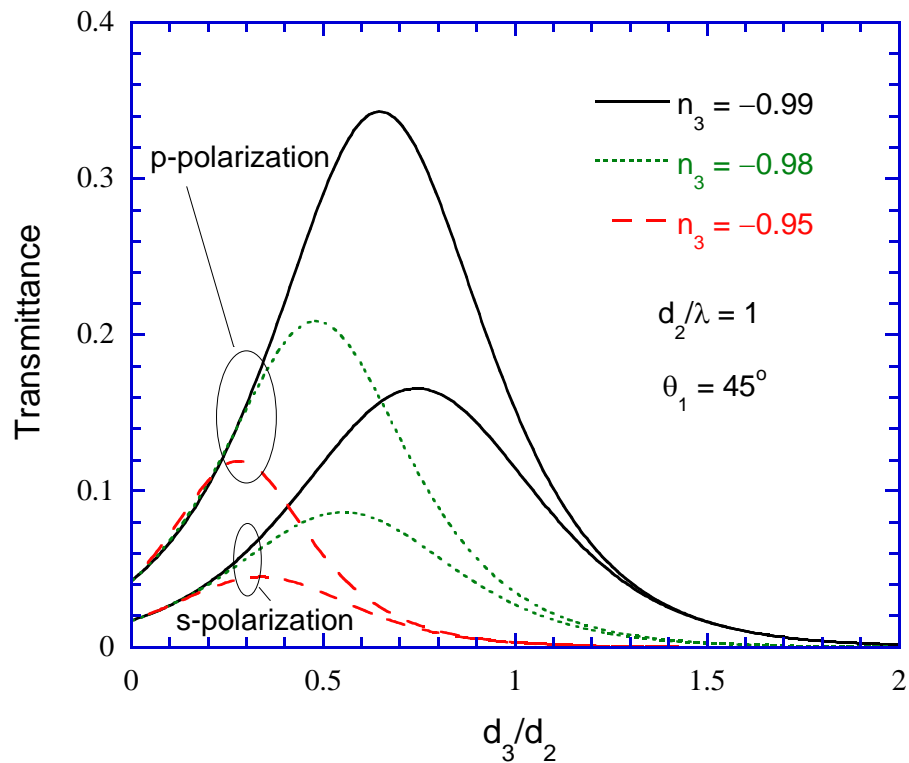


Figure 3.4 The polarized transmittance versus  $d_3/d_2$  for  $n_3 = -0.99, -0.98,$  and  $-0.95$ , where  $d_2/\lambda = 1$  and  $\theta_1 = 45^\circ$ .

An intriguing question is how to achieve the maximum tunneling transmittance for given  $n_3$  values but there exists no simple relation. To determine  $d_{3,\max}$  that yields the peak transmittance for given values of  $n_3$  and  $\theta_1$ , we set the partial derivative of  $T$  in Equations (2.16) and (2.19) with respect to  $d_3$  equal to zero and obtained the following expression for both polarizations:

$$d_{3,\max} = \frac{1}{4ik_{3z}} \ln \left( \frac{C_1 + C_3}{C_2 + C_4} \right) \quad (3.4)$$

where  $C_1 = \left( \text{Re}(\xi_1)e^{-ik_{2z}d_2} + \text{Re}(\xi_4)e^{ik_{2z}d_2} \right)^2 \quad (3.5a)$

$$C_2 = \left( \text{Re}(\xi_4)e^{-ik_{2z}d_2} + \text{Re}(\xi_1)e^{ik_{2z}d_2} \right)^2 \quad (3.5b)$$

$$C_3 = \left( \text{Im}(\xi_1)e^{-ik_{2z}d_2} + \text{Im}(\xi_4)e^{ik_{2z}d_2} \right)^2 \quad (3.5c)$$

and  $C_4 = \left( \text{Im}(\xi_4)e^{-ik_{2z}d_2} + \text{Im}(\xi_1)e^{ik_{2z}d_2} \right)^2 \quad (3.5d)$

Here, Re and Im take the real part and the imaginary part of a complex number, respectively. Notice that  $ik_{2z}$  and  $ik_{3z}$  are real since both  $k_{2z}$  and  $k_{3z}$  are purely imaginary, and  $\xi_1 = \xi_2^*$  and  $\xi_3 = \xi_4^*$ . Figure 3.5 shows  $d_{3,\max}$  versus  $n_3$  for both  $s$ - and  $p$ -polarizations at different incidence angles and for different  $d_2/\lambda$  ratios. In this figure,  $n_3$  changes from  $-1.05$  to  $-0.95$ . If  $n_3 = -1$ ,  $d_{3,\max} = d_2$  regardless of the other parameters. When  $n_3$  is close to  $-1$ ,  $d_{3,\max}$  may be greater or less than  $d_2$  to obtain the peak transmittance. As the deviation of  $n_3$  from  $-1$  becomes large, however,  $d_{3,\max}$  is always less than  $d_2$ . The corresponding peak transmittance is shown in Figure 3.6. The

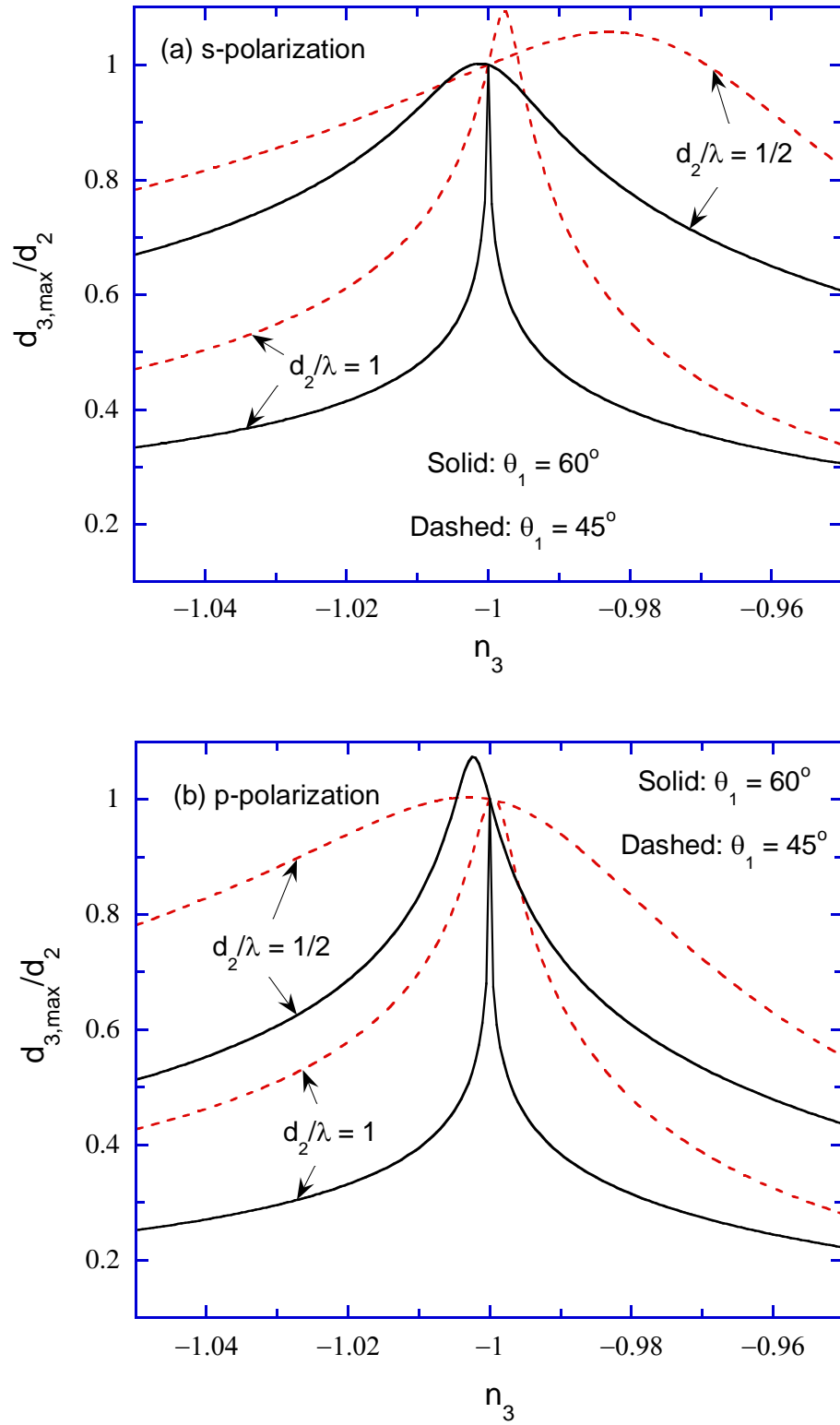


Figure 3.5  $d_{3,\max}/d_2$  versus  $n_3$  for different  $d_2/\lambda$  and  $\theta_1$ : (a) *s*-polarization; (b) *p*-polarization.

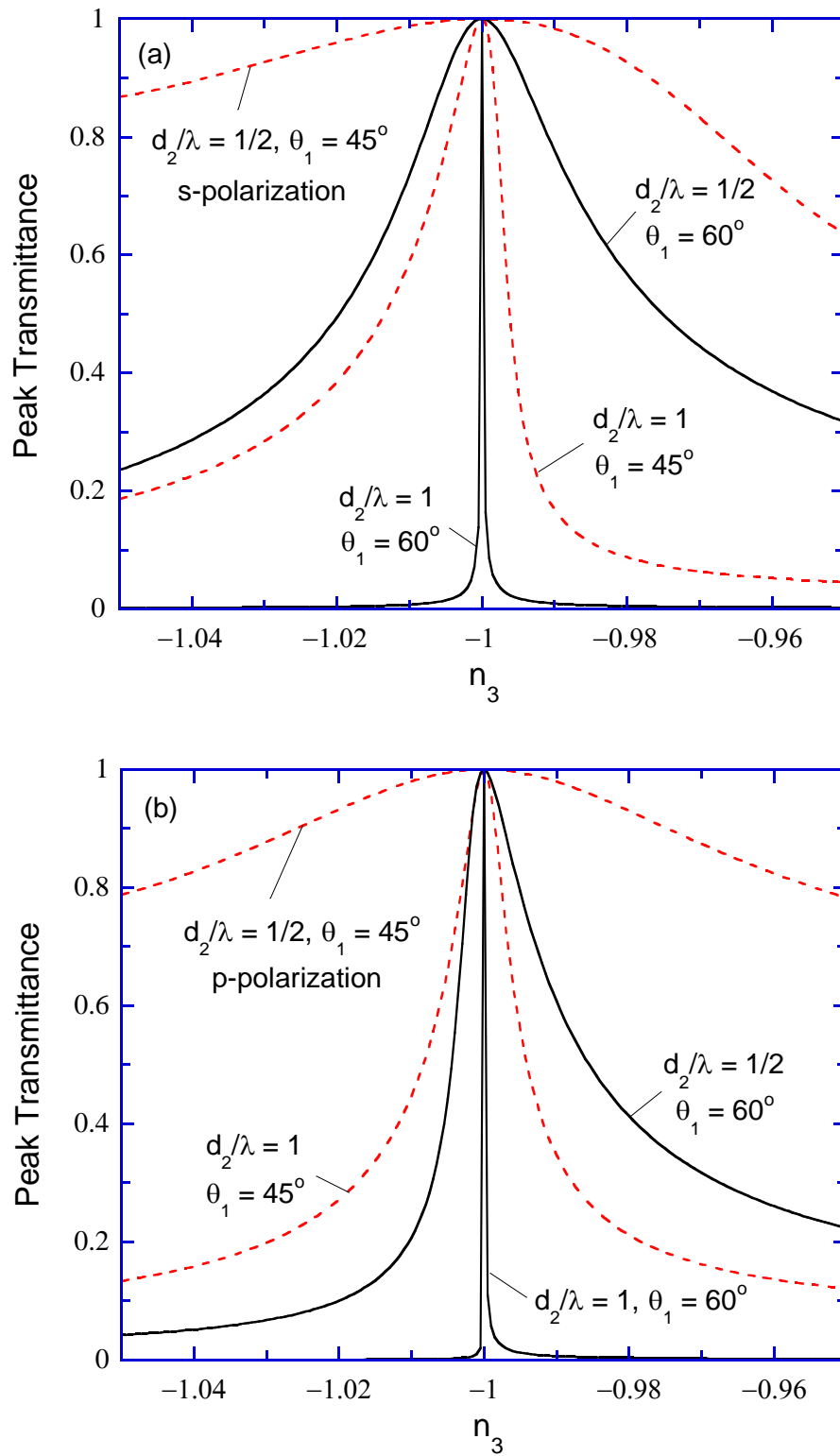


Figure 3.6 The peak transmittance as a function of  $n_3$  for different  $d_2/\lambda$  and  $\theta_1$ : (a) *s*-polarization; (b) *p*-polarization.

transmittance is always less than unity as long as  $n_2 \neq -n_3$  and decreases rapidly as  $n_3$  deviates further away from  $-1$ , especially at large incidence angles.

### 3.3 The Effect of the NIM Layer on the Hemispherical Transmittance

The transmittance given in Equations (2.16) and (2.19) is categorized as the directional spectral transmittance. The hemispherical spectral transmittance, or simply hemispherical transmittance, is defined as (Siegel and Howell, 2002)

$$T_h = \frac{\int_0^{\pi/2} \int_0^{2\pi} I_{\lambda,i}(\theta_1, \phi_1) \bar{T}(\theta_1) \sin \theta_1 \cos \theta_1 d\theta_1 d\phi_1}{\int_0^{\pi/2} \int_0^{2\pi} I_{\lambda,i}(\theta_1, \phi_1) \sin \theta_1 \cos \theta_1 d\theta_1 d\phi_1} \quad (3.6)$$

where  $I_{\lambda,i}$  is the spectral intensity of the incoming radiation, which is assumed to be randomly polarized,  $\bar{T}(\theta_1)$  is the average of the transmittance obtained for  $s$ - and  $p$ -polarizations from Equations (2.16) and (2.19), respectively. Because all layers are isotropic,  $\bar{T}(\theta_1)$  is independent of the azimuthal angle  $\phi_1$ . If the radiation is incident uniformly from all over the hemisphere, such as in the case of a blackbody, the intensity is independent of  $\theta_1$  and  $\phi_1$ . Hence, the hemispherical transmittance is

$$T_h = 2 \int_0^{\pi/2} \bar{T}(\theta_1) \sin \theta_1 \cos \theta_1 d\theta_1 \quad (3.7)$$

The contribution of propagating waves can be obtained by setting the upper integration limit to the critical angle  $\theta_c$ , and the contribution of photon tunneling or evanescent waves can be obtained by setting the lower integration limit to  $\theta_c$ .

In the ideal case  $n_3 = -1$ , the calculated hemispherical transmittance is shown in Figure 3.7 as a function of  $d_3/d_2$ , for  $d_2 = \lambda$ . Here,  $\lambda$  is the wavelength corresponding

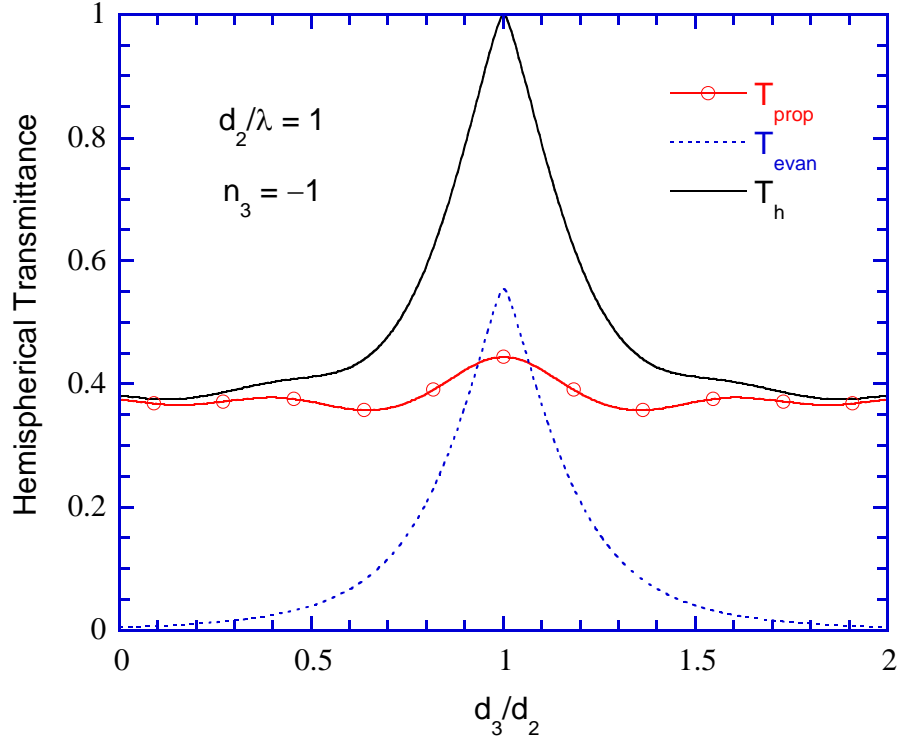


Figure 3.7 The hemispherical transmittance of the layered structure versus  $(d_3 - d_2)/\lambda$  with an NIM of  $n_3 = -1$ , where  $T_{prop}$  and  $T_{evan}$  denote the transmittance by propagating waves and by photon tunneling, respectively, and  $T_h = T_{prop} + T_{evan}$  is calculated from Equation (3.7).

to  $\varepsilon_1 = \mu_1 = -1$ . When  $\theta_1 < \theta_c$ , there exist propagating waves in all layers and interferences in the intermediate layers cause the oscillation in the transmittance. When  $\theta_1 > \theta_c$ , the transmission of radiative energy is through photon tunneling. In the case when  $d_3 = d_2$ , the phase shifts of propagating waves through layers 2 and 3 cancel each other, and no energy is reflected back to medium 1. For  $\theta_1 > \theta_c$ , all the incident energy is transmitted by photon tunneling when  $d_3 = d_2$ . This is because the amplitude increases and decreases by exactly the same amount in layers 2 and 3, respectively. Therefore, the

hemispherical transmittance becomes 1 when  $d_3 = d_2$ . When  $d_3 = 0$ , the situation is the same as that without the NIM. The hemispherical transmittance vs.  $d_2/\lambda$  is shown in Figure 3.8. The transmittance approaches 1 when  $d_2 \ll \lambda$ . As  $d_2$  increases, the contribution of photon tunneling decays rapidly and becomes negligible when  $d_2 \approx \lambda$ . By comparing Figures 3.7 and 3.8, it is clear that the insert of a NIM can greatly enhance photon tunneling and increase the hemispherical transmittance.

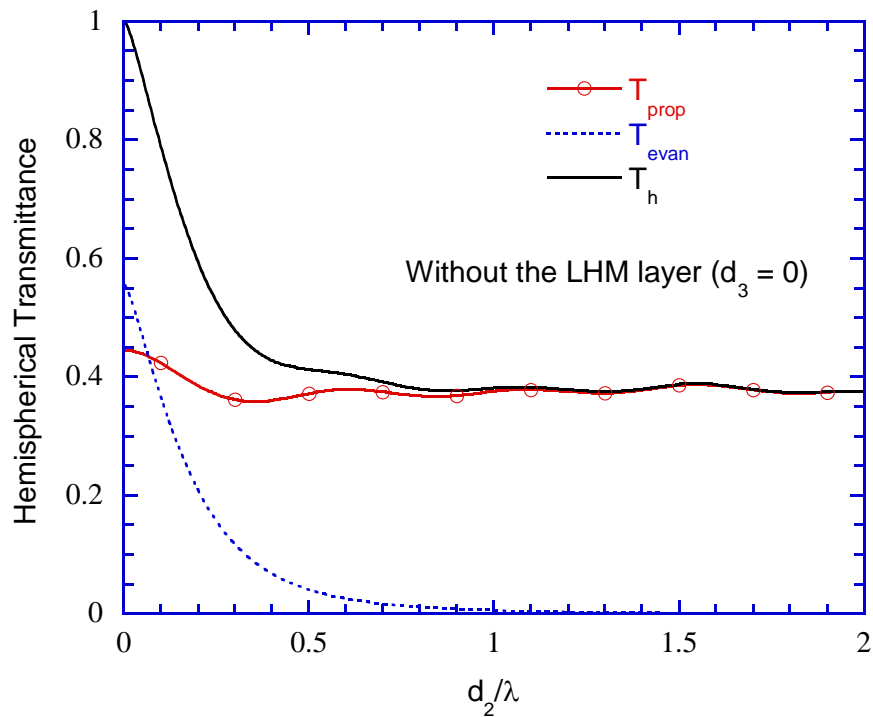


Figure 3.8 The hemispherical transmittance of the layered structure, without the NIM layer, as a function of  $d_2/\lambda$ . The contribution of photon tunneling is negligible if  $d_2/\lambda > 1$ .

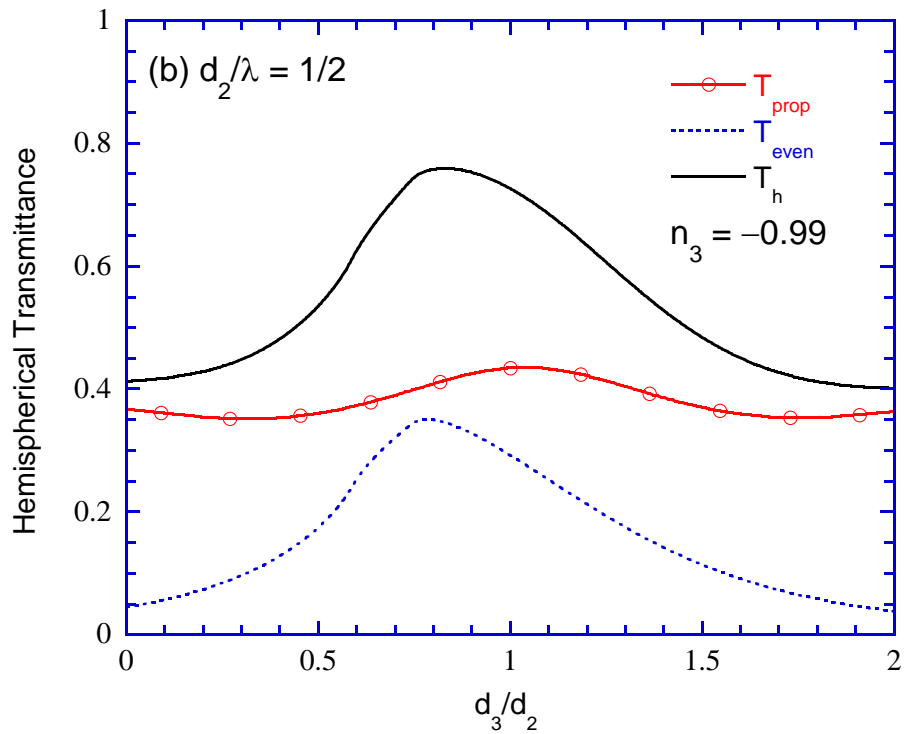
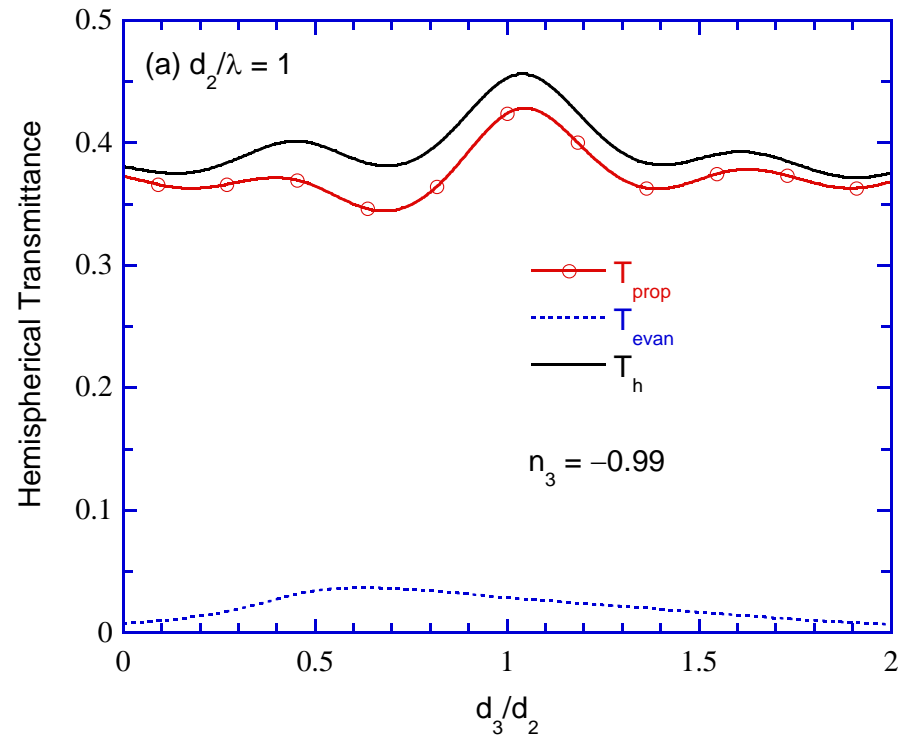


Figure 3.9 The hemispherical transmittance versus  $d_3/d_2$  for  $n_3 = -0.99$ : (a)  $d_2/\lambda = 1$ ; (b)  $d_2/\lambda = 1/2$ .



When  $n_3$  is slightly different from  $-1$  (say,  $n_3 = -0.99$ ), some radiation will be reflected back to medium 1. There exist two critical angles,  $\theta_{c,2}$  and  $\theta_{c,3}$ . The difference between them is very small for a small deviation of  $n_3$  from  $-1$ . When  $\theta_1$  falls in between the two critical angles, the transmitted radiative energy is negligible unless the width of the layer, where an evanescent wave exists, is much smaller than the wavelength. The calculated  $T_h$  is shown in Figure 3.9 (a) for  $d_2 = \lambda$  as a function of  $d_3/d_2$ . It can be seen that the contribution of photon tunneling to the spectral hemispherical transmittance decreases dramatically due to a slight variation of  $n_3$  from  $-1$ . For  $d_2 = \lambda$ , the transmittance by photon tunneling  $T_{evan}$  reaches its maximum at about  $d_3 = 0.55d_2$ , and it only accounts for about 10% of the hemispherical transmittance  $T_h$ . The maximum transmittance by propagating waves  $T_{prop}$  is obtained at  $d_3 = 1.05d_2$  as a result of the wave interference. The phase lags of all propagating waves through layers 2 and 3 cannot be completely cancelled out in this case. When  $d_2 = 0.5\lambda$  as shown in Figure 3.9 (b), however, the contribution to the transmittance by photon tunneling is comparable to that by propagating waves at  $d_3$  near  $0.8d_2$ , where a peak hemispherical transmittance of 0.76 can be obtained.

### 3.4 Considering the Dispersion and Loss of an NIM

It has been shown that  $\varepsilon$  and  $\mu$  of an NIM must be inherently dependent on the frequency (Veselago, 1968). Both  $\varepsilon$  and  $\mu$  are in general complex, absorption and losses can be significant. All the case studied above did not consider the effect of dispersion and loss on photon tunneling. Therefore, the frequency-dependent complex  $\varepsilon$  and  $\mu$  are

considered in this section, and the physical mechanism for the enhanced photon tunneling is analyzed in terms of the excitation of a surface plasmon resonance.

The frequency-dependent  $\varepsilon$  and  $\mu$  of the NIM are taken as Equations (2.5) and (2.6), respectively. In the present study, the following parameters are chosen as  $\omega_0 = 0.5\omega_p$ ,  $F = 0.785$ , and  $\gamma_e = \gamma_m = \gamma$  with  $\gamma$  allowed to vary from zero to a small fraction of  $\omega_p$ . Because of the scaling capability of the metamaterial (Yen, 2004), the frequency is normalized to  $\omega_p$  in all the calculated results. The complex refractive index  $\tilde{n}(\omega)$  of the NIM is then calculated from Equation (2.7) and the calculated  $n$  and  $\kappa$  are plotted in Figure 3.10 as functions of the dimensionless frequency  $\omega/\omega_p$  for  $\gamma$  equal to

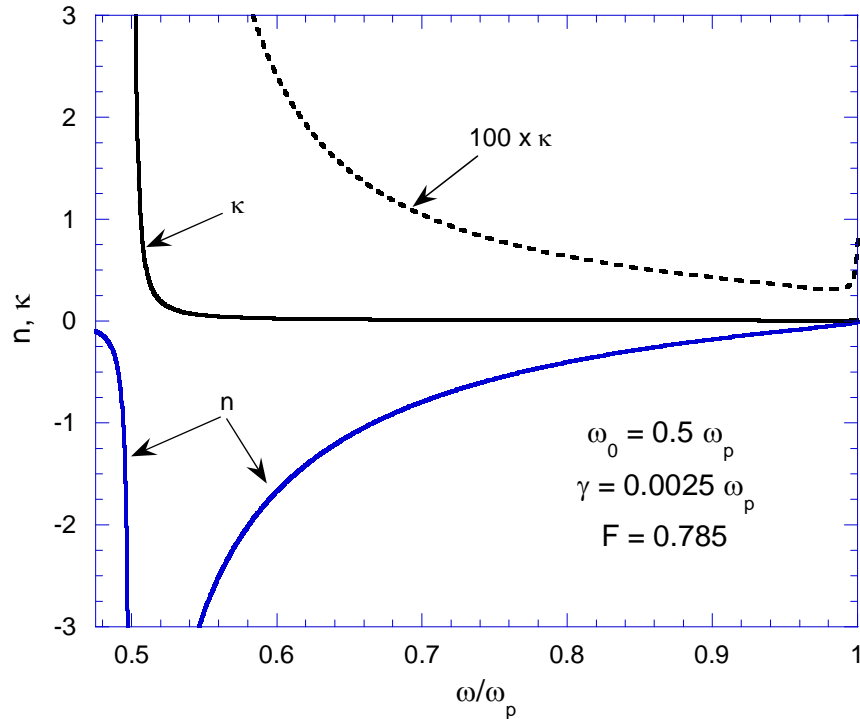


Figure 3.10 Refractive index  $n$  and extinction coefficient  $\kappa$  of an NIM, calculated from Equations (2.5) – (2.6) as functions of the dimensionless frequency  $\omega/\omega_p$ . The dashed line shows the  $\kappa$  values multiplied by 100.

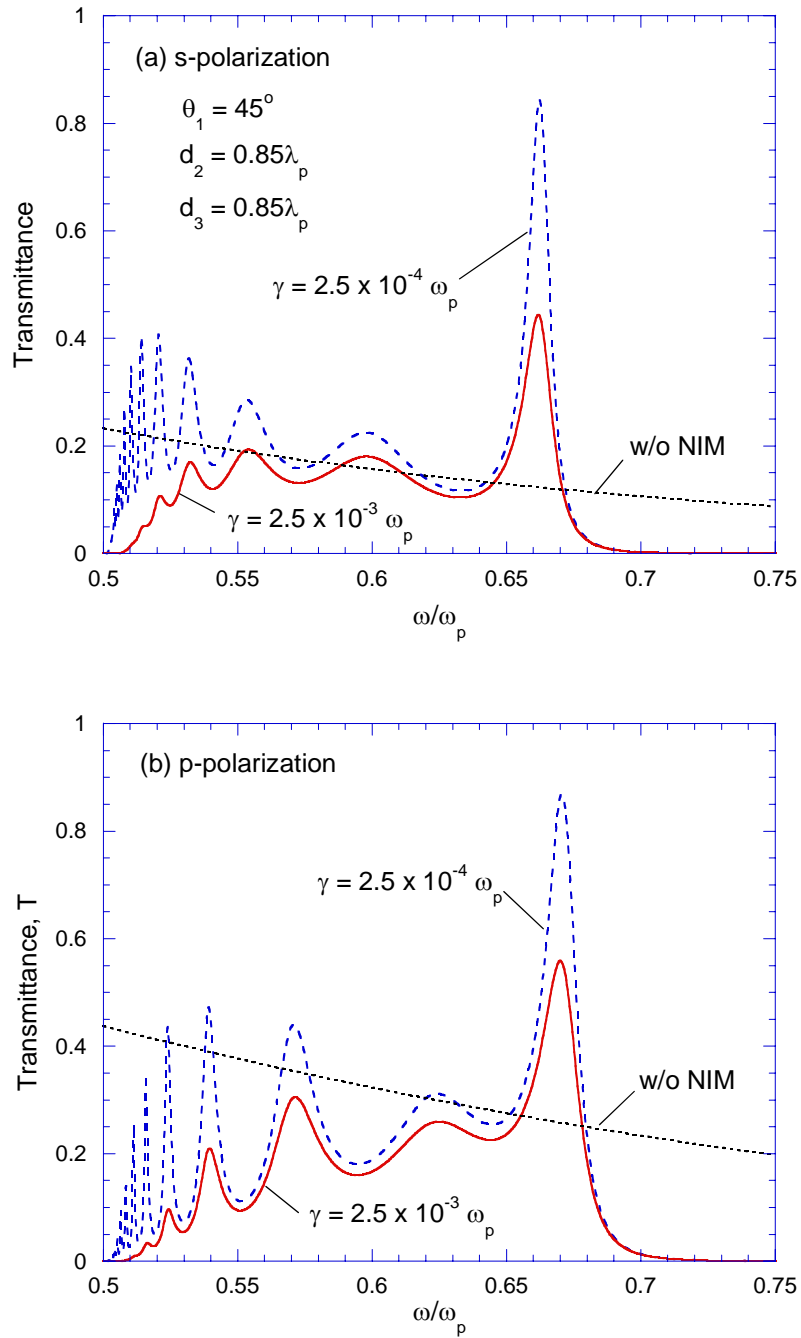


Figure 3.11 Spectral transmittance of a four-layer structure at  $45^\circ$  incidence angle: (a)  $s$ -polarization; (b)  $p$ -polarization. The transmittance without an NIM layer ( $d_3 = 0$ ) is also shown for comparison.

$0.0025\omega_p$ . It can be seen that in the frequency range from  $\omega_0$  to  $\omega_p$ , where the real parts of  $\epsilon$  and  $\mu$  are negative,  $n$  is negative and  $\kappa$  (for small values of  $\gamma$ ) is small at frequencies not too close to  $\omega_0$ .

Still consider the four-layer structure similar to that used in previous sections except that  $\epsilon_3$  and  $\mu_3$  of the NIM are calculated from Equations (2.5) and (2.6). The calculated spectral transmittance at  $45^\circ$  angle of incidence is plotted in Figure 3.11, for  $\gamma = 0.0025\omega_p$  and  $0.00025\omega_p$ , and compared with the case without the NIM layer ( $d_3 = 0$ ). The vacuum gap width ( $d_2$ ) and the NIM layer thickness ( $d_3$ ) are both set to  $0.85\lambda_p$ , where  $\lambda_p = 2\pi c/\omega_p$  is the wavelength corresponding to the plasma frequency. The dimensionless approach allows the results to be scalable toward different electromagnetic spectral regions, once suitable negative index materials are available. For both polarizations, the transmittance oscillates in the frequency range from  $0.5 < \omega/\omega_p < 0.7$ , with a distinct peak between 0.65 and 0.68, and then goes to zero abruptly. The oscillation in the transmittance at  $\omega/\omega_p < 0.65$  is due to the interference of propagating waves inside the NIM layer, coupled with the photon tunneling transmission through the vacuum gap. On the other hand, the peak transmittance is due to the excitation of a surface plasmon polariton (SPP) at the interface between the vacuum and NIM.

A surface plasmon polariton (SPP) is a coupled, localized electromagnetic wave that propagates along the interface of two different media. The fields extend into both media and decay exponentially away from the interface (Raether, 1988; Wallis, 1985). The dispersion relations of SPPs at the interface of vacuum (layer 2) and an NIM (layer 3) are given by the following equations if loss in the NIM is negligible (Ruppin, 2000).

$$\frac{\beta_2}{\mu_2} + \frac{\beta_3}{\mu_3} = 0, \text{ for } s\text{-polarization} \quad (3.8)$$

and 
$$\frac{\beta_2}{\varepsilon_2} + \frac{\beta_3}{\varepsilon_3} = 0, \text{ for } p\text{-polarization} \quad (3.9)$$

where  $\beta_l$  is positive and related to the wave vector by  $\beta_l = (k_x^2 - \varepsilon_l \mu_l \omega^2 / c^2)^{1/2}$ ,  $l = 2$  or  $3$ . For  $\beta$  to be positive,  $k_{lz}$  must be purely imaginary. Another necessary criterion for surface polariton to exist is that  $\mu_3 < 0$  for  $s$ -polarization and  $\varepsilon_3 < 0$  for  $p$ -polarization.

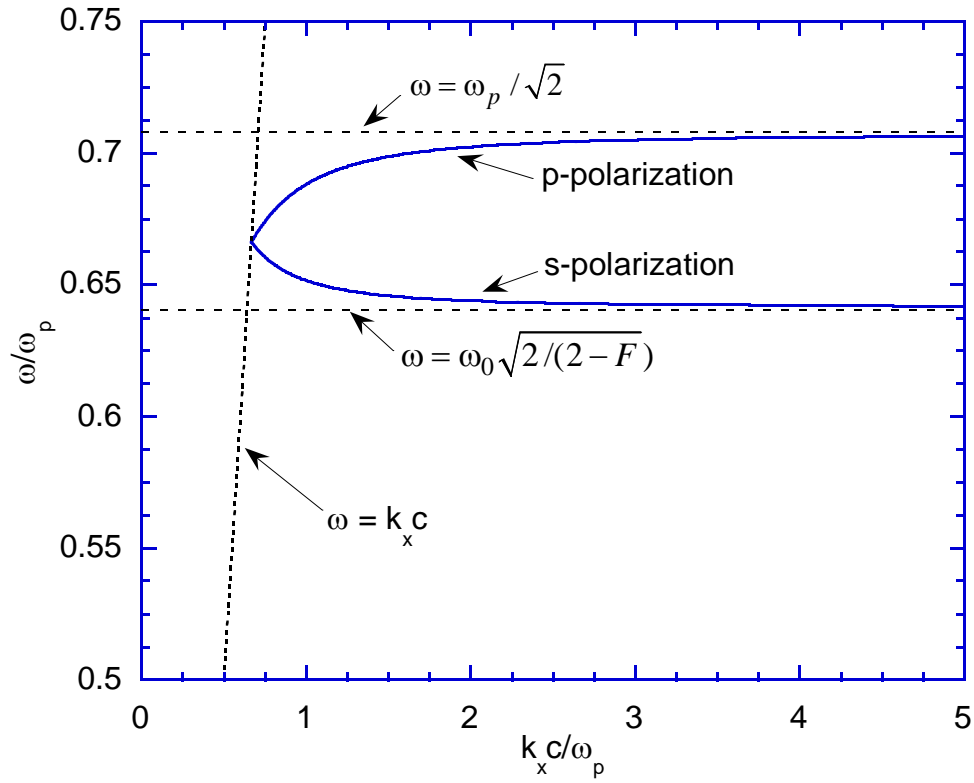


Figure 3.12 Dispersion curves of SPPs excited at the interface of a semi-infinite vacuum and a semi-infinite NIM, where  $\varepsilon$  and  $\mu$  for the NIM are calculated from Equations (3.8) and (3.9) with  $\gamma = 0$ .

The simultaneous negative  $\varepsilon$  and  $\mu$  in an NIM allow SPPs to be excited for both polarizations in the same frequency region. The dispersion relations of SPPs at the interface of vacuum and an NIM are plotted in Figure 3.12 using Equations (3.8) and (3.9). Note that  $\varepsilon$  and  $\mu$  for the NIM in Equations (3.8) and (3.9) are calculated from Equations (2.5) and (2.6) with neglecting  $\gamma$ . The straight line in Figure 3.12 represents the dispersion relation for a propagating electromagnetic wave in vacuum; the  $s$ - and  $p$ -polarized SPP dispersion curves lie entirely to the right of this line and approach the asymptotical values corresponding to  $\varepsilon = -1$  and  $\mu = -1$  of the NIM, respectively. Applying Equations (3.8) and (3.9) to the four-layer structure and rewrite the SPP dispersion relations in terms of the incidence angle  $\theta_1$ , under the assumption that  $\gamma = 0$ , one obtains

$$\sin \theta_1 = \frac{1}{n_1} \left( \frac{\mu_3^2 - \mu_3 \varepsilon_3}{\mu_3^2 - 1} \right)^{1/2}, \text{ for } s\text{-polarization} \quad (3.10)$$

and

$$\sin \theta_1 = \frac{1}{n_1} \left( \frac{\varepsilon_3^2 - \varepsilon_3 \mu_3}{\varepsilon_3^2 - 1} \right)^{1/2}, \text{ for } p\text{-polarization} \quad (3.11)$$

These two equations link the frequency  $\omega_{spp}$  at which SPPs may be excited with the incidence angle. Table 3.1 compares the  $\omega_{spp}$  calculated from Equations (3.10) and (3.11) at different incidence angles with the frequency at which the transmittance is maximum for the case with  $\gamma = 0.0025\omega_p$ . The agreement is very good, especially at larger incidence angles. The small deviation at  $\theta_1$  close to the critical angle  $\theta_c$  is caused by the disturbance of end layers because the derivation of Equations (3.10) and (3.11) assumes that the vacuum gap and the NIM layer extend to infinity. The effect of nonzero  $\gamma$  on

$\omega_{spp}$  is negligibly small because the small value of  $\gamma$  used. Nevertheless,  $\gamma$  can affect the magnitude of the transmittance and reducing  $\gamma$  can increase the transmittance. These sharp peaks of transmittance due to SPP excitations suggest a possible way to build new optical resonators, similar to the Fabry-Perot resonators (Yeh, 1988; Kumar et al., 2000), which have important applications in optoelectronics and optical communications.

Table 3.1 Comparison of the SPP resonance frequency  $\omega_{spp}$  calculated from Equations (3.10) and (3.11) to the resonance frequency obtained from the transmittance maximum for the four-layer structure.

| Incidence angle | $\omega_{spp} / \omega_p$ for <i>s</i> -polarization |                       | $\omega_{spp} / \omega_p$ for <i>p</i> -polarization |                       |
|-----------------|--|-----------------------|--|-----------------------|
|                 | Equation (3.10)                                      | Transmittance maximum | Equation (3.11)                                      | Transmittance maximum |
| 42°             | 0.66600  | 0.66350               | 0.66650  | 0.66550               |
| 45°             | 0.66325  | 0.66175               | 0.67075  | 0.67025               |
| 50°             | 0.65975  | 0.65925               | 0.67625  | 0.67625               |
| 55°             | 0.65750  | 0.65725               | 0.68025  | 0.68050               |
| 60°             | 0.65550  | 0.65550               | 0.68325  | 0.68350               |

Because both  $d_2$  and  $d_3$  are finite, the matching of thickness is critical for transmittance enhancement. In the lossless case,  $\beta_2 d_2 = \beta_3 d_3$  has been shown to be a phase matching condition (Zhang and Fu, 2002; Fu and Zhang, 2003) because it will result in a transmittance of unity. When loss is included, an optimum value of  $d_3$  that results in maximum transmittance still exists but the optimization condition can no longer

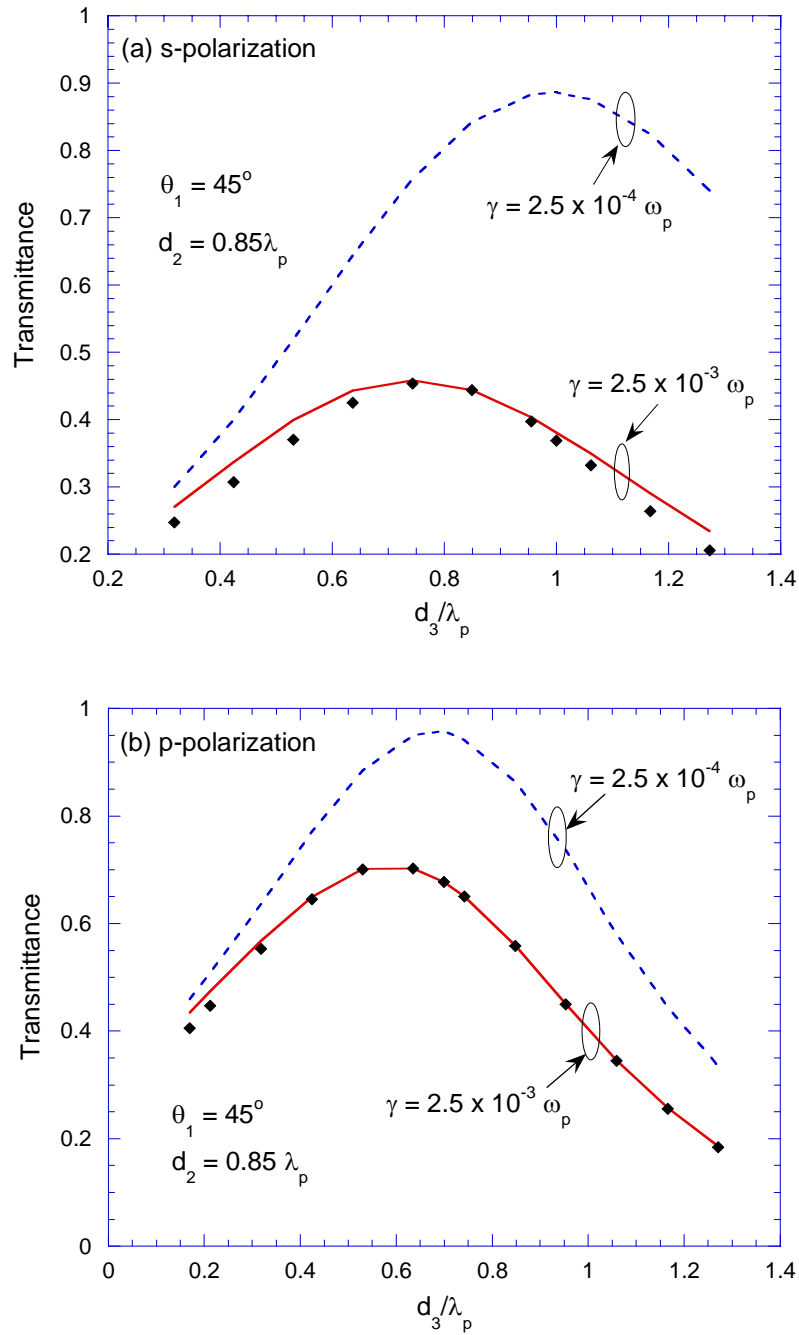


Figure 3.13 Peak transmittance of the 4-layer structure versus the thickness of the NIM for incidence angle of  $45^\circ$  and when  $d_2$  is fixed at  $0.85\lambda_p$ : (a) *s*-polarization; (b) *p*-polarization. The squares correspond to the transmittance calculated at  $\omega_{spp} = 0.66175\omega_p$  for *s*-polarization and  $\omega_{spp} = 0.67025\omega_p$  for *p*-polarization.



be expressed by such a simple relation. The maximum transmittance of the four-layer structure as a function of  $d_3$  is shown in Figure 3.13 for different  $\gamma$  values, where the vacuum gap width is fixed to  $d_2 = 0.85\lambda_p$ . The squares denote the transmittance calculated at the frequency equal to  $\omega_{spp} = 0.66175\omega_p$  for  $s$ -polarization and  $\omega_{spp} = 0.67025\omega_p$  for  $p$ -polarization. The deviation of the squares from the solid curve is due to the disturbance of the end layers that shifts the polariton resonance frequency slightly. The value of  $d_3$  that results in a maximum transmittance depends on the polarization because the SPP frequencies are different. As  $d_3$  increases, the transmittance first increases, reaches a maximum at a certain  $d_3$ , and then decreases when  $d_3$  is further increased. Using  $d_3 = d_2\beta_2/\beta_3$  and under the lossless condition, the estimated optimal thickness  $d_3 = 1.02\lambda_p$  for  $s$ -polarization and  $0.7\lambda_p$  for  $p$ -polarization, close to values for  $\gamma = 0.00025\omega_p$  as shown in Figure 3.13. As  $\gamma$  is increased to  $0.0025\omega_p$ , the optimal  $d_3$  decreases, indicating that absorption in the NIM layer shifts the optimal thickness  $d_3$  to a smaller value.

### 3.5 Employing NIMs in a Multilayer Structure of More than Four Layers

Polaritons can be excited at both surfaces of the NIM slab (Ruppin, 2001). Both surface and bulk polaritons may play a role to affect the radiative properties (Park et al., 2004). To explore the effect of double-surface polaritons and bulk polaritons on photon tunneling, a five-layer structure can be constructed by subdividing the vacuum gap into two layers, each having half of the thickness, that sandwich the NIM layer. The total thickness of the vacuum gaps and thickness of the NIM layer remain at  $0.85\lambda_p$ , the same

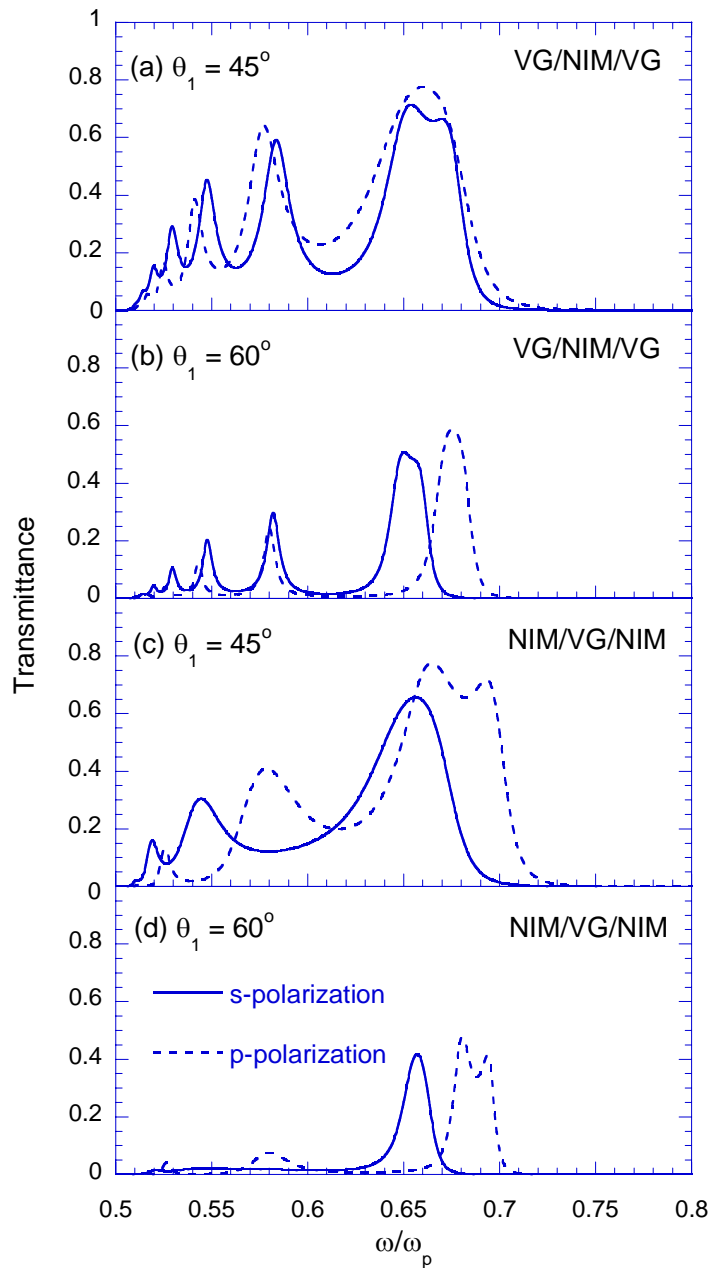


Figure 3.14 The transmittance spectra of a 5-layer structure for  $\gamma = 0.0025\omega_p$ . In (a) and (b), the vacuum gap (VG) is equally divided into two layers sandwiching the NIM layer. The total thickness of the VGs and the thickness of the NIM layer are the same as in Figure 4, i.e.,  $0.85\lambda_p$ . In (c) and (d), the NIM layer is equally divided into two layers that sandwich the VG.

as in Figure 3.11. The results for both  $s$ - and  $p$ -polarizations are plotted in Figure 3.14(a) for  $\theta_1 = 45^\circ$  and 3.14(b) for  $\theta_1 = 60^\circ$ . It can be seen from Figure 3.14(a) that the transmittance near the SPP frequency is increased remarkably compared with Figure 3.11. Furthermore, the full-width-at-half-maximum of the peak is significantly broadened. In particular, the peak at the SPP frequency for  $s$ -polarization has been split into two peaks. This change of the transmittance profile is because SPPs are excited at both surfaces of the NIM layer. The fields of the SPPs decay in opposite directions inside the NIM from both surfaces and can couple with each other, resulting in split of each polariton mode into two new ones (Raether, 1988; Ruppin, 2001). The split of the SPP mode depends on the field coupling strength. It follows that the split SPP modes tend to be more separated for a thinner NIM layer while they shift to each other for a thicker NIM layer and eventually the fields inside the NIM decouple and the split SPP modes restore when the NIM thickness approaches infinity. The broadening of the transmittance peak shown in Figure 3.14(a) is because the two split SPP modes are very close to each other, especially for  $p$ -polarization, such that the corresponding two peaks overlap. The field reinforcement inside the NIM due to the coupling gives rise to the large enhancement of the tunneling transmittance and this enhancement is more remarkable at larger incidence angles, such as the case shown in Figure 3.14(b) with the transmittance is over 20 times greater than that without an NIM layer.

An alternative way to construct a five-layer structure is to place the vacuum gap in the middle and subdivide the NIM into two layers located between the vacuum gap and a dielectric. The transmittance of this five-layer structure is shown in Figures 3.14(c) and 3.14(d) for an incidence angle equal to  $45^\circ$  and  $60^\circ$ , respectively. The label

NIM/VG/NIM indicates that the vacuum gap (VG) is between two subdivided NIM layers. In the calculation, the vacuum gap thickness and the total NIM thickness are still equal to  $0.85\lambda_p$ . The transmittance features due to SPP excitation are similar to those seen in Figures 3.14(a) and 3.14(b), except that discernable split of the peak is for  $p$ -polarization instead of  $s$ -polarization. On the other hand, when compared the transmittance spectra for  $\omega/\omega_p < 0.6$ , large oscillation in the transmittance with a series of peaks can be seen in Figures 3.14(a) and 3.14(b) but not in Figures 3.14(c) and 3.14(d), where the transmittance is smaller and less oscillating. The reason for this difference is that the transmittance is enhanced in the case with VG/NIM/VG by the excitation of the waveguide modes or bulk polaritons inside the NIM layer, but there are no bulk polaritons in Figures 3.14(c) and 3.14(d). A bulk polariton can only be excited in a slab and is characterized by the fields decaying exponentially outside the slab but oscillating as a standing wave inside the slab. Therefore, a slab should have a larger refractive index than its surrounding media in order to sustain bulk polaritons; this is the case in Figures 3.14(a) and 3.14(b). A detailed discussion of the dispersion relations of bulk polaritons can be found in the work of Park et al. (2004). The transmittance peaks for  $\omega/\omega_p < 0.6$  in Figures 3.14(a) and 3.14(b) correspond to the modes of bulk polaritons excited in the NIM slab. Bulk polaritons have important applications in integrated optical waveguides (Buckman, 1992) and for inducing resonant tunneling superlattices (Yeh, 1985). Figure 3.14 demonstrates that an NIM slab which sustains bulk polaritons can enhance radiative energy transmission via photon tunneling.

The focusing capability of an NIM slab has been the most promising application of these metamaterials. Challenges remain to reduce the losses in practical devices.

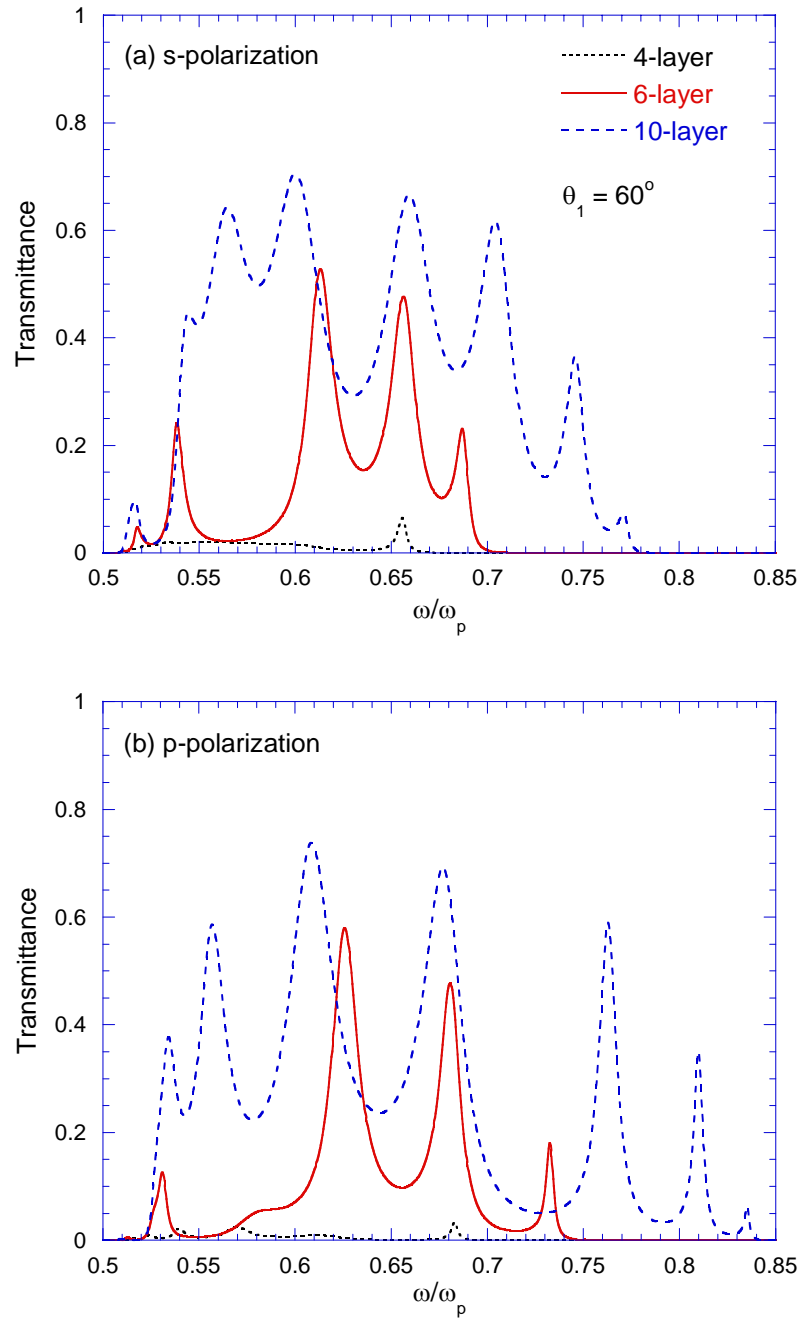


Figure 3.15 The transmittance spectra of multilayer structures with different numbers of layers at an incidence angle  $\theta_1 = 60^\circ$ : (a) *s*-polarization, (b) *p*-polarization. In each multilayer structure a VG and an NIM layer of the same thickness are alternately placed between the two end layers. The total thickness of the VGs is the same as the total thickness of the NIM layers and is set to  $0.85\lambda_p$ , the same as in Figures 3.11.

Ramakrishna et al. (2003) and Gao and Tang (2004) showed that the image resolution could be improved by dividing the NIM slab used in the imaging device into many thinner lamellae and it was thought that the subdivision would result in a reduced absorption in the NIM. Many thinner NIM layers, when placed alternatively with vacuum gaps, can cause stronger field coupling inside the structure when SPPs are excited. Therefore better enhancement of photon tunneling may be achieved. For instance, a 6-layer structure can be made by dividing the vacuum gap and the NIM layer each into two sub-layers and placing them alternately between the two end dielectrics. A 10-layer structure can be constructed by doubling the number of vacuum gaps and NIM layers without increasing the total thicknesses. The transmittance of multilayer structures calculated using the matrix formulation is shown in Figures 3.15(a) for *s*-polarization and 3.15(b) for *p*-polarization, at 60° incidence angle. Clearly, the transmittance increases after each division and the frequency range over which significant tunneling can be observed is greatly broadened by subdividing the layers. The subdividing process results in more bulk polaritons or SPPs being excited and coupling inside the structure. The dispersion relations of bulk and surface modes are very complicated when the structure consists of many layers. Nevertheless, when the layers between the two end dielectrics become thinner and thinner, the stronger SPP coupling will result in many splittings of the surface modes such that some modes shift to higher frequencies and broaden the passband while some other modes shift to lower frequencies and can transform to bulk polaritons (Park et al., 2004).

In order to understand the radiative properties for both propagating modes and evanescent modes, the transmittance and absorptance at a single frequency  $\omega = 0.665\omega_p$

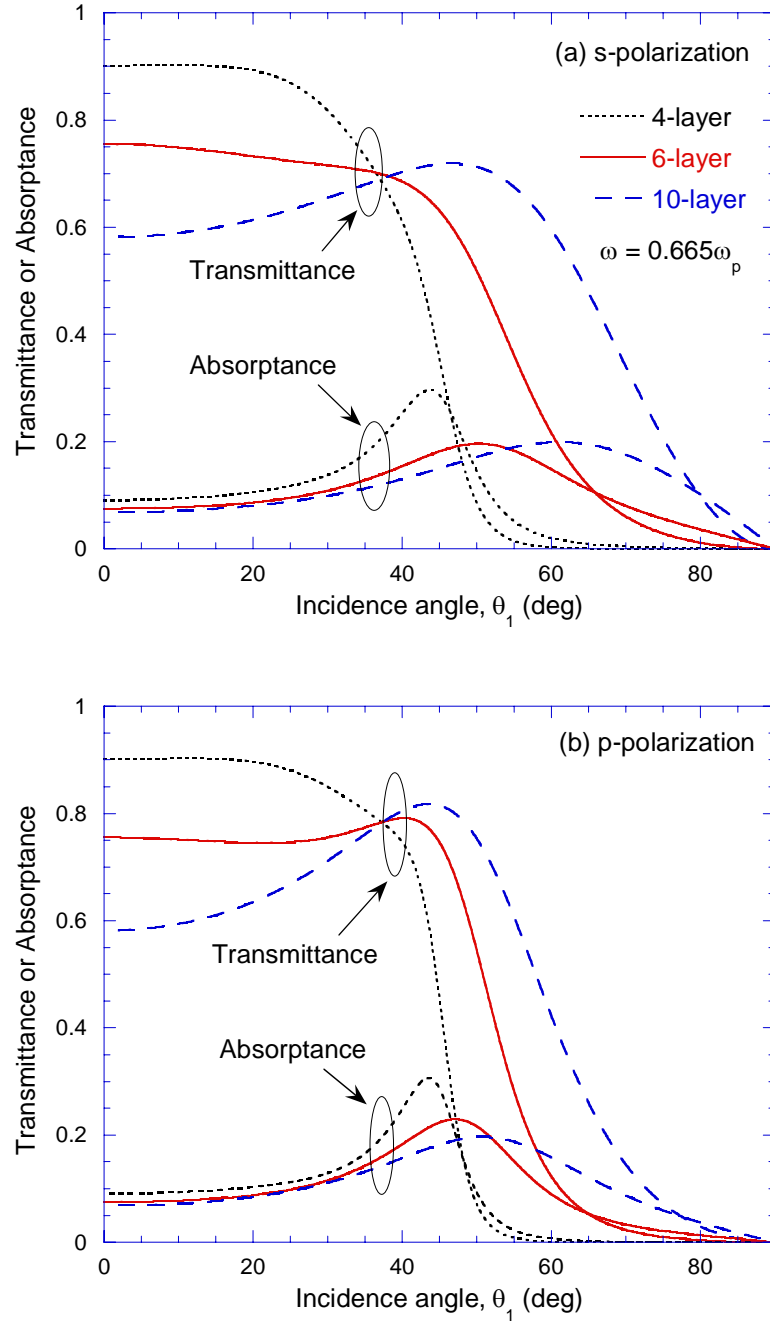


Figure 3.16 The transmittance and absorptance of multilayer structures, with different number of layers, versus the incidence angle  $\theta_1$ . (a) *s*-polarization, (b) *p*-polarization. The configurations are the same as corresponding ones in Figure 3.15 and the frequency is fixed at  $\omega = 0.665\omega_p$ .

is plotted in Figures 3.16(a) for  $s$ -polarization and 3.16(b) for  $p$ -polarization, as a function of the incidence angle. When the incidence angle is smaller than the critical angle ( $42^\circ$  in this case), the radiative properties are affected by multiple reflections and interferences of the propagating waves in the layered structure. Consequently, a decrease in transmittance is observed when the layer number is increased from 4 to 10, presumably due to the enhancement of reflectance as more boundaries are added. On the other hand, when the incidence angle is greater than the critical angle, bulk polaritons and surface polaritons may be excited and may interact with each other to enhance the electromagnetic field in the structure, resulting in an enhancement in the transmittance as the number of layer is increased. Increasing the magnitude of evanescent waves at the image plane is key to the improved image quality using NIM multilayer structures (Ramakrishna et al., 2003; Gao and Tang, 2004). Contrary to intuition, however, the enhancement in transmission is not necessarily due to a reduction of absorption by subdivision of the NIM layers. It can be seen from Figure 3.16 that the absorptance increases with the number of layers at large incidence angles, where the enhanced transmission of evanescent waves is associated with a reduction of reflection.



## CHAPTER 4

### A COHERENT THERMAL EMISSION SOURCE BY PAIRING A LAYER OF NEGATIVE $\epsilon$ WITH A LAYER OF NEGATIVE $\mu$

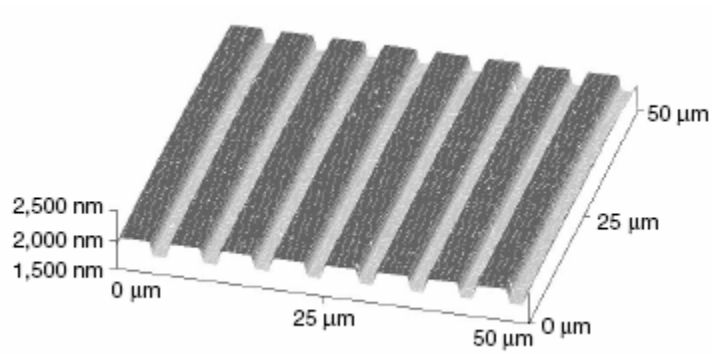
A coherent emission source, such as a laser or an antenna, is manifested by its emission being highly monochromatic and directional. In contrast, radiation from a thermal source, as illustrated in Figure 2.6(a), is produced by the randomly fluctuating electric (and magnetic, for magnetic materials) currents inside the thermal source. The EM waves emitted from the randomly fluctuating currents have a wide range of frequencies and propagate in many directions such that they cannot produce constructive interference in particular directions. Therefore, a thermal source is usually presented as a typical example of an incoherent emission source. However, it has been demonstrated that by etching a periodic grating on the surface of heavily doped silicon (Hesketh et al., 1986 and 1988), silicon carbide (SiC) (Greffet et al., 2002), and gold (Kreiter, 1999), thermal emission from the material can exhibit coherent properties in the optical or infrared region, producing lobes of radiation restricted to small solid angles and in well-defined directions. Such a thermal source has much higher directional spectral emissivity at some particular frequencies and in some particular directions than a thermal source of the same material but without the grating, allowing more radiative energy to be emitted. Therefore, a coherent thermal emission source may have potential applications in “radiative cooling” and in infrared photovoltaic devices (Greffet et al., 2002).

The physical mechanism underlying the coherent thermal emission is due to the excitation of surface polaritons on the surface of the source material and the coupling of surface polaritons with thermal emission when diffracted by the grating. It has been

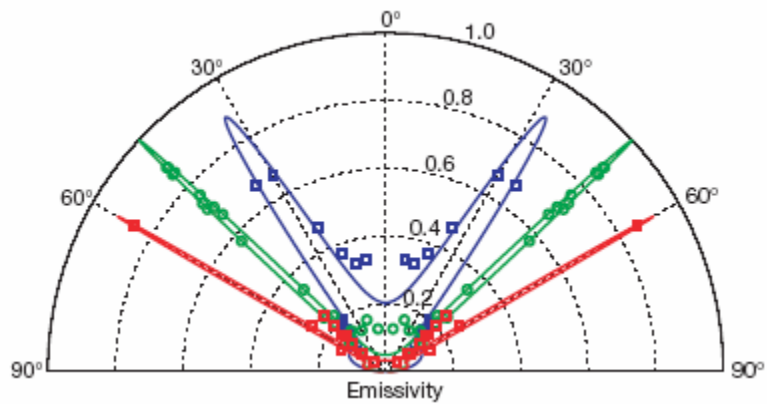
known from Chapter 3 that surface polaritons are evanescent and cannot couple directly with propagating waves because surface polaritons have a wavevector magnitude greater than that of the propagating waves. By etching a grating on the surface, however, surface polaritons can couple with propagating waves. The relation between the emission angle  $\theta_1$  and the wavevector magnitude  $k$  is given by the simple grating equation

$$k_{SP} = k \sin \theta_1 + m \frac{2\pi}{d} \quad (4.1)$$

where  $m$  is an integer,  $k_{SP}$  is the wavevector magnitude of the surface polaritons and  $d$  is the periodicity of the grating. The existence of surface polaritons requires the source material to have a negative real part of the dielectric function. As a consequence, an EM wave incident on the surface of such a material will be highly reflected, denoted by a large value of the directional spectral reflectance  $R$ . From Kirchhoff's law (Siegel and Howell, 2002), the directional spectral emissivity of the material  $\varepsilon = 1 - R$  (assuming an opaque material such that the transmittance  $T = 0$ ) is small though surface polaritons are excited. With gratings, the excited surface polaritons couple with and enhance the thermal radiation in the direction imposed by Eq. (4.1) for a particular wavelength (frequency). But in other directions the directional spectral emissivity is kept in low values such that the emission spectra exhibit narrow angular emission lobes. The experimental results of Greffet et al. (2002) are shown in Figure 4.1 for illustration. Coherent thermal emission from a source as shown in Figure 4.1(a) is only for  $p$ -polarization (emission with electric fields normal to the grooves of the grating) because normal materials do not support surface polaritons of  $s$ -polarization. In this chapter, a new type of coherent thermal emission source is proposed.



(a)



(b)

Figure 4.1 Coherent thermal emission from a grating: (a) geometry of the grating on the surface of a piece of SiC with periodicity  $d = 6.248 \mu\text{m}$  and depth  $h = 0.284 \mu\text{m}$  (b) The experimental results of the directional spectral emissivity obtained from reflectance measurements at room temperature based on Kirchhoff's law, the wavelengths for the angular emission lobes ranging with increasing polar angles are  $11.04 \mu\text{m}$ ,  $11.36 \mu\text{m}$ , and  $11.86 \mu\text{m}$ , respectively (from Greffet et al., 2002).

#### 4.1 Gratingless Coherent Thermal Emission Source

The proposed thermal emission source is constructed with a heterogeneous structure that consists of a thin layer made of a material with a negative permittivity  $\epsilon$  but a positive permeability  $\mu$  and a thick substrate with a positive permittivity  $\epsilon$  but negative permeability  $\mu$ , or vice versa. Such a coherent thermal emission source depends on the availability of a material with a negative  $\mu$ . Although a material with a negative  $\mu$  is not found in naturally occurring materials, Pendry et al. (1999) showed that a metamaterial that has a negative  $\mu$  at certain wavelengths or frequency can be constructed from a periodic array of nonmagnetic, conducting, split-ring resonators (SRRs). Many metals and polar dielectrics have a negative  $\epsilon$  in the visible and infrared, and periodic structures of thin metal wires can dilute the average concentration of electrons and shift the plasma frequency to the far infrared or even GHz bands (Pendry et al., 1996). The SRR structure and thin metal wire structure have been used by Shelby et al. (2001) to realize an NIM metamaterial at X-band microwave frequencies by carefully tuning the geometry of the SRR structure and the thin metal wire structure and embedding them on opposite sides of interlocking standard circuit boards. But only the SRR alone, its permittivity  $\epsilon$  has been shown to be positive (Smith et al., 2002). A recent experiment (Yen et al., 2004) has shown that a negative  $\mu$  at higher frequencies can be achieved by scaling down the dimensions of the SRR structure. Podolskiy et al. (2002) also proposed a novel nanowire-pair composite for achieving a negative  $\mu$  at higher frequencies. Therefore, the heterogeneous structure is assumed possible to make using metamaterials and may be much easier to make than the NIM prototype of Shelby et al. (2001). It will be shown that coherent thermal emission from such a heterogeneous structure is possible

for both  $s$ - and  $p$ -polarizations. The coherent thermal emission is from a smooth surface (no grating). The mechanism for the coherent thermal emission is still due to surface polariton excitation, but at the interface of the heterogeneous structure. A similar structure composed of two lossless thin layers has been studied by Alu and Engheta (2003). They found that the structure can act, in some aspects, similar to a negative index material, and thus may be used for super-resolution imaging.

#### 4.2 Surface Polariton Dispersion Relations at the Interface of the Bilayer

Consider a plane wave incident from vacuum onto the heterogeneous bilayer structure, shown in Figure 4.2(a). For convenience, the semi-infinite medium (vacuum) in which the wave originates is labeled as medium 1 ( $\epsilon_1 = \mu_1 = 1$ ); medium 2 (thickness  $d_2$ ) is the layer with a negative  $\epsilon$  and medium 3 is the substrate with a negative  $\mu$ . Assume that the plane wave of frequency  $\omega$  is incident at angle  $\theta_1$ . The normal component of the wave vector in medium  $l$  ( $l = 1,2,3$ ) reads  $k_{lz} = \left(\omega^2 \epsilon_l \mu_l / c^2 - k_x^2\right)^{1/2}$  where  $c$  denotes the speed of light in vacuum,  $k_x$  is the parallel component of the wave vector and is given by  $k_x = \omega \sin \theta_1 / c$ . (This parallel component is the same in all media.). Because  $\epsilon$  and  $\mu$  have opposite signs in the bilayer structure,  $k_{2z}$  and  $k_{3z}$  are purely imaginary when loss is neglected. A surface polariton is possible to be excited at the interface of medium 2 and medium 3 as long as the surface polariton dispersion relations are satisfied, which is the same as Equations (3.8) and (3.9). For convenient discussion, these two equations are rewritten as

$$\frac{k_{2z}}{\mu_2} + \frac{k_{3z}}{\mu_3} = 0, \text{ for } s\text{-polarization} \quad (4.2)$$

and 
$$\frac{k_{2z}}{\varepsilon_2} + \frac{k_{3z}}{\varepsilon_3} = 0, \text{ for } p\text{-polarization} \quad (4.3)$$

Surface polaritons of both polarizations are possible to be excited since  $\varepsilon_2$  and  $\varepsilon_3$  as well as  $\mu_2$  and  $\mu_3$  are assumed opposite signs in the heterogeneous structure.

As mentioned earlier, a metal wire structure can be used to achieve a negative  $\varepsilon$  for medium 2 and a split-ring resonator structure can be used to achieve a negative  $\mu$  for medium 3. In reality, dispersion and losses are inevitable. Following the discussion by Pendry et al. (1996, 1999), the following expressions are chosen to describe the electric and magnetic behaviors of media 2 and 3:

$$\varepsilon_2(\omega) = 1 - \frac{\omega_p^2}{\omega^2 + i\gamma_e\omega} \quad \text{and} \quad \mu_2(\omega) = 1 \quad (4.4)$$

$$\mu_3(\omega) = 1 - \frac{F\omega^2}{\omega^2 - \omega_0^2 + i\gamma_m\omega} \quad \text{and} \quad \varepsilon_3(\omega) = \varepsilon_3 \quad (4.5)$$

Here,  $\omega_p$ ,  $\omega_0$ ,  $F$ , and  $\gamma_e$  and  $\gamma_m$  have the same definitions as in Equations (2.5) and (2.6). Although  $\varepsilon_3$  is in general frequency dependent (Smith et al., 2002), for simplicity, it is initially taken to be real, positive, and independent of frequency. Varied values of  $\varepsilon_3$  are used in the subsequent calculations.

The dispersion relations of surface polaritons at the second interface are calculated by substituting Equations (4.4) and (4.5) into the expression for  $k_{Lz}$  and Equations (4.2) and (4.3) and neglecting the effect of loss. In the calculations the values  $\omega_0 = 0.5\omega_p$  and  $F = 0.785$  are taken. The result is shown in Figure 4.2(b) for different values of  $\varepsilon_3$ . The dashed curves and solid curves denote  $s$ - and  $p$ -polarizations,

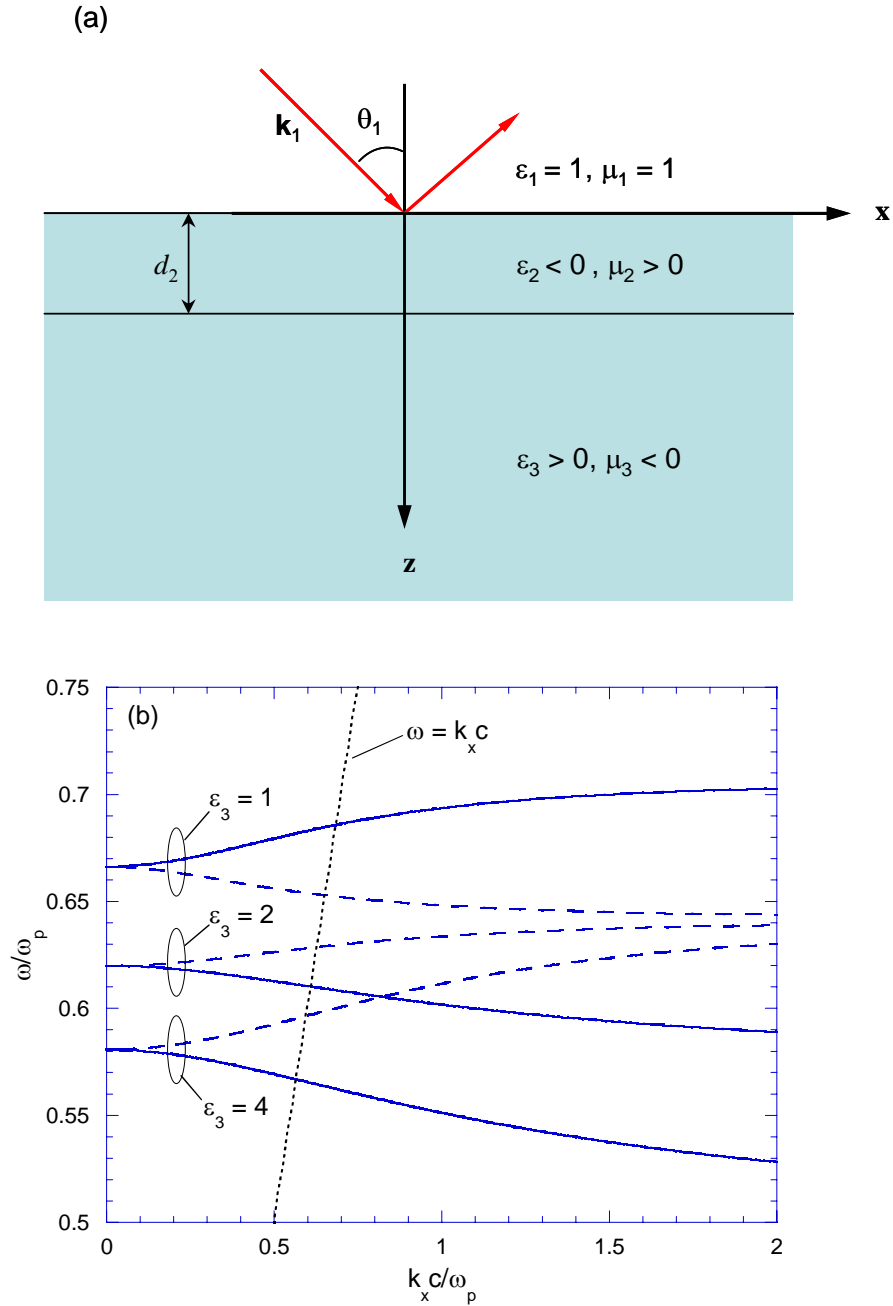


Figure 4.2 A coherent thermal emission source made of a bilayer structure (a) Schematic of the bilayer in vacuum. (b) The dispersion relations of surface polaritons at the interface of the two layers that make the bilayer. The dashed lines are for  $s$ -polarization and solid lines are for  $p$ -polarization. The dotted line represents the dispersion relation in vacuum. Note that surface polaritons can be excited by radiation at normal incidence ( $k_x = 0$ ).

respectively. It is clear that surface polaritons of both polarizations can be excited for this particular bilayer structure. The dotted line represents the dispersion relation of electromagnetic waves in vacuum. It delineates the surface polariton dispersion curves into two regions. Within the region on the right hand side of the dotted line, an evanescent wave is required for the excitation of surface polaritons; within the region on the left hand side of the dotted line, however, surface polaritons can be excited by a propagating wave. The dispersion curves give a non-zero  $\omega$  for  $k_x=0$  ( $\theta_1 = 0$ ), indicating that surface polaritons are excited even at normal incidence. This behavior leads to unique optical properties, discussed in the following paragraphs.

### 4.3 Predicted Results

In order to show that thermal emission from the bilayer can be coherent, the directional spectral emissivity  $\epsilon_\omega$  of the bilayer needs to be calculated. From Kirchhoff's law (Siegel and Howell, 2002),  $\epsilon_\omega$  is simply equal to  $1-R$  for an opaque material, where  $R$  is the directional spectral reflectance of the bilayer and is calculated using the matrix formulae presented in Chapter 2. But it should be noted that if medium 2 and medium 3 are completely lossless,  $R$  is always unity even though surface polaritons are excited. This is because energy dissipation in the heterogeneous structure is zero if both  $k_{2z}$  and  $k_{3z}$  are purely imaginary. Therefore, loss is the key to causing large absorption in the bilayer when surface polaritons are excited. In the calculation, the following parametric values are taken:  $\epsilon_3 = 4$ , medium 2 thickness  $d_2 = 0.425\lambda_p$  where  $\lambda_p = 2\pi c/\omega_p$ , and  $\gamma_e = \gamma_m = 0.0025\omega_p$ . The calculated  $\epsilon_\omega$  of the bilayer at  $30^\circ$  and  $60^\circ$  emission angles is



plotted in Figure 4.3(a) for  $s$ -polarization. It can be seen that  $\epsilon_\omega$  exhibits very large values only in a narrow frequency band, with the center frequency  $\omega_c$  equal to  $0.584\omega_p$  for  $30^\circ$  emission angle and  $0.592\omega_p$  for  $60^\circ$  emission angle, respectively.  $\epsilon_\omega$  at frequencies beyond the narrow band is almost zero. The two center frequencies above are the frequencies of surface polaritons for the two corresponding angles of emission. The full width at half maximum (FWHM) of the narrow frequency band  $\Delta\omega$  is equal to  $6.902 \times 10^{-3}\omega_p$  for  $30^\circ$  emission angle and  $4.871 \times 10^{-3}\omega_p$  for  $60^\circ$  emission angle, which results in the corresponding Q factor ( $\omega_c/\Delta\omega$ ) equal to 85 and 122, respectively. This particular spectrum of the directional spectral emissivity makes thermal emission from the bilayer exhibit somewhat monochromaticity for a given direction. In Figure 4.3(b),  $\epsilon_\omega$  is plotted as a function of the angle of emission with the frequency fixed, where the solid curve corresponds to  $\omega = 0.584\omega_p$  and the dashed curve corresponds to  $\omega = 0.592\omega_p$ . Angular emission lobes which are similar to those in Figure 4.1(b) are observed. The angular emission lobes are relatively broad, which are due to the relatively flat dispersion curves shown in Figure 4.2(b) for small wavevector  $k_x$ . Therefore, thermal emission from the bilayer can be coherent. The coherent emission is because surface polaritons excited at the interface of the bilayer couple with and thus enhance the thermal emission. Similarly, the calculated  $\epsilon_\omega$  of the bilayer at  $30^\circ$  and  $60^\circ$  emission angles for  $p$ -polarization is plotted in Figure 4.4(a). The center frequency is found to be  $0.576\omega_p$  for  $30^\circ$  emission angle and  $0.570\omega_p$  for  $60^\circ$  emission angle, with a Q factor equal to 83 and 113, respectively. Angular distributions of  $\epsilon_\omega$  for  $\omega = 0.576\omega_p$  (solid curve)

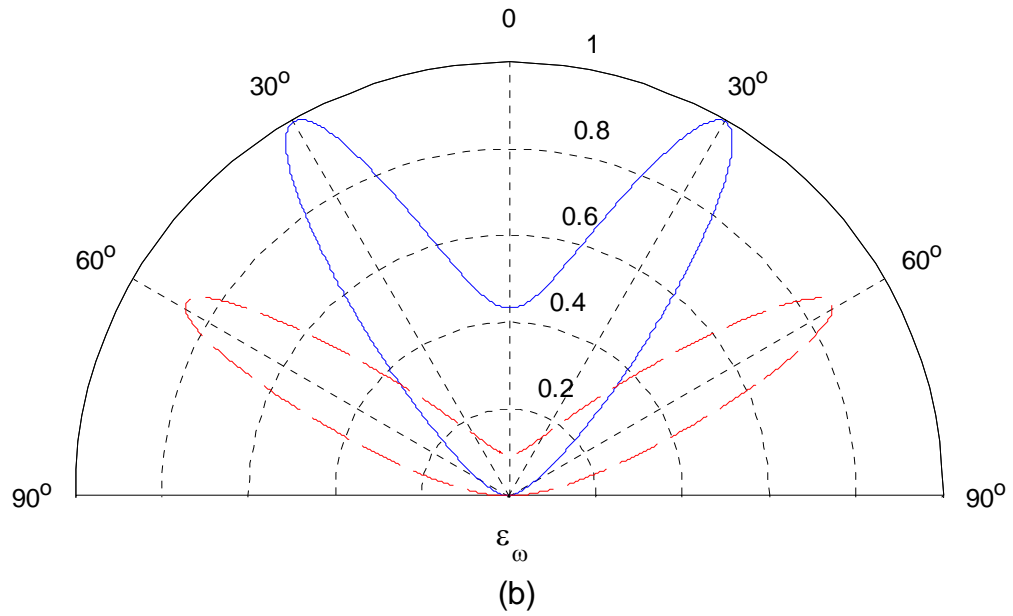
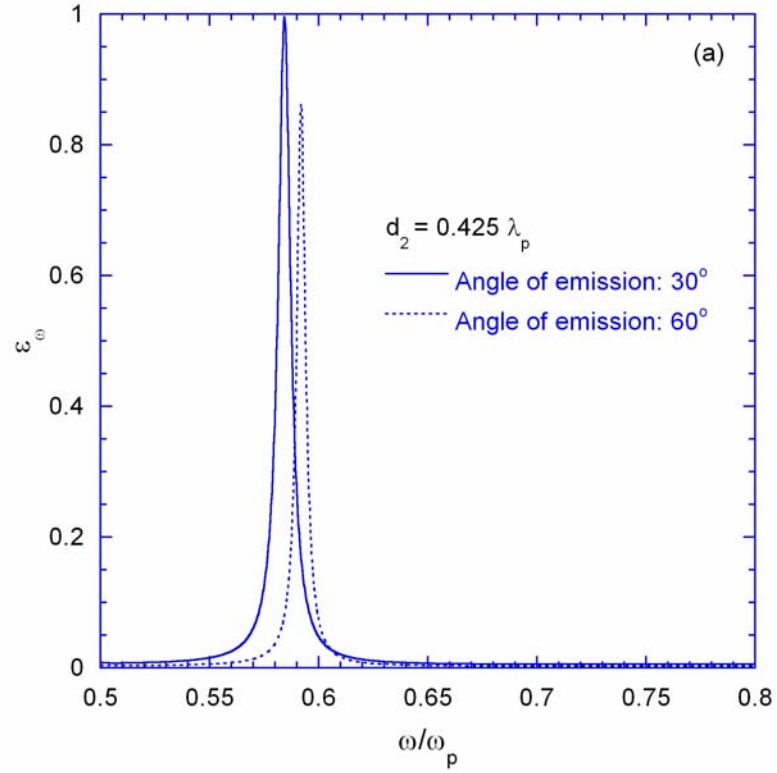


Figure 4.3 The directional spectral emissivity  $\varepsilon_\omega$  of the bilayer structure for  $s$ -polarization: (a) plotted versus  $\omega$  for  $30^\circ$  and  $60^\circ$  emission angles; (b) angular distribution for  $\omega = 0.584\omega_p$  (solid curve) and  $\omega = 0.592\omega_p$  (dashed curve).

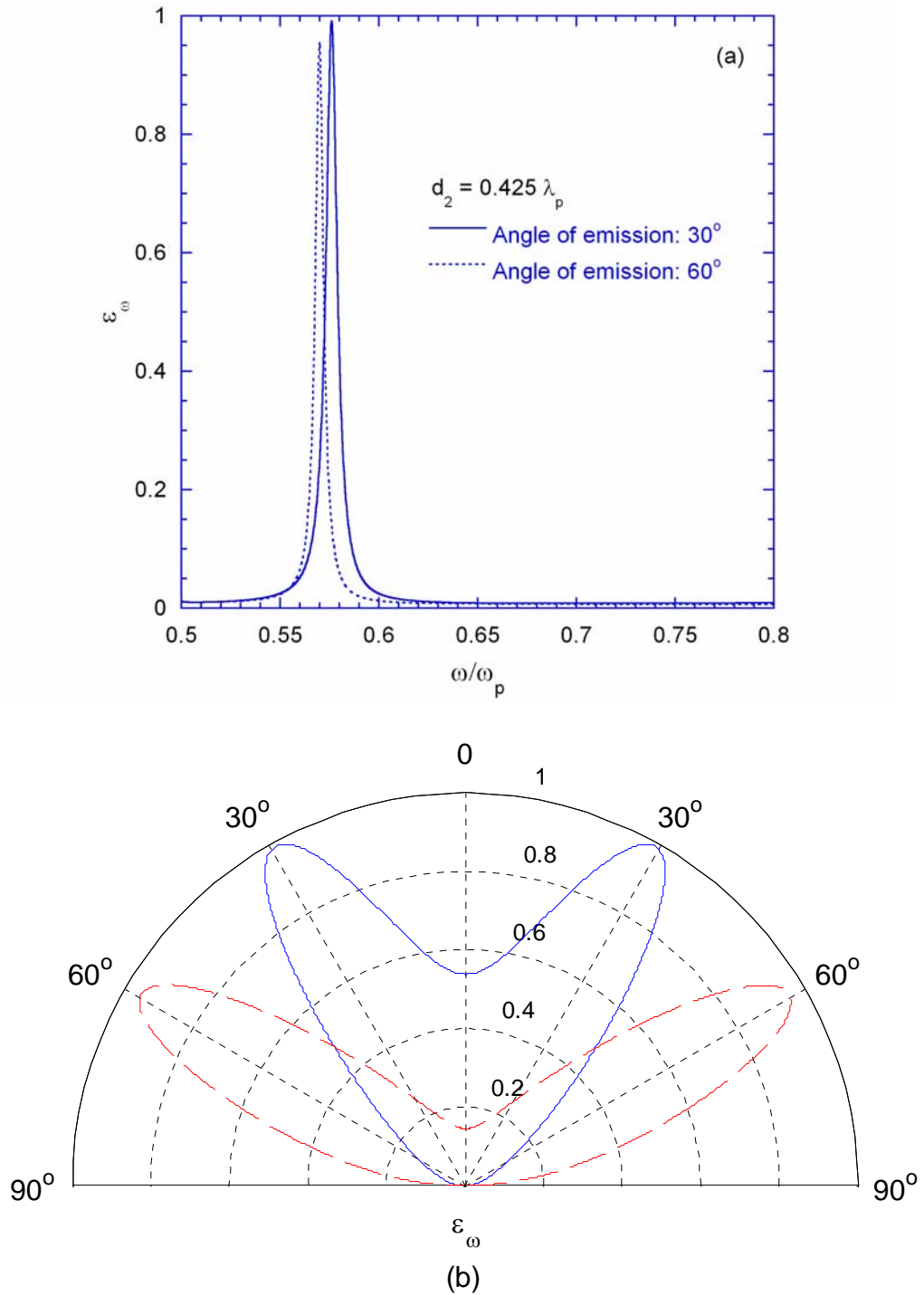


Figure 4.4 The directional spectral emissivity  $\varepsilon_\omega$  of the bilayer structure for  $p$ -polarization: (a) plotted versus  $\omega$  for  $30^\circ$  and  $60^\circ$  emission angles; (b) angular distribution for  $\omega = 0.576\omega_p$  (solid curve) and  $\omega = 0.570\omega_p$  (dashed curve).

and  $\omega = 0.570\omega_p$  (dashed curve) are shown in Figure 4.4(b). Angular emission lobes are also found. Again, the relatively wide angular emission lobes are due to the relatively flat dispersion curves in Figure 4.2(b). Narrow angular emission lobes may be obtained if the parameters in Equations (4.4) and (4.5) are chosen appropriately. Therefore, the bilayer can be used to achieve coherent thermal emission of both  $s$ - and  $p$ -polarizations but without use of gratings. It should be mentioned here that  $d_2$  has important effect on the magnitude of  $\varepsilon_\omega$  at the center frequency  $\omega_c$ . Tuning the value of  $d_2$  can obtain an optimized  $\varepsilon_\omega$  for each angle of emission.

The frequency (wavelength) and direction of coherent thermal emission from a grating depend on both the dielectric function and the periodicity of the grating. For the proposed heterogeneous structure, shown in Figure 4.2(a), the frequency and direction of coherent thermal emission are only determined by the materials since no gratings are used. Therefore, it will be difficult to tune the emission frequency and emission angle if the materials are fixed. This problem can be solved if the heterogeneous structure is built with three layers. For example, if the top layer (medium 2, medium 1 is still assumed vacuum as in Figure 4.2(a)) has  $\varepsilon_2 < 0$ ,  $\mu_2 > 0$  and thickness  $d_2$ , the mid-layer (medium 3) will have  $\varepsilon_3 > 0$ ,  $\mu_3 < 0$  and thickness  $d_3$ , and the substrate (medium 4) will be the same as medium 2 except that its thickness is assumed infinity. In this structure,  $d_3$  gives an extra parameter that can be adjusted to control the frequency and angle of emission. The reason has been stated in Chapter 3, that is, surface polaritons can be excited at both the second and third interfaces. The excited surface polaritons will interact with each other if  $d_3$  is small enough that each dispersion curve shown in Figure

4.2(a) will split into two curves, with one shifting to higher frequencies and the other to lower frequencies, and denoted by two dispersion relations. For  $p$ -polarization, the dispersion relations can be written as (Ruppin, 2001)

$$\frac{k_{2z}}{\varepsilon_2} + \frac{k_{3z}}{\varepsilon_3} \tanh(k_{3z}d_3 / 2) = 0 \quad (4.6)$$

and 
$$\frac{k_{2z}}{\varepsilon_2} + \frac{k_{3z}}{\varepsilon_3} \coth(k_{3z}d_3 / 2) = 0 \quad (4.7)$$

The dispersion relations for  $s$ -polarization are in the same form except that  $\varepsilon_2$  and  $\varepsilon_3$  are replaced with  $\mu_2$  and  $\mu_3$ . Assuming that the material properties can be expressed with Equations (4.4) and (4.5) and  $\varepsilon_3 = 4$ , the dispersion curves for  $p$ -polarization calculated from Equations (4.6) and (4.7) are shown in Figure 4.5 for  $d_3$  equal to  $0.1\lambda_p$  (solid curves) and  $0.07\lambda_p$  (dashed curves). The upper and lower branches of the curves correspond to Equations (4.6) and (4.7), respectively. Comparing with Figure 4.2(b), split of the dispersion curve by reducing the value of  $d_3$  is clearly seen. The upper branch has a much larger frequency shift than the lower branch, resulting in a steeper upper branch but a flatter lower branch. Therefore, coherent thermal emission should be found at two different narrow frequency bands for each angle of emission. The directional spectral emissivity of the three-layer heterogeneous structure is shown in Figure 4.6(a) as a function of  $\omega/\omega_p$  for a  $30^\circ$  emission angle. In this figure, the value of  $d_2$  is taken as  $0.53\lambda_p$  such that large values of  $\varepsilon_\omega$  appear around the higher surface polariton frequency, which is equal to  $0.706\omega_p$  for  $d_3 = 0.1\lambda_p$  and  $0.782\omega_p$  for  $d_3 = 0.07\lambda_p$ . It can be seen that for a given emission direction, tuning the value of  $d_3$  can control the center frequency of the narrow emission band. The corresponding Q factor is 210 for  $\omega_c = 0.706\omega_p$  and 174

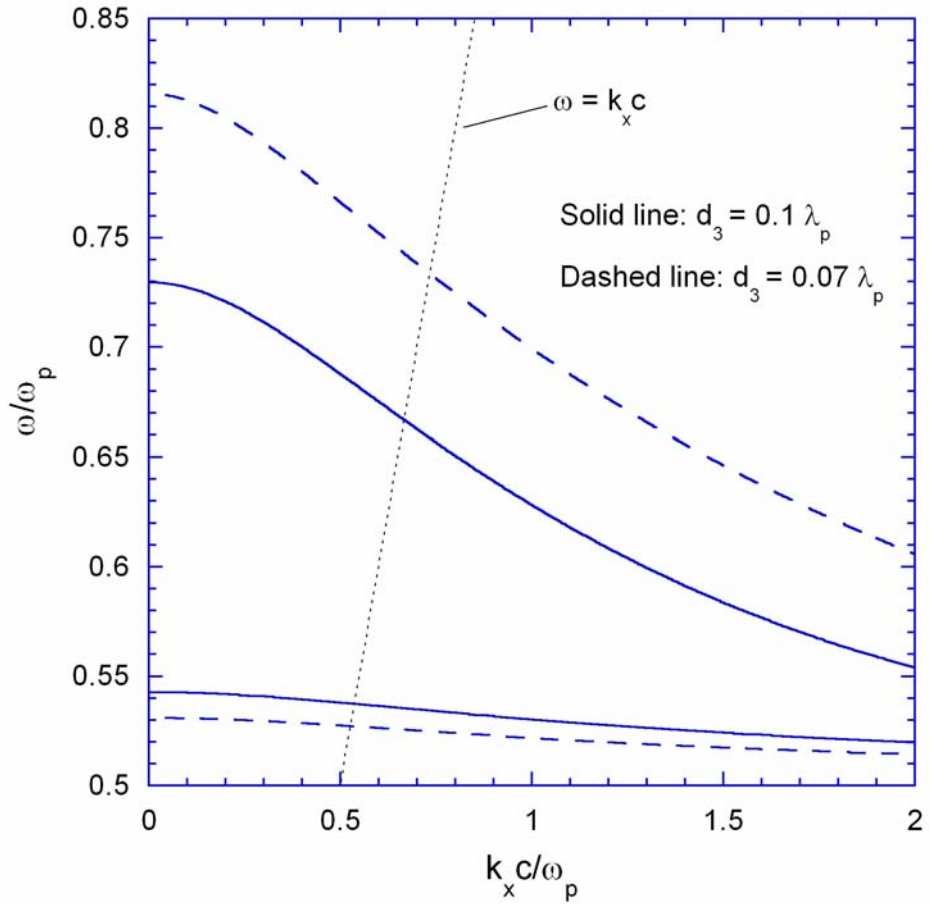


Figure 4.5 The dispersion curves of a three-layer structure where the negative  $\mu$  layer is sandwiched by two negative  $\varepsilon$  layers of the same material. In the calculation, Equations (4.4) and (4.5) with  $\varepsilon_3$  taken as 4 are used to model the electric and magnetic behaviors of media 2 and 3.

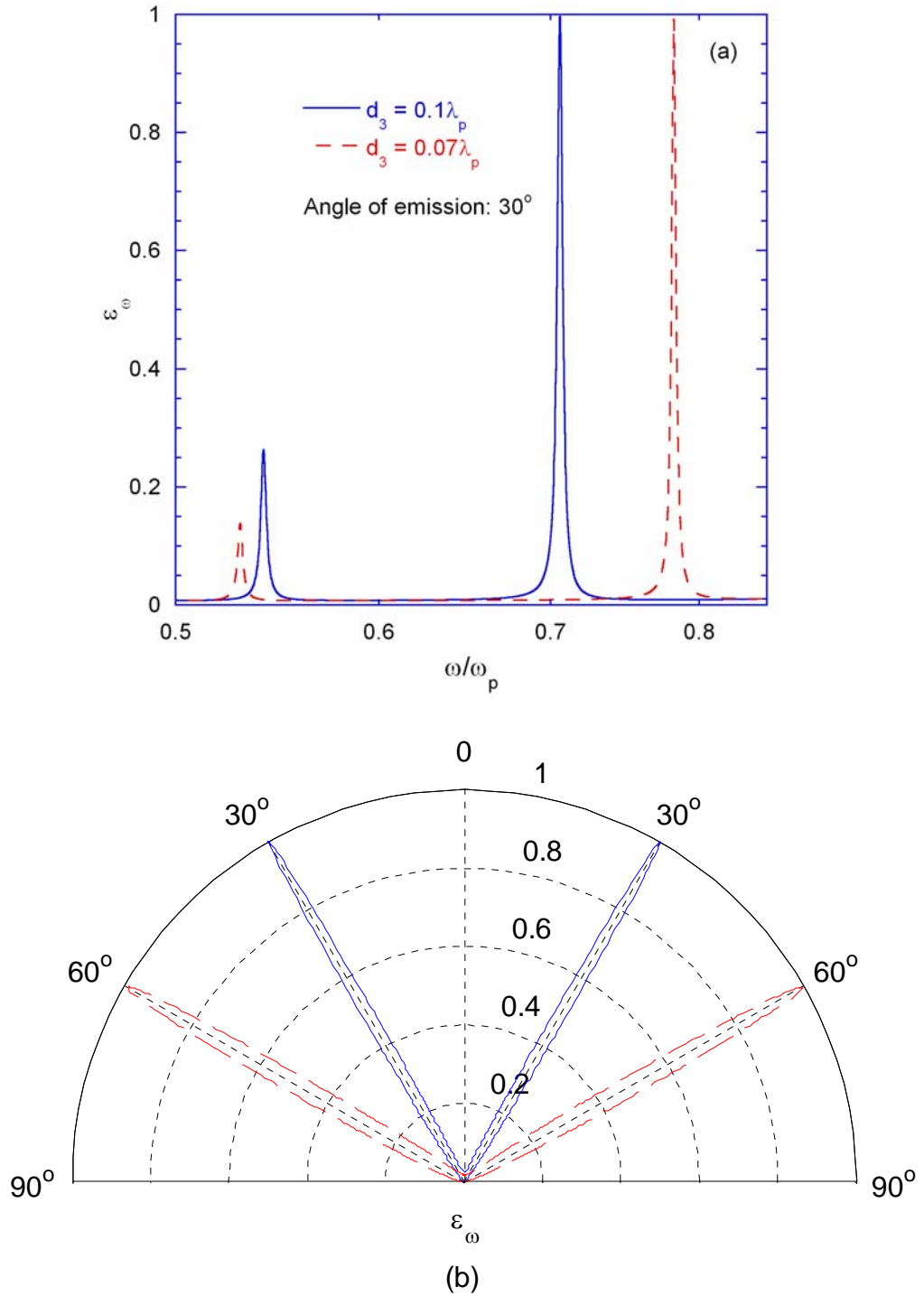


Figure 4.6 The directional spectral emissivity  $\varepsilon_\omega$  of the three-layer structure for  $p$ -polarization: (a) plotted versus  $\omega$  for a 30° emission angles; (b) angular distribution for  $\omega = 0.706\omega_p$  (solid curve) and  $\omega = 0.678\omega_p$  (dashed curve).

for  $\omega_c = 0.782\omega_p$ . Finally, because the upper branch of the dispersion curves is so steep that very narrow angular emission lobes can be obtained using the three-layer heterogeneous structure, which is shown in Figure 5.6(b). In this figure,  $d_3 = 0.1\lambda_p$ , the solid curve corresponds to  $\omega = 0.706\omega_p$  and the dashed curve corresponds to  $\omega = 0.678\omega_p$ . The dashed curve indicates the coherent thermal emission is at a  $60^\circ$  emission angle, which is not shown in Figure 4.6(a).



## CHAPTER 5

### THE BREWSTER ANGLE WITH A NEGATIVE INDEX MATERIAL

The particular phenomenon of the Brewster angle related to a lossless NIM is studied in this chapter. A Brewster angle is an incidence angle for which no energy is reflected for at least one polarization. There are a number of applications and devices that employ the unique property of Brewster's angle, including polarizers (Kaplan and Hanssen, 1999; Sihvola and Lindell, 1993) and transmission windows (Yang et al., 2003). It has been shown that the Brewster angle, which exists only for a TM wave (i.e.,  $p$ -polarized) upon reflection at the boundary between two conventional dielectric media, can occur for both TE (i.e.,  $s$ -polarized) and TM waves when one of the materials is an NIM (Leskova et al., 2001 and 2003). However, the criteria for the occurrence of a Brewster angle have not been fully investigated.

The geometry considered here is illustrated in Figure 2.2, where light is incident from a medium of refractive index  $n_1$  to another medium of refractive index  $n_2$ . In the figure, PIM refers to a conventional dielectric with a positive index of refraction. Note that when light is incident from a PIM to an NIM, as shown in Figure 2.2(b), negative refraction occurs ( $\theta_2 < 0$ ) and the refracted wavevector points opposite to the direction of the energy flux. For conventional nonmagnetic dielectrics, the Brewster angle results from the fact that an electric dipole cannot radiate along its own axis. The reflected power goes to zero when the electric dipoles induced in the material align with the direction of the reflected wave (Kong, 1990). Consequently, a Brewster angle exists only for TM waves, when the refracted wave is perpendicular to the reflected wave (i.e.,

$\theta_1 + \theta_2 = 90^\circ$ ). When this criterion is combined with Snell's law, the conventional expression for the Brewster angle is obtained:  $\theta_B = \theta_1 = \tan^{-1}(n_2/n_1)$ .

Given the dramatic change in refraction for plane waves incident on an NIM versus a PIM (Figure 2.2), it is interesting to consider whether Brewster's angle obeys the conventional criterion above. In this chapter, the existence of Brewster's angle at the interface between two semi-infinite lossless dielectric-magnetic media (also known as general dielectrics), including especially the case of NIMs is investigated. Each medium is characterized by a real  $\epsilon$  (relative permittivity) and a real  $\mu$  (relative permeability) of the same sign. Consequently, the refractive index  $n = \pm\sqrt{\epsilon\mu}$  is positive when both  $\epsilon$  and  $\mu$  are positive, or negative when both  $\epsilon$  and  $\mu$  are negative (Veselago, 1968). Following the Ewald-Oseen extinction theorem (Born and Wolf, 1999), dipole emission from the material giving rise to the reflection and refraction characteristics are shown in detail in this chapter.

### 5.1 The Brewster angle of a Lossless NIM

The starting point to calculate the reflectance is to evaluate the Fresnel coefficients between medium 1 and medium 2 (see Figure 2.2). For a TM plane wave, the reflection coefficient is the ratio of reflected to incident magnetic field. Following, for example, Pendry (2000), it can be shown that

$$r_p = \frac{H_r}{H_i} = \frac{\frac{k_{1z}}{\epsilon_1} - \frac{k_{2z}}{\epsilon_2}}{\frac{k_{1z}}{\epsilon_1} + \frac{k_{2z}}{\epsilon_2}} = \frac{\sqrt{\frac{\mu_1}{\epsilon_1}} \cos \theta_1 - \sqrt{\frac{\mu_2}{\epsilon_2}} \cos \theta_2}{\sqrt{\frac{\mu_1}{\epsilon_1}} \cos \theta_1 + \sqrt{\frac{\mu_2}{\epsilon_2}} \cos \theta_2} \quad (5.1)$$

where  $k_{1z}$  and  $k_{2z}$  are the  $z$ -components of the wave vectors of incidence and refraction, respectively,  $\theta_1$  and  $\theta_2$  are the angles of incidence and refraction and are related by Snell's law  $n_1 \sin \theta_1 = n_2 \sin \theta_2$ . Note that  $k_z = n(\omega/c) \cos \theta$ . For a TE plane wave, the ratio of reflected to incident electric field defines the reflection coefficient, that is,

$$r_s = \frac{E_r}{E_i} = \frac{\frac{k_{1z}}{\mu_1} - \frac{k_{2z}}{\mu_2}}{\frac{k_{1z}}{\mu_1} + \frac{k_{2z}}{\mu_2}} = \frac{\sqrt{\epsilon_1} \cos \theta_1 - \sqrt{\frac{\epsilon_2}{\mu_2}} \cos \theta_2}{\sqrt{\epsilon_1} \cos \theta_1 + \sqrt{\frac{\epsilon_2}{\mu_2}} \cos \theta_2} \quad (5.2)$$

If medium 2 is an NIM, both  $\theta_2$  and  $k_{2z}$  become negative as shown in Figure 2.2(b) but  $\cos \theta_2$  remains positive. Because the ratio of permittivity and permeability is positive, the reflection coefficients are real and depend only on the magnitudes of the permittivities and permeabilities of the two media. If  $|n_1/n_2| > 1$  (i.e.,  $\epsilon_1 \mu_1 > \epsilon_2 \mu_2$ ), however, total internal reflection will occur at incidence angles greater than the critical angle defined as  $\theta_c = \sin^{-1} |n_2/n_1|$  for both polarizations. At  $\theta_1 = \theta_c$ , both  $k_{2z}$  and  $\cos \theta_2$  are zero, so  $r_p = r_s = 1$ . When  $\theta_1 > \theta_c$ , both  $k_{2z}$  and  $\cos \theta_2$  become purely imaginary, resulting in complex reflection coefficients (with magnitude equal to unity). The requirement of the evanescent wave to decay towards positive  $z$  in medium 2 imposes a constraint on the selection of  $k_{2z}$  (Pendry, 2000), that is,  $k_{2z} = n_2(\omega/c) \cos \theta_2 = i\beta_2$ , where  $\beta_2 = (\omega/c) \sqrt{n_1^2 \sin^2 \theta_1 - n_2^2}$  is a real positive number no matter whether medium 2 is a PIM or an NIM. When the sign of  $n_2$  is changed from positive (PIM) to negative (NIM),  $k_{2z}$  remains the same but  $\cos \theta_2$  changes sign. As a consequence, the reflection coefficient will change to its complex conjugate

for any given polarization (Lakhtakia, 2003). Nevertheless, Equations (5.1) and (5.2) are general expressions when the signs of  $k_{2z}$  and  $\cos\theta_2$  are properly selected.

The reflectance, however, is given by  $R = |r|^2$  for either polarization. Despite the fact that  $\varepsilon$ 's and  $\mu$ 's may be negative, their signs do not have any impact on the reflectance. Hence, in the lossless case,

$$\begin{aligned} R(\theta_1, \varepsilon_1, \mu_1, \varepsilon_2, \mu_2) &= R(\theta_1, \varepsilon_1, \mu_1, -\varepsilon_2, -\mu_2) \\ &= R(\theta_1, -\varepsilon_1, -\mu_1, \varepsilon_2, \mu_2) \\ &= R(\theta_1, -\varepsilon_1, -\mu_1, -\varepsilon_2, -\mu_2) \end{aligned} \quad (5.3)$$

These equalities greatly simplify the analysis of parameter regimes for which a Brewster angle may exist. The Brewster angle corresponds to a reflection coefficient of zero. Because the Fresnel coefficient is a continuous function of the incidence angle, the key for the occurrence of a Brewster angle is whether the sign of the reflection coefficient changes between normal incidence and an incidence angle equal to either the critical angle or the grazing angle ( $90^\circ$ ).

Consider the case  $\varepsilon_1\mu_1 < \varepsilon_2\mu_2$ , when there is no total internal reflection. Equations (5.1) and (5.2) show that  $r_p = -r_s$  at normal incidence and  $r_p = r_s = -1$  at  $\theta_1 = 90^\circ$ . If  $\mu_1/\varepsilon_1 \neq \mu_2/\varepsilon_2$ , either  $r_p$  or  $r_s$  will be positive at  $\theta_1 = 0$ , resulting in a Brewster angle between  $0$  and  $90^\circ$  for either  $p$ - or  $s$ -polarization. A Brewster angle exists for a TM wave if  $\mu_1/\varepsilon_1 > \mu_2/\varepsilon_2$  and for a TE wave if  $\mu_1/\varepsilon_1 < \mu_2/\varepsilon_2$ . In the extreme case when  $\mu_1/\varepsilon_1 = \mu_2/\varepsilon_2$ , we have  $r_s = r_p = 0$  at normal incidence. That is, a Brewster angle exists for both polarizations at normal incidence, and the reflectance (the same for both polarizations) will increase monotonically from  $0$  to  $1$  as  $\theta_1$  is increased from  $0$  to  $90^\circ$ .

The above discussion can be extended to the case  $\varepsilon_1\mu_1 > \varepsilon_2\mu_2$ , for which a critical angle exists. Recall that  $\cos\theta_2 = 0$  and  $r_s = r_p = 1$  at the critical angle. A Brewster angle exists for a TM wave if  $\mu_1/\varepsilon_1 < \mu_2/\varepsilon_2$  and for a TE wave if  $\mu_1/\varepsilon_1 > \mu_2/\varepsilon_2$ . When  $\mu_1/\varepsilon_1 = \mu_2/\varepsilon_2$ , the reflectance is the same for both polarizations and increases from 0 to 1 when  $\theta_1$  is increased from 0 to  $\theta_c$ .

The various possibilities can be concisely summarized in a map of different material parameter regimes, as shown in Figure 5.1. A different regime map containing similar information was provided in the work of Henderson et al. (1991), who considered reflection/transmission between general dielectrics, but without discussing negative index materials. The regime map of Figure 5.1 is established in terms of two new parameters  $X = \varepsilon_1\mu_1/\varepsilon_2\mu_2$  and  $Y = \varepsilon_2\mu_1/\varepsilon_1\mu_2$  where  $\varepsilon_l$  and  $\mu_l$  are the permittivity and permeability of medium  $l$  ( $l = 1,2$ ). Based on the discussion given above, a Brewster angle can be found for a TM wave in the shaded regions (I) and (IV). Similarly, a Brewster angle exists for a TE wave in regions (II) and (III). Total internal reflection will occur in regions (II) and (IV), where  $X > 1$ . The line  $X = 1$  corresponds to the case of  $|\theta_1| = |\theta_2|$ , when the reflectance is independent of the angle of incidence. The line  $Y = 1$  corresponds to the cases when the reflectance is zero at normal incidence and independent of polarization. The normal reflectance increases as  $Y$  is either reduced or increased, and it becomes unity as  $Y$  approaches 0 or infinity. At the crossing point  $X = Y = 1$ , the reflectance is zero for both polarizations, regardless of the angle of incidence. The physical significance of the curves for  $X = Y$  and  $XY = 1$  will be discussed below.

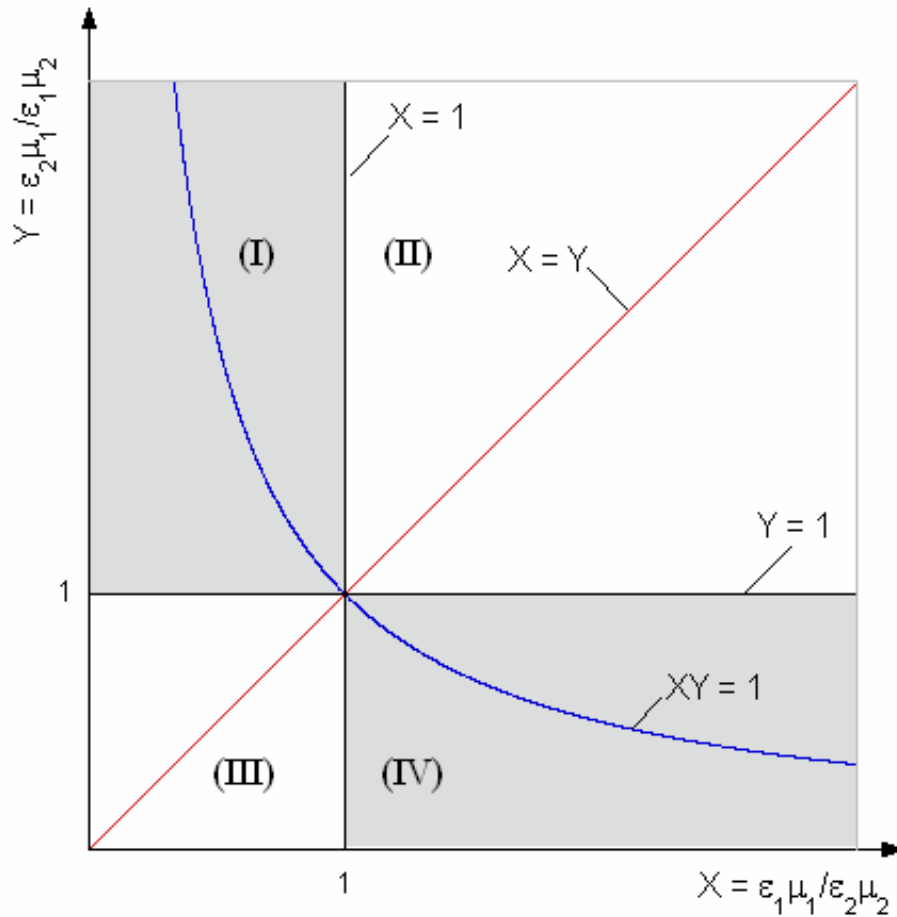


Figure 5.1 The regime map based on parameters  $X$  and  $Y$ , which depend on the permittivities and permeabilities of the two media (see axis labels). The Brewster angle exists for TM waves in the shaded regions and for TE waves in the unshaded regions. The curves  $X = Y$  and  $XY = 1$  correspond to  $\theta_1 + \theta_2 = 90^\circ$  for PIM/PIM or NIM/NIM interfaces, this is the condition that reflected and refracted beams lie at right angles. However, for a PIM/NIM or NIM/PIM interface the refracted and *incident* beams are perpendicular.

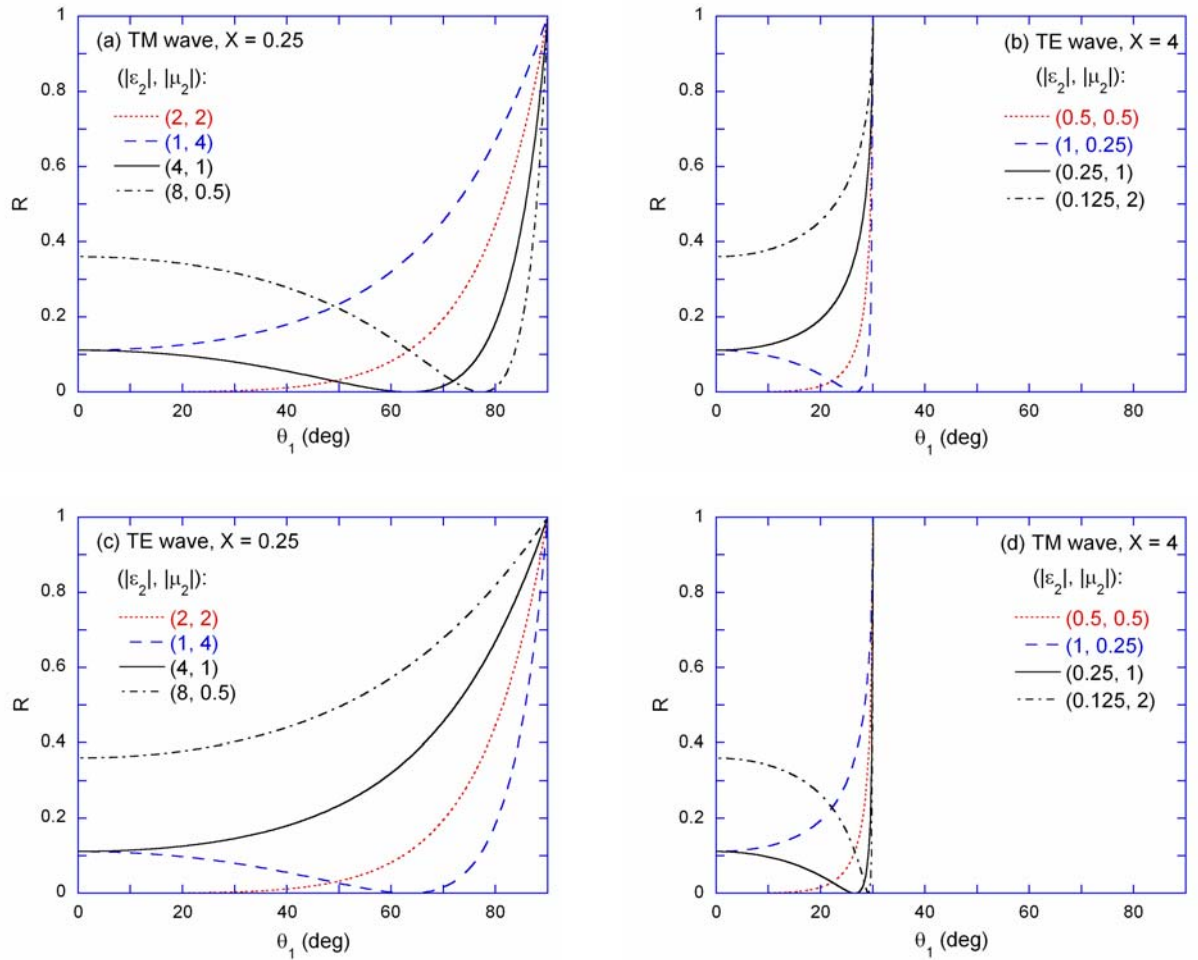


Figure 5.2 The reflectance  $R$  at the interface of vacuum and an NIM, with different values of the permittivity and permeability, as a function of the incidence angle. The Brewster angle can occur for a TE wave, a TM wave, or both under conditions discussed in the text.

Figure 5.2 shows the calculated reflectance for light incident from vacuum ( $\epsilon_1 = \mu_1 = 1$ ) to an NIM. The figures on the left correspond to  $X = 0.25$ , while the figures on the right correspond to  $X = 4$ , when total internal reflection will occur. Each of the four panels provides a brief case study of the reflectance for parameters in the four different regions. From Figure 5.2(a), one can see that the Brewster angle for a TM wave exists when  $|\epsilon_2| > |\mu_2|$ , i.e. in Region I of Figure 5.1. When  $\epsilon_2 = \mu_2$  ( $Y = 1$ ), the reflectance is zero at normal incidence and it increases as the ratio  $\epsilon_2 / \mu_2$  deviates from 1. Similar trends can be seen in Figures 5.2(b)-5.2(d). For instance, as shown in Figure 5.2 (b), the Brewster angle for a TE wave exists in Region II where total internal reflection also occurs. It can be seen that the reflectance for a TM wave and for a TE wave will interchange when the values of  $\epsilon_2$  and  $\mu_2$  are switched. Not shown in Figure 5.2 is the case  $X = 1$ , for which  $|\theta_1| = |\theta_2|$  and the reflectance becomes  $R = \left( |\epsilon_1| - |\epsilon_2| \right)^2 / \left( |\epsilon_1| + |\epsilon_2| \right)^2$ , for any  $\theta_1$ , independent of polarization.

General expressions for the Brewster angle can be obtained by setting  $r = 0$  for each polarization; see Equations (5.1) and (5.2). The solutions give:

$$\theta_B = \sin^{-1} \left( \sqrt{Y - 1/Y - X} \right), \text{ for a TM wave} \quad (5.4a)$$

and 
$$\theta_B = \sin^{-1} \left( \sqrt{1 - Y/1 - XY} \right), \text{ for a TE wave} \quad (5.4b)$$

These equations uniquely determine the value of the Brewster angle for different material parameters except when  $X = Y = 1$ , for which the reflectance is zero at all angles of incidence. Figure 5.3 shows a contour plot of the Brewster angle according to Equations (5.4). The curves represent constant Brewster angles in the  $X$ - $Y$  plane. For both



polarizations, the contours approach the  $Y = 1$  line when  $\theta_B$  approaches 0, and they approach the  $X = 1$  line when  $\theta_B$  approaches  $90^\circ$ .

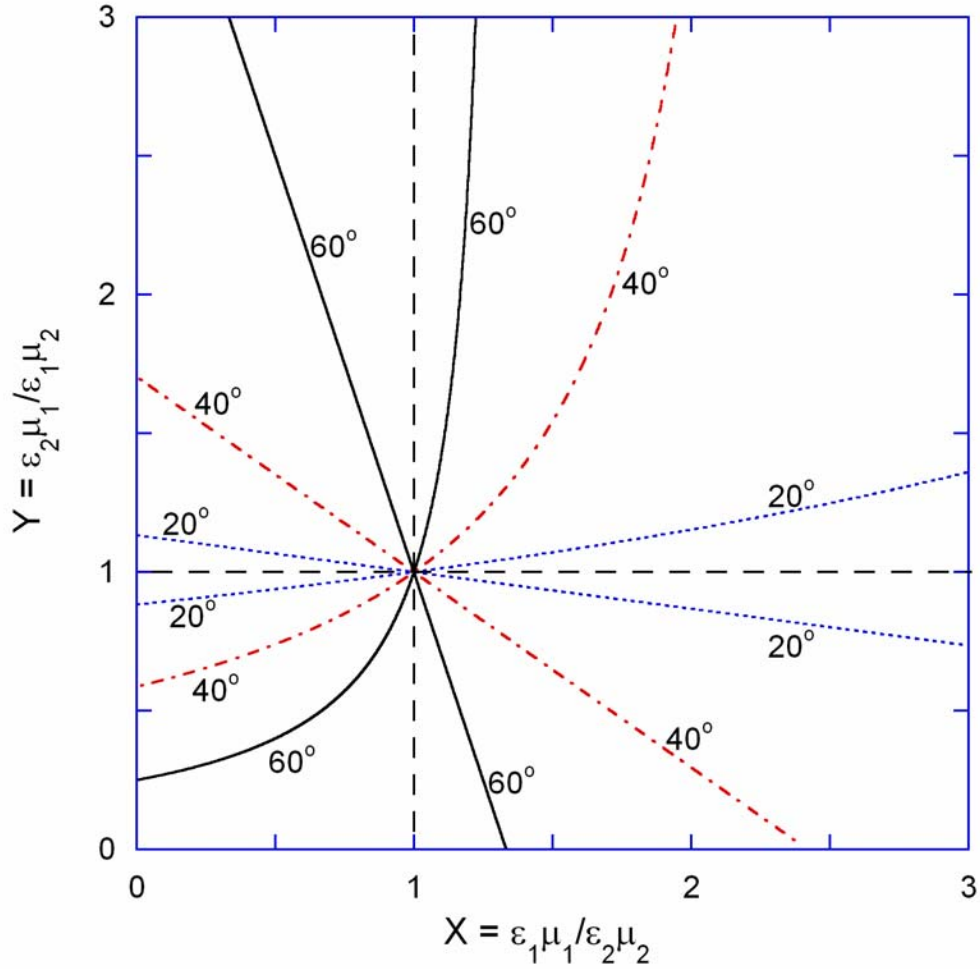


Figure 5.3 Contour plot with curves of constant Brewster angle in the  $X$ - $Y$  plane.

From the result above, it is clear that at  $\theta_1 = \theta_B$ , the relation  $\theta_1 + \theta_2 = 90^\circ$  does not necessarily hold for dielectric-magnetic media. The relation is satisfied only when  $\epsilon_1 = \epsilon_2$  ( $X = Y$ ) for a TE wave and  $\mu_1 = \mu_2$  ( $XY = 1$ ) for a TM wave, respectively.

Curves with  $X = Y$  and  $XY = 1$  are shown in Figure 5.1 to distinguish these special cases. It should be noted that if  $\varepsilon_1 = -\varepsilon_2$  for a TE wave or  $\mu_1 = -\mu_2$  for a TM wave, then  $\theta_1 - \theta_2 = 90^\circ$  at the Brewster angle. In this case, the refracted wave is perpendicular to the *incident* wave.

## 5.2 Physical Explanations Based on the Ewald-Oseen Extinction Theorem

The physical mechanisms of reflection and refraction can be explained based on the Ewald-Oseen extinction theorem (Born and Wolf, 1999). For simplicity, consider the reflection and refraction of a plane wave incident from vacuum ( $\varepsilon_1 = \mu_1 = 1$ ) into a dielectric-magnetic medium. From the microscopic point of view, electromagnetic wave reflection and refraction at the interface is the result of induced re-emission from electric and magnetic dipoles in the medium. The dipoles radiate in vacuum and the transmitted wave is the superposition of the incident wave and all radiated waves from the induced dipoles, while the reflected wave is solely due to the dipole emission. It is well known that for a nonmagnetic dielectric and a TM wave incident at the Brewster angle, the axes of the induced electric dipoles are aligned with the wavevector of reflection, resulting in zero reflectance. In the case that the medium is magnetic, radiation from induced magnetic dipoles inside the dielectric also must be included. The radiated fields from the induced electric and magnetic dipoles can be calculated, respectively, as (Born and Wolf, 1999)

$$\mathbf{E}_e = \nabla(\nabla \cdot \Pi_e) - \varepsilon_0 \mu_0 \frac{\partial^2 \Pi_e}{\partial t^2} \quad (5.5)$$

$$\mathbf{E}_m = -\mu_0 \nabla \times \frac{\partial \Pi_m}{\partial t} \quad (5.6)$$

where  $\Pi_e$  and  $\Pi_m$  are the Hertz vectors, which are expressed in terms of the electric polarization  $\mathbf{P}$  and magnetization  $\mathbf{M}$  as

$$\Pi_e = \int_V \frac{\mathbf{P}}{\epsilon_0} G(\mathbf{r} - \mathbf{r}') d\mathbf{r}' = \int_V \frac{\mathbf{P} e^{ik|\mathbf{r}-\mathbf{r}'|}}{4\pi\epsilon_0|\mathbf{r}-\mathbf{r}'|} d\mathbf{r}' \quad (5.7)$$

$$\Pi_m = \int_V \mathbf{M} G(\mathbf{r} - \mathbf{r}') d\mathbf{r}' = \int_V \frac{\mathbf{M} e^{ik|\mathbf{r}-\mathbf{r}'|}}{4\pi|\mathbf{r}-\mathbf{r}'|} d\mathbf{r}' \quad (5.8)$$

where  $k = \omega/c$ . The integration is for the whole volume occupied by the dielectric. Following the Ewald-Oseen extinction theorem (Born and Wolf, 1999), if the incident field from vacuum is  $\mathbf{E}_i$  and the transmitted field  $\mathbf{E}_t$ , the total radiated field for  $\mathbf{r}$  inside the dielectric is given by

$$\mathbf{E}_{rad} = \mathbf{E}_e + \mathbf{E}_m = \mathbf{E}_t - \mathbf{E}_i \quad (5.9)$$

$\mathbf{P}$  and  $\mathbf{M}$  in Equations (5.7) and (5.8) can be related to the electric and magnetic fields in the dielectric as

$$\mathbf{P} = \epsilon_0 \chi \mathbf{E}_t \quad \text{and} \quad \mathbf{M} = \chi_m \mathbf{H}_t \quad (5.10)$$

where  $\chi$  is the dielectric susceptibility and is related to  $\epsilon$  as  $\epsilon = 1 + \chi$ ,  $\chi_m$  is the magnetic susceptibility and is related to  $\mu$  as  $\mu = 1 + \chi_m$ ,  $\mathbf{H}_t$  can be calculated from  $\mathbf{E}_t$  using Maxwell's first curl equation.

In the subsequent derivation, the same coordinates as in Figure 2.2 are used and the dielectric is assumed to occupy the half space of  $z \geq 0$ . Therefore, the evaluation of Equations (5.7) and (5.8) for  $z \geq 0$  should give the transmitted field and for  $z < 0$  should give the reflected field. For an incident plane wave  $\mathbf{E}_{i0} e^{ik_1 \mathbf{r}}$  (omitting the common factor

$e^{-i\omega t}$  here and subsequently), the integration of Equation (5.7) can be evaluated following Orfanidis (2004) as

$$\Pi_e = \begin{cases} \chi \mathbf{E}_{t0} \left[ -\frac{e^{i\mathbf{k}_1 \mathbf{r}}}{2k_{1z}(k_{2z} - k_{1z})} + \frac{e^{i\mathbf{k}_2 \mathbf{r}}}{(k_2^2 - k_1^2)} \right], & \text{for } z \geq 0 \\ -\chi \mathbf{E}_{t0} \left[ \frac{e^{i\mathbf{k}_r \mathbf{r}}}{2k_{1z}(k_{2z} + k_{1z})} \right] & , \text{for } z < 0 \end{cases} \quad (5.11)$$

where  $\mathbf{k}_1$ ,  $\mathbf{k}_2$ , and  $\mathbf{k}_r$  are the wave vectors of the incident, transmitted, and reflected fields, respectively,  $k_{lz}$  is the  $z$ -component of  $\mathbf{k}_l$  ( $l = 1, 2$ ), and  $\mathbf{E}_{t0}$  denotes the amplitude of the transmitted field. The evaluation of Equation (5.8) can be done similarly. Inside a general dielectric ( $z \geq 0$ ) with relative permittivity  $\epsilon_2$  and relative permeability  $\mu_2$ , Equation (5.9) then becomes:

$$\begin{aligned} & \chi \frac{\mathbf{k}_1 \times (\mathbf{k}_1 \times \mathbf{E}_{t0}) e^{i\mathbf{k}_1 \mathbf{r}}}{2k_{1z}(k_{2z} - k_{1z})} + \chi \mathbf{E}_{t0} \frac{k_1^2 e^{i\mathbf{k}_2 \mathbf{r}}}{(k_2^2 - k_1^2)} + \chi_m \mathbf{E}_{t0} \frac{k_2^2 e^{i\mathbf{k}_2 \mathbf{r}}}{(k_2^2 - k_1^2) \mu_2} \\ & + \chi_m \frac{\mathbf{k}_2 (\mathbf{k}_1 \cdot \mathbf{E}_{t0}) e^{i\mathbf{k}_1 \mathbf{r}} - (\mathbf{k}_1 \cdot \mathbf{k}_2) \mathbf{E}_{t0} e^{i\mathbf{k}_1 \mathbf{r}}}{2k_{1z}(k_{2z} - k_{1z}) \mu_2} = \mathbf{E}_{t0} e^{i\mathbf{k}_2 \mathbf{r}} - \mathbf{E}_{i0} e^{i\mathbf{k}_1 \mathbf{r}}, \text{ for } z \geq 0 \end{aligned} \quad (5.12)$$

Collecting terms of identical phase leads to

$$(1 + \chi)(1 + \chi_m)k_1^2 = \epsilon_2 \mu_2 k_2^2 = k_2^2 \quad (5.13)$$

and

$$\chi \frac{\mathbf{k}_1 \times (\mathbf{k}_1 \times \mathbf{E}_{t0})}{2k_{1z}(k_{2z} - k_{1z})} + \chi_m \frac{\mathbf{k}_2 (\mathbf{k}_1 \cdot \mathbf{E}_{t0}) - (\mathbf{k}_1 \cdot \mathbf{k}_2) \mathbf{E}_{t0}}{2k_{1z}(k_{2z} - k_{1z}) \mu_2} = -\mathbf{E}_{i0} \quad (5.14)$$

The reflected field is expressed as

$$\mathbf{E}_r = \mathbf{E}_{r,e} + \mathbf{E}_{r,m} = (\mathbf{E}_{r0,e} + \mathbf{E}_{r0,m}) e^{i(\mathbf{k}_r \cdot \mathbf{r} - \omega t)}, \text{ for } z < 0 \quad (5.15)$$

where  $\mathbf{E}_{r,e}$  is the contribution from electric dipole radiation and  $\mathbf{E}_{r,m}$  the contribution from magnetic dipole radiation,  $\mathbf{E}_{r0,e}$  and  $\mathbf{E}_{r0,m}$  denote the amplitudes of  $\mathbf{E}_{r,e}$  and  $\mathbf{E}_{r,m}$ , respectively. Using Equation (5.11),  $\mathbf{E}_{r0,e}$  and  $\mathbf{E}_{r0,m}$  can be written as

$$\mathbf{E}_{r0,e} = \chi \frac{\mathbf{k}_r \times (\mathbf{k}_r \times \mathbf{E}_{t0})}{2k_{1z}(k_{2z} + k_{1z})} \quad (5.16)$$

and

$$\mathbf{E}_{r0,m} = \chi_m \frac{\mathbf{k}_2 (\mathbf{k}_r \cdot \mathbf{E}_{t0}) - (\mathbf{k}_2 \cdot \mathbf{k}_r) \mathbf{E}_{t0}}{2k_{1z}(k_{2z} + k_{1z})\mu_2} \quad (5.17)$$

In the special case of  $\varepsilon_2 = \mu_2$  (corresponding to  $Y = 1$  in Figure 5.1), one has  $\chi = \chi_m$ ; it can be shown from Equations (5.16) and (5.17) that  $\mathbf{E}_{r0,e} = -\mathbf{E}_{r0,m}$  for normal incidence, resulting in zero reflectance, as expected from the discussion of the regime map. In the case that medium 2 is an NIM,  $\varepsilon_2$ ,  $\mu_2$ ,  $\chi$ , and  $\chi_m$  are all negative. For a TM wave incident from medium 1 to medium 2, the condition of zero reflectance leads to

$$(\varepsilon_2 - 1)\mu_2(k_{1z}k_{2z} - k_x^2) = (\mu_2 - 1)(k_{2z}^2 + k_x^2) \quad (5.18)$$

where  $k_x$  is the  $x$ -component of the wave vector which is the same in both media. In deriving Equation (5.18) the relation  $\mathbf{k}_2 \cdot \mathbf{E}_{t0} = 0$  has been used. Combining Equation (5.18) with  $k_x^2 + k_{1z}^2 = k_1^2$  and  $k_x^2 + k_{2z}^2 = \varepsilon_2\mu_2k_1^2$  gives

$$\mathbf{k}_1 \cdot \mathbf{k}_2 = k_x^2 + k_{1z}k_{2z} = \frac{\varepsilon_2(\mu_2 + 1)k_1^2}{(\varepsilon_2 + 1)} \quad (5.19)$$

and

$$k_{2z} = \varepsilon_2 k_{1z} \quad (5.20)$$

It can be seen from Equation (5.19) that  $\mathbf{k}_1$  will be perpendicular to  $\mathbf{k}_2$  if  $\mu_2 = -1$  (unless  $\varepsilon_2$  is also  $-1$ , in which case the Brewster angle is not uniquely determined). The condition  $\mu_2 = -1$  corresponds to the curve  $XY = 1$  in the regime map. Equation (5.20)

is equivalent to Equation (5.4a). Note that the above two equations are derived under the assumptions of zero reflectance and a TM wave incident on an NIM.

Now look at the amplitudes of  $E_{r0,e}$  and  $E_{r0,m}$  at different incidence angles. Using Equations (5.16) and (5.17), the field amplitudes emitted from induced dipoles inside a general dielectric with positive permittivity and permeability are calculated and shown in Figure 5.4 as a function of the incidence angle  $\theta_1$ . Here a TM wave is assumed and  $\epsilon_2 = 4$  and  $\mu_2 = 1$  are taken in Figure 5.4(a) while  $\epsilon_2 = 8$  and  $\mu_2 = 0.5$  are taken in Figure 5.4(b), which results in the refractive indices  $n_2 = 2$  for both cases and total internal reflection will not happen. In Figure 5.4(a), only the induced electric dipoles contribute to the reflected wave because the material is nonmagnetic. A Brewster angle arises from the induced electric dipoles being aligned along the direction of the reflected wave and is calculated by the conventional formula  $\theta_B = \tan^{-1}(n_2/n_1)$ . In Figure 5.4(b), however, both induced electric and magnetic dipoles make contribution to the reflected wave. It can be seen that the contribution from the induced electric dipoles  $E_{r0,e}$  is zero at  $\theta_1 = \tan^{-1}(n_2/n_1)$  while the contribution from the induced magnetic dipoles  $E_{r0,m}$  is not zero. Furthermore,  $E_{r0,e}$  and  $E_{r0,m}$  are in phase if  $\theta_1 < \tan^{-1}(n_2/n_1)$ , but are out of phase if  $\theta_1 > \tan^{-1}(n_2/n_1)$ . As a consequence, a Brewster angle  $\theta_B$  appears when  $E_{r0,e}$  and  $E_{r0,m}$  cancel out each other.

The situation is different for an NIM, because induced magnetic dipoles always contribute to the reflected wave. For the purpose of comparison, the  $\epsilon$  and  $\mu$  of an NIM are chosen as the negative values of those used in Figure 5.4 and the amplitudes  $E_{r0,e}$ ,

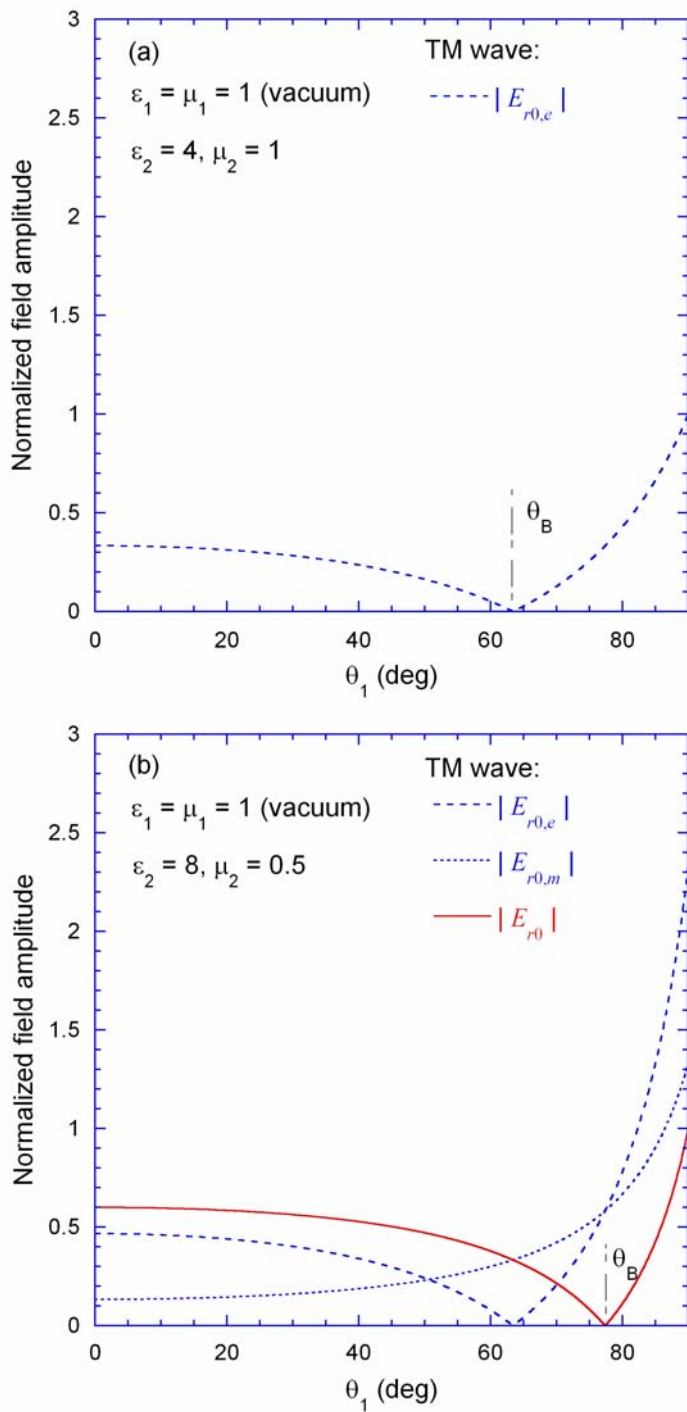


Figure 5.4 The emitted electric field amplitudes vary with incidence angle  $\theta_1$  for a TM wave incident from vacuum ( $\epsilon_1 = \mu_1 = 1$ ) into a dielectric: (a)  $\epsilon_2 = 4$  and  $\mu_2 = 1$ , no induced magnetic dipoles; (b)  $\epsilon_2 = 8$  and  $\mu_2 = 0.5$ . Note that the field amplitudes have been normalized by the incident electric field amplitude.

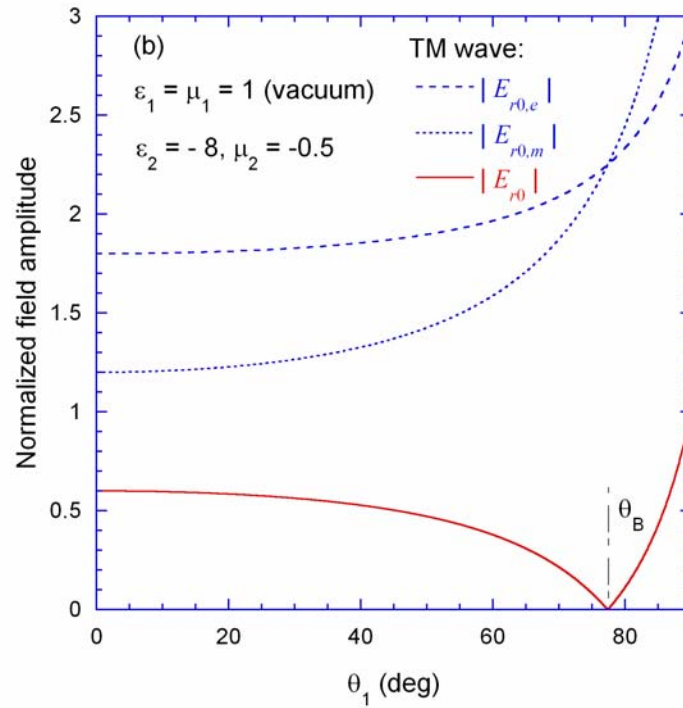
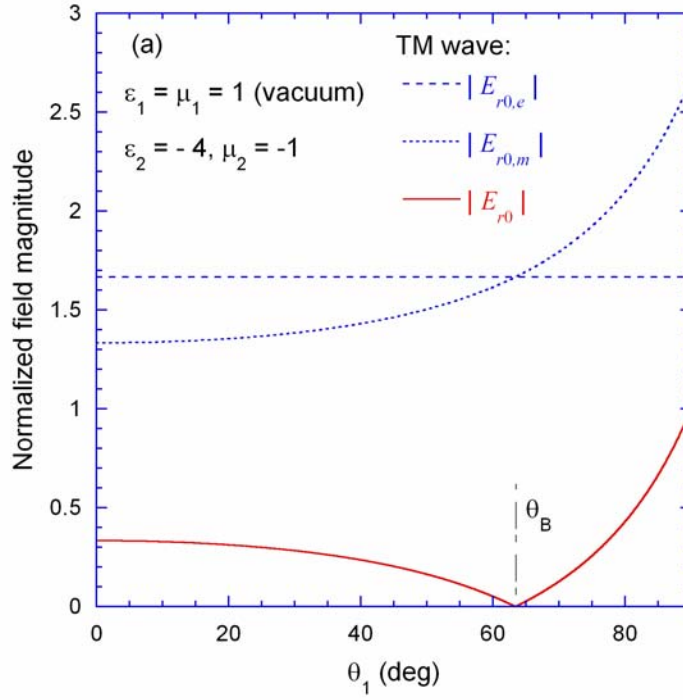


Figure 5.5 The emitted electric field amplitudes vary with incidence angle  $\theta_1$  for a TM wave incident from vacuum ( $\epsilon_1 = \mu_1 = 1$ ) into a lossless NIM: (a)  $\epsilon_2 = -4$  and  $\mu_2 = -1$ ; (b)  $\epsilon_2 = -8$  and  $\mu_2 = -0.5$ .



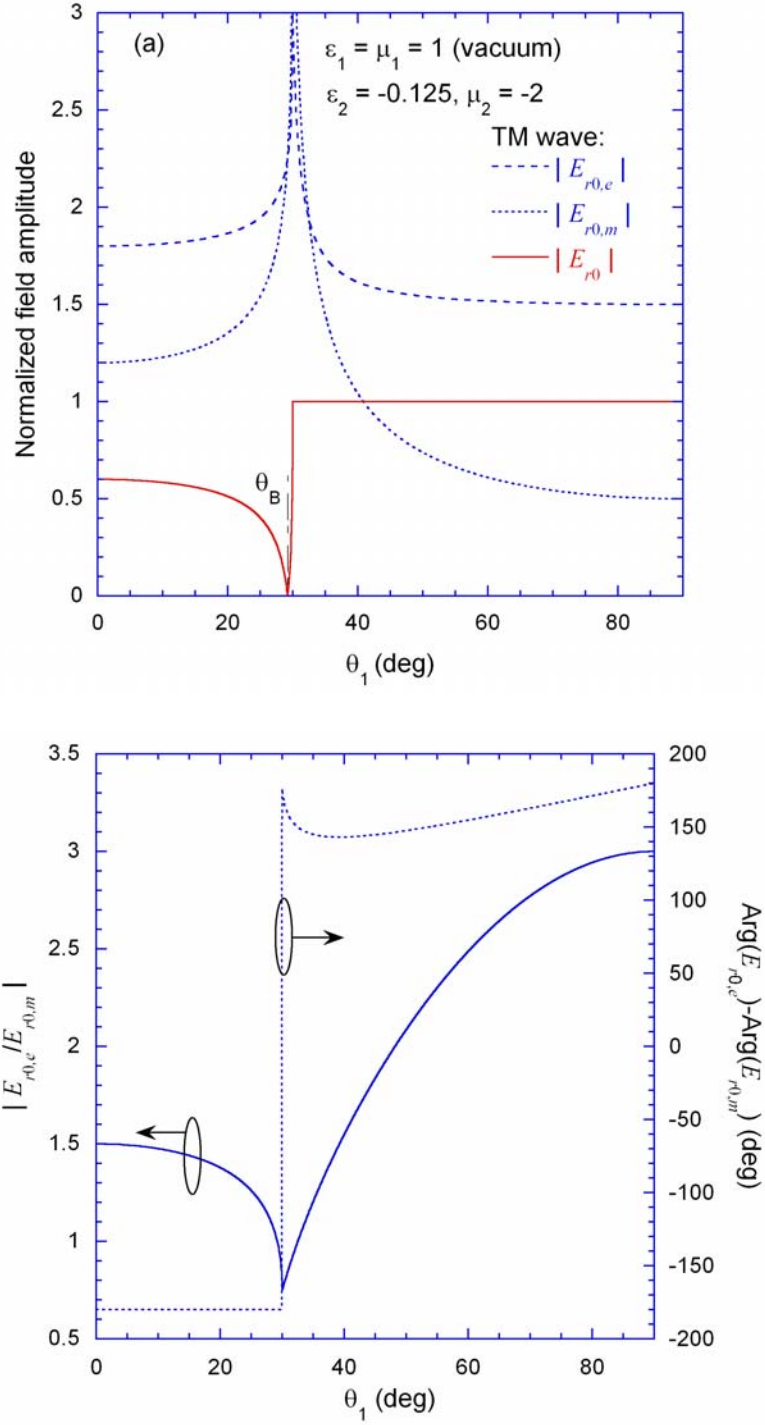


Figure 5.6 The emitted electric field amplitudes vary with incidence angle  $\theta_1$  for a TM wave incident from vacuum ( $\epsilon_1 = \mu_1 = 1$ ) into a lossless NIM with  $\epsilon_2 = -0.125$  and  $\mu_2 = -2$ : (a) normalized emitted field amplitudes; (b) emitted field amplitude ratio  $|E_{r0,e}/E_{r0,m}|$  and phase difference.

$E_{r0,m}$  and the reflected wave  $E_{r0}$  are calculated. The results are plotted in Figure 5.5(a) for  $\epsilon_2 = -4$  and  $\mu_2 = -1$ , and in Figure 5.5(b) for  $\epsilon_2 = -8$  and  $\mu_2 = -0.5$ . Both plots show that  $E_{r0,e}$  and  $E_{r0,m}$  never reach zero and superpose out-of-phase at any angle of incidence, resulting in a Brewster angle when the magnitudes are equal. The value of the Brewster angle, however, is the same in Figure 5.4 and Figure 5.5, in accordance with Equation (4a).

A situation that corresponds to total internal reflection is also considered, which is shown in Figure 5.6 with  $\epsilon_2 = -0.125$  and  $\mu_2 = -2$  ( $X = 4$  and  $Y = 0.0625$  in the regime map). In this case, when  $\theta_1 > \theta_c$ , the phase difference between  $E_{r0,e}$  and  $E_{r0,m}$  is not simply 0 (in phase) or  $\pm\pi$  (out of phase), but varies continuously with  $\theta_1$ . The superposition of  $E_{r0,e}$  and  $E_{r0,m}$ , when taking this factor into account, results in total internal reflection for  $\theta_1 > \theta_c$ .

The discussion for a TE wave can be done in the same way. Therefore, we have shown, from a microscopic point of view, zero reflectance for a plane wave incident at the Brewster angle is due to the superposition of the radiated fields of induced electric and magnetic dipoles inside a lossless dielectric-magnetic material including an NIM. The cancellation of the emitted fields can only be along a direction that deviates from the axes of either the electric dipoles or the magnetic dipoles and the relation  $\theta_1 + \theta_2 = 90^\circ$  ( $\theta_1 - \theta_2 = 90^\circ$  for a PIM/NIM interface) is satisfied only under the restricted conditions  $\epsilon_1 = \pm\epsilon_2$  (s-polarization) or  $\mu_1 = \pm\mu_2$  (p-polarization).

## CHAPTER 6

### PREDICTION AND OPTIMIZATION OF NANOSCALE RADIATION HEAT TRANSFER CONSIDERING DIFFERENT DOPING LEVELS OF SILICON

This chapter is devoted to investigating the near-field radiation heat transfer between two closely spaced semi-infinite media with parallel and smooth surfaces, especially with doped silicon. The two media are separated by a vacuum gap of width  $d$  range from several tens of microns to 1 nm. The motivation of this study has been stated in Chapter 1 and the fluctuational electrodynamics method presented in Chapter 2 will be used in the calculation. Currently, two kinds of geometric models have been extensively used in numerical simulations of near-field radiation heat transfer using the fluctuational electrodynamics method. One has been shown schematically in Figure 2.6(b) and described above, and has been the basic model for nanoscale thermophotovoltaic devices (Whale and Cravalho, 2002; Narayanaswamy and Chen, 2003). The other concerns radiation heat transfer between a sphere and the surface of a semi-infinite medium, where the sphere mimics the tip in a scanning tunneling microscope (Pendry, 1999; Mulet et al., 2001). This model, however, assumes that the sphere is positioned at a distance from the surface much greater than the radius of the sphere such that the sphere can be treated as a point-like dipole. In reality this assumption may not be correct as the tip can be placed at a distance from the surface much smaller than the curvature radius of the tip. The model in Figure 2.6(b), though cannot quantitatively predict the radiation heat transfer between a tip and a surface, has no such constraint on the vacuum gap width. Furthermore, predicted results using the model of Figure 2.6(b) can offer insight into the phenomenon of near-field radiation heat transfer. The results calculated by Polder and Van Hove (1971)

have been used to compare with the measured heat flux between a metallic tip and a sample surface (Müller-Hirsch et al., 1999). Therefore, the model of Figure 2.6(b) will be used in this work, especially for predicting the effect of dopant concentration of silicon on the radiation heat transfer at the nanoscale.

Equations (2.29)–(2.31) will be used to calculate the near-field radiation heat transfer in this work. But before the calculation the dielectric function of silicon needs to be determined. Lots of work has been devoted to modeling the optical properties of silicon. A Drude model (Hesketh et al., 1988; Auslender and Hava, 1995; Marquier et al., 2004) has been used for the dielectric function of doped silicon in the infrared region. The important parameters in this model are the free carrier concentration and the scattering time, which are functions of temperature and dopant concentration. Therefore, these parameters obtained at certain temperature and dopant concentration normally cannot be used to describe the dielectric function of silicon at other temperatures and dopant concentrations. It is desired to have a model that can account for the continuous change of the dielectric function of silicon as functions of temperature and dopant concentration. Such a model was proposed by Hebb (1997), which will be discussed in the next section and will be employed in this work for expressing the dielectric function of silicon.

## **6.1 The Dielectric Function of Silicon**

The model proposed by Hebb (1997) is essentially a Drude model and can account for the dielectric function of both intrinsic and doped silicon, which is given in the following expression:

$$\varepsilon = (n + i\kappa)^2 = \varepsilon_{ib-l} - \frac{N_e e^2 / \varepsilon_0 m_e}{\omega^2 + i\omega / \tau_e} - \frac{N_h e^2 / \varepsilon_0 m_h}{\omega^2 + i\omega / \tau_h} \quad (6.1)$$

where  $n$  is the refractive index and  $\kappa$  is the extinction coefficient,  $N_e$  and  $N_h$  are the concentrations,  $m_e$  and  $m_h$  the effective masses,  $\tau_e$  and  $\tau_h$  the scattering times for free electrons and holes, respectively,  $e$  is electron charge, and  $\varepsilon_{ib-l}$  denotes the contribution from absorption by transition across the band gap and lattice vibrations. In Equation (6.1), the effective masses  $m_e$  and  $m_h$  are assumed to be independent of frequency, dopant concentration, and temperature, and are taken as  $0.32m_0$  and  $0.37m_0$ , respectively, where  $m_0$  is the mass of an electron in vacuum. In the term  $\varepsilon_{ib-l}$ , contribution from electronic transition across the band gap is evaluated with the empirical formulae proposed by Timans (1996). Absorption by lattice vibration occurs for wavelengths greater than  $6 \mu\text{m}$  and is weak in silicon and has no significant effect on the refractive index. At high temperatures, the effect of absorption by lattice vibrations is negligible compared to the absorption by free carriers. According to Hebb (1997), the contribution to the dielectric function from lattice vibrations is assumed independent of temperature, and room temperature values of the extinction coefficient (Edwards, 1985) will be used. The parameters  $\tau_e$  and  $\tau_h$  depend on the collisions of electrons and holes with lattice and ionized dopant sites (impurities). The total scattering time, for the case of  $\tau_e$ , is calculated by the following formula:

$$\tau_e^{-1} = \tau_{e,l}^{-1} + \tau_{e,d}^{-1} \quad (6.2)$$

where  $\tau_{e,l}$  denotes the scattering time for collision with lattice and  $\tau_{e,d}$  the scattering time for collision with ionized dopant sites. The calculation of  $\tau_h$  follows the same rule.

The scattering times for collision with lattice do not depend on dopant concentration and have been fitted (Hebb, 1997) from experimental data for lightly doped silicon, which are expressed as

$$\tau_{e,l} = 9.98 \times 10^{-11} T^{-1.43} \quad (6.3)$$

and 
$$\tau_{h,l} = 6.24 \times 10^{-12} T^{-1.13} \quad (6.4)$$

where  $\tau_{e,l}$  and  $\tau_{h,l}$  are in s,  $T$  is in K. For silicon with higher dopant concentrations than  $10^{15} \text{ cm}^{-3}$ , the scattering time for collision with ionized dopant sites must be considered in order to calculate the total scattering time. The following approximations for the temperature dependence of  $\tau_{e,d}$  and  $\tau_{h,d}$  have been proposed (Hebb, 1997)

$$\tau_{e,d} = \beta_e T^{1.5} \quad (6.5)$$

and 
$$\tau_{h,d} = \beta_h T^{1.5} \quad (6.6)$$

where  $\beta_e$  and  $\beta_h$  depend on the dopant concentration but not on temperature, which can be extracted from the experimental values of mobility at room temperature. The total scattering time is related to the mobility by the following relations (Sze, 1981)

$$\tau_e = \mu_e m_e / e \quad (6.7)$$

and 
$$\tau_h = \mu_h m_h / e \quad (6.8)$$

where  $\mu_e$  and  $\mu_h$  represent the electron mobility and hole mobility, respectively. In this work,  $\mu_e$  and  $\mu_h$  as functions of dopant concentrations at room temperature are given the following two expressions (Beadle et al., 1985)

$$\mu_e = \frac{1268}{1 + (N_D \times 10^{-17} / 1.3)^{0.91}} + 92 \quad (6.9)$$

and

$$\mu_h = \frac{447.3}{1 + (N_A \times 10^{-17} / 1.9)^{0.76}} + 47.7 \quad (6.10)$$

where  $\mu_e$  and  $\mu_h$  are in  $\text{cm}^2/\text{V}\cdot\text{s}$ ,  $N_D$  and  $N_A$  denote dopant concentration of n-type (donor) and p-type (acceptor) and are in  $\text{cm}^{-3}$ . Note that  $\mu_e$  in Equation (6.9) was measured versus  $N_D$  in Phosphorus-doped silicon and  $\mu_h$  in Equation (6.10) was measured versus  $N_A$  in Boron-doped silicon (Beadle et al., 1985). It is assumed in this work that Phosphorus and Boron are the donor and acceptor in silicon. A silicon crystal at any values of  $N_D$  and  $N_A$  should satisfy electrical neutrality (Sze, 1981). This condition is used to evaluate the values of  $N_e$  and  $N_h$  for given temperature and dopant concentration. The calculation of  $N_e$  and  $N_h$  in this work is performed using a free software FERMI2 (Gaylord and Linxwiler, 1976).

From Equations (6.3) and (6.5),  $\tau_{e,l}$  decreases when increasing temperature while  $\tau_{e,d}$  increases with temperature. The temperature dependence of the total scattering time  $\tau_e$  calculated from Equation (6.2) is shown in Figure 6.1 for various dopant concentrations. It can be seen that  $\tau_{e,l}$  dominates the scattering time at high temperatures while  $\tau_{e,d}$  is important at low temperatures. Validation of the model in Equation (6.1) is

performed by comparing the absorption coefficient  $\alpha = 2\omega\kappa/c$  of intrinsic silicon with the results obtained from the empirical formulae given by Timans (1996), which is shown in Figure 6.2(a) as a function of  $\omega$  for various temperatures. The contribution to  $\alpha$  from lattice vibrations is small at the high temperatures that it is neglected in Figure 6.2(a). The absorption coefficient  $\alpha$  for doped silicon is shown in Figure 6.2(b) versus temperature for the wavelength  $\lambda = 1.3 \mu\text{m}$  and compared with experimental data (Timans, 1996). The comparison indicates that Equation (6.1) is appropriate for describing the dielectric function of silicon under the prescribed conditions. The model of Equation (6.1) has been used by Hebb (1997) in the temperature range from 300 K up to 1400 K and for dopant concentrations up to greater than  $10^{20} \text{ cm}^{-3}$ .

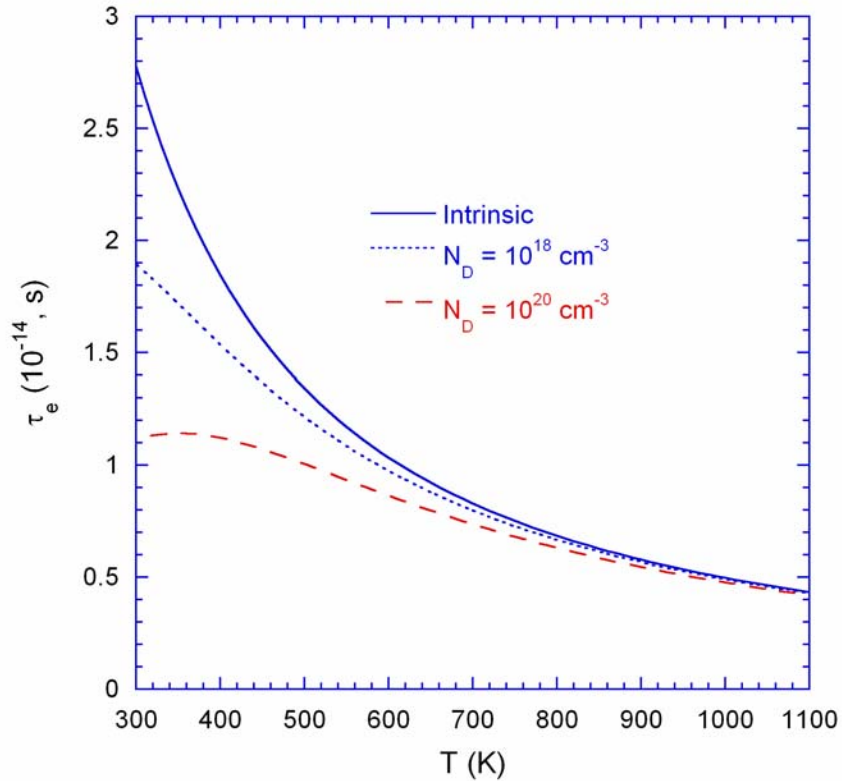


Figure 6.1 The electron scattering time of silicon changes with temperature and dopant concentration.



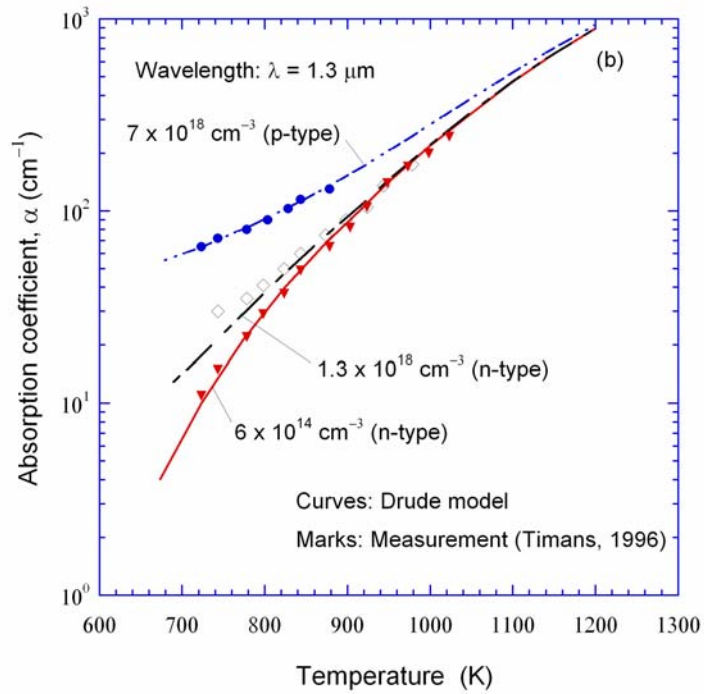
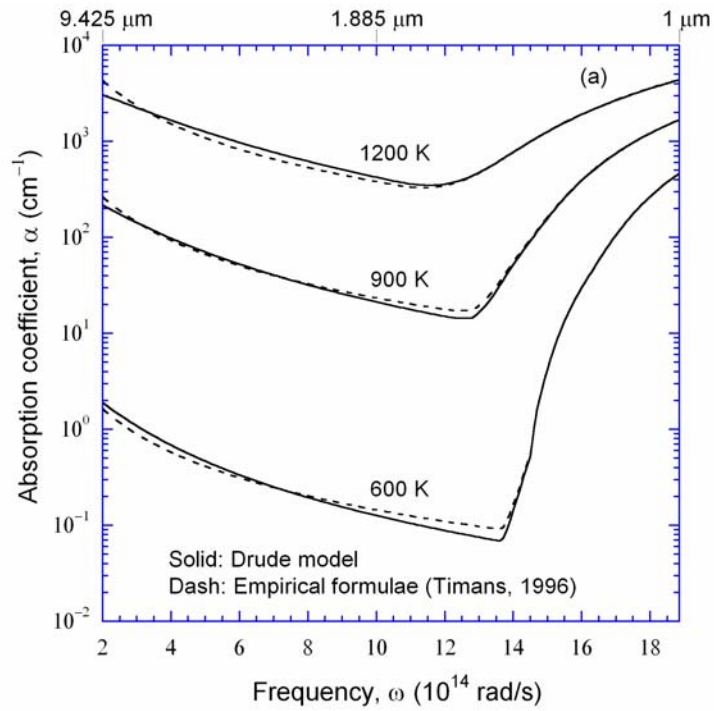


Figure 6.2 The absorption coefficient of (a) intrinsic and (b) doped silicon, obtained from the Drude model, Equation (7), and the empirical formulae from Timans (1996). Note that the same equation is used to evaluate  $\epsilon_{ib-l}$  in both models.

## 6.2 Energy Density of Thermally Emitted EM Fields from a Flat Surface

The spectral energy density  $u(z, \omega)$  emitted from a flat surface of silicon can be calculated with Equations (6.1) and (2.28). The calculated  $u(z, \omega)$  for the surface temperature equal to 1000 K and at various heights above the surface is plotted in Figure 6.3. The result shows different profiles of  $u(z, \omega)$  for different  $z$  values. From the radiation spectra of a blackbody at 1000 K, the maximum of the energy density appears at  $\omega \approx 3.69 \times 10^{14}$  rad/s. In Figure 6.3, a maximum  $u(z, \omega)$  appearing at  $\omega \approx 3.69 \times 10^{14}$  rad/s can be seen for the cases of  $z = 1$  mm and  $10 \mu\text{m}$ . It has been shown in Equation (2.28) that  $u(z, \omega)$  includes contributions from propagating waves and

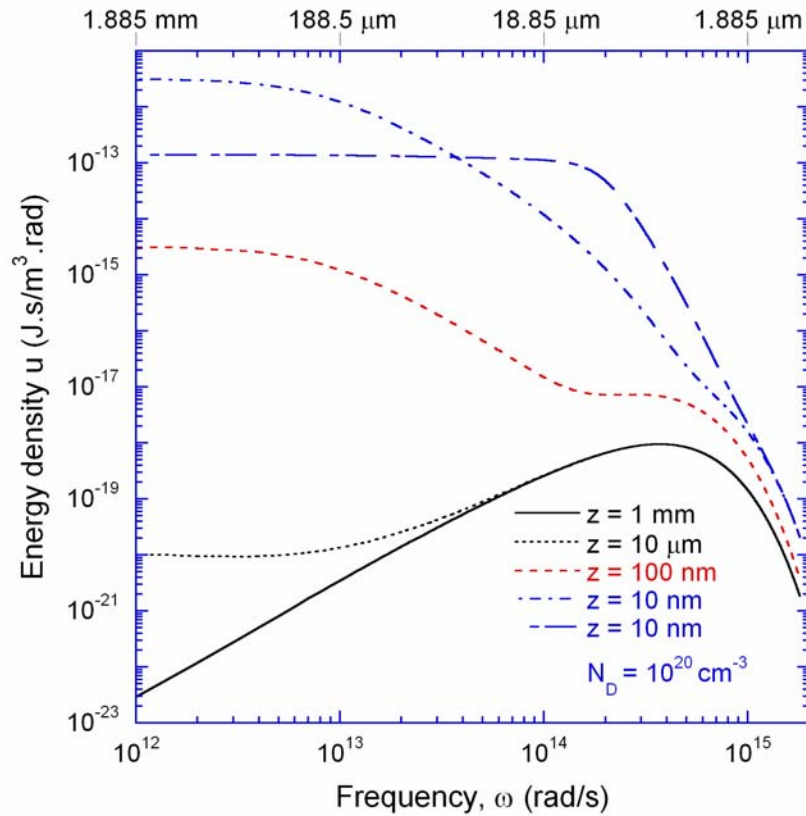


Figure. 6.3 The evolution of the energy density emitted from a silicon surface at 1000 K. The curves are plotted for different heights above the surface.

evanescent waves. Because evanescent waves decay exponentially away from the surface, their contribution to the energy density is negligible for  $z > \omega/c$ . But if  $z \ll \omega/c$ , evanescent waves will make tremendous contribution to the energy density so that much larger energy density can be obtained, as shown in Figure. 6.3 for the cases of  $z = 10$  and  $100$  nm. Note also from Figure. 6.3 that if the silicon is doped  $N_D = 10^{20} \text{ cm}^{-3}$ ,  $u(z, \omega)$  for  $z = 10$  nm has significant difference compared to that of an intrinsic silicon. In order to see in depth the dependence of  $u(z, \omega)$  on  $z$  and dopant concentration, rewrite Equation (2.28) as

$$u(z, \omega) = N(z, \omega)\Theta(\omega, T) \quad (6.11)$$

where  $N(z, \omega)$  accounts for the density of modes per unit volume. According to Pendry (1999), the density of modes for  $z \ll \omega/c$  is dominated by evanescent waves of  $p$ -polarization for nonmagnetic materials. Using Asymptotic expansion, it has been shown (Shchegrov et al., 2000; Joulain et al., 2003) that  $N(z, \omega)$  for  $z \ll \omega/c$  can be approximated, in large  $K$  limit, as

$$N(z, \omega) \approx \text{Im}(r_{12}^p) \frac{1}{8\pi^2 \omega z^3} \approx \text{Im} \left( \frac{\varepsilon_1 - 1}{\varepsilon_1 + 1} \right) \frac{1}{8\pi^2 \omega z^3} \quad (6.12)$$

The  $z^{-3}$  dependence of  $N(z, \omega)$  on  $z$  makes  $N(z, \omega)$  decrease much faster than the exponential decay, resulting in large  $N(z, \omega)$  only localize very close to the surface.

The dependence of  $N(z, \omega)$  on dopant concentration can be seen from the dependence of

$\text{Im} \left( \frac{\varepsilon_1 - 1}{\varepsilon_1 + 1} \right)$  on dopant concentration. Substituting  $\varepsilon_1$  with the dielectric function of

silicon at  $T = 1000$  K,  $N(z, \omega)$  from Equation (6.12) as a function of  $\omega$  is shown in

Figure. 6.4 for  $z = 10$  nm. Comparing the curves for  $z = 10$  nm in Figures 6.3 and 6.4, the energy density is clearly seen to follow the trend of  $N(z, \omega)$ .

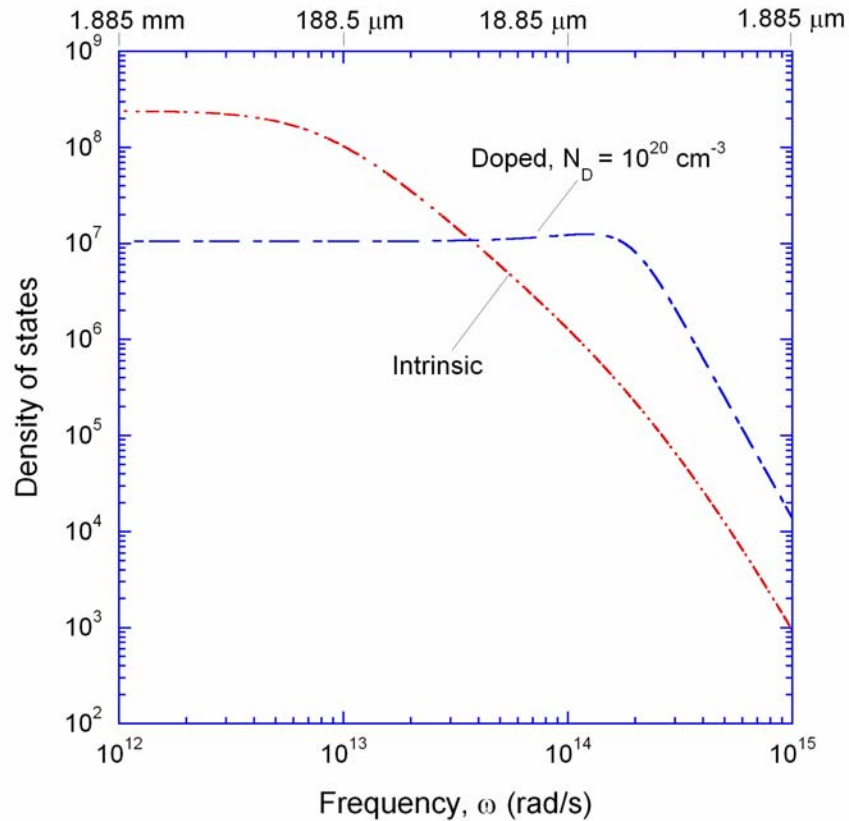


Figure 6.4 Estimated density of modes for  $z = 10$  nm above the surface of an intrinsic silicon and an n-type silicon (dopant concentration  $N_D = 10^{20} \text{ cm}^{-3}$ ) at 1000 K.

### 6.3 Net Energy Flux between Silicon and Silicon

The radiation heat transfer between two semi-infinite media is calculated using Equations (2.29) – (2.31). In the case that the two media are both intrinsic silicon and medium 1 is maintained at 1000 K while medium 2 is at 300 K. The calculated net spectral energy flux between the two media is shown in Figure 6.5(a) for different values

of the vacuum gap width  $d$ . Although the flux magnitude increases as  $d$  decreases, the feature looks similar to the Planck blackbody radiation even for  $d$  as small as 100 nm. Small deviation is observed when  $d$  is further reduced to 10 nm, which is only at low frequencies. The oscillation for  $d = 10 \mu\text{m}$  is due to wave interference in the vacuum gap. The net energy flux is obtained by integrating the net spectral energy flux over  $\omega$ . The result is shown in Figure 6.5(b). The dotted line denotes the net energy flux calculated with the traditional Stefan-Boltzmann law if both media are assumed blackbodies. Wien's displacement law (Siegel and Howell, 2002) determines that dominant wavelength  $\lambda_{max}$  for the 1000 K emitter is around  $3 \mu\text{m}$ . The energy flux is essentially a constant when the gap width  $d$  is greater than  $3 \mu\text{m}$ , which is the far-field regime. When  $d < \lambda_{max}$ , the net energy flux first increases rapidly. This increase of the net energy flux with reducing gap width slows down when  $d < 100 \text{ nm}$ . The net energy flux approaches a finite value and changes little when  $d < 10 \text{ nm}$ . The saturated net energy flux is 21 times that of the far-field limit and 11 times that with blackbodies. The case when the emitter is a doped silicon with  $N_D = 10^{20} \text{ cm}^{-3}$  is also calculated. The result in the near-field regime, which can be seen in Figure 6.5(b), is slightly smaller than that for the emitter being intrinsic silicon. In fact, this result is caused by the intrinsic silicon at 300 K. An intrinsic silicon at 300 K is almost lossless (i.e.,  $\kappa = 0$ ). According to Cravalho et al. (1967) and Pan (2000), the maximum heat flux from an emitter to a lossless dielectric is bounded to the Planck radiation of a blackbody at the emitter temperature times the dielectric function of the receiver.

The above problem may be better understood if the heat transfer is treated to be through channels proposed by Pendry (1999): each wave vector corresponds to a channel,

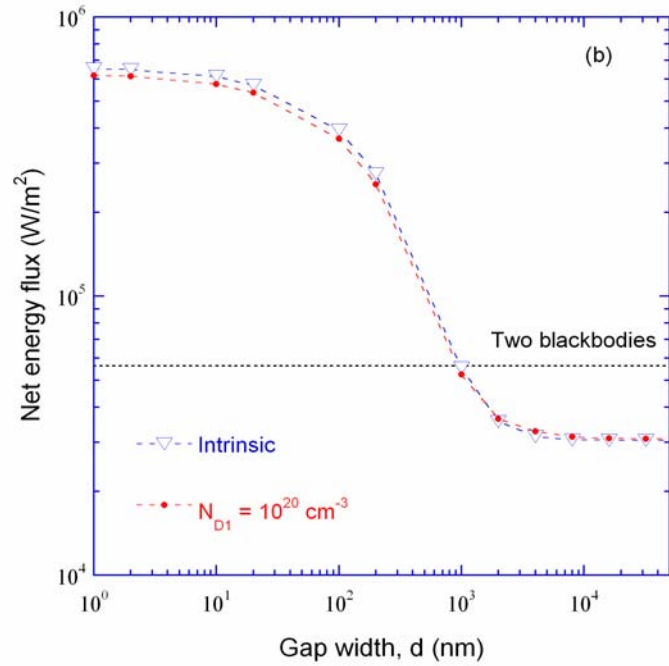
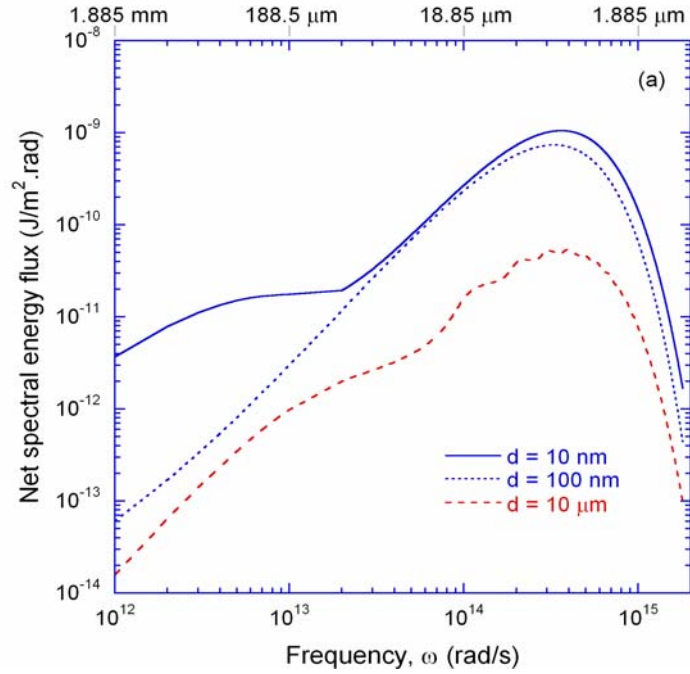


Figure 6.5 The energy flux between two semi-infinite intrinsic silicon media: (a) spectral distribution for different values of  $d$ , (b) the net total energy flux between the two silicon media as a function of  $d$ . The high temperature medium at 1000 K is separated from the low temperature medium at 300 K by a vacuum of width  $d$ .

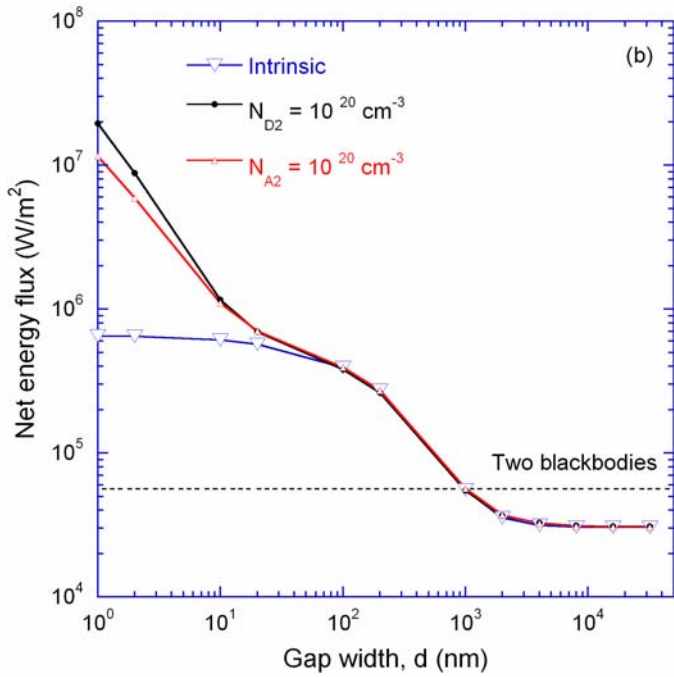
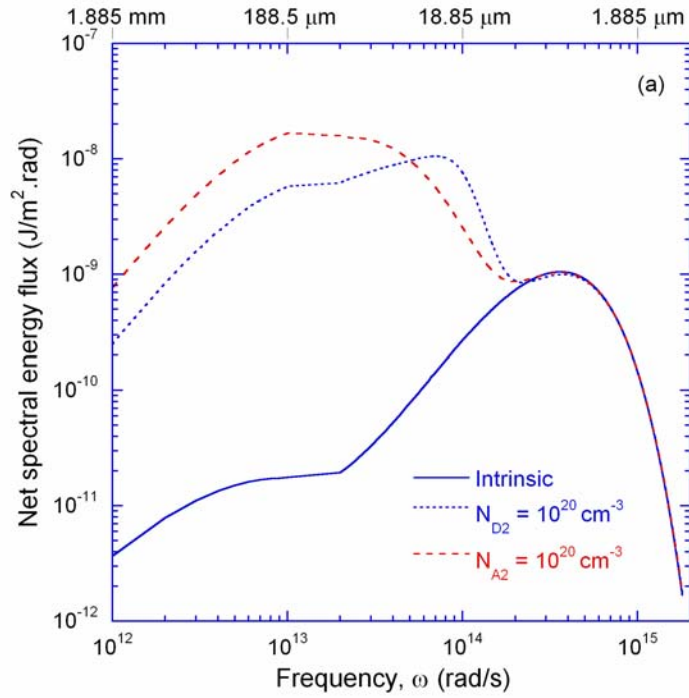


Figure 6.6 The effect of doping on the net (a) spectral energy density and (b) total energy density between the two silicon media. Doped silicon is only for the low temperature medium and (a) is drawn with  $z = 10$  nm.

or mode, through which heat can flow. Therefore, large heat transfer is characterized by large number of channels available for heat flow. Recall from Equation (6.12) that the density of modes outside the surface of medium 1 is proportional to  $\text{Im}[(\epsilon_1 - 1)/(\epsilon_1 + 1)]$ . Similarly, the density of modes outside the surface of medium 2 should also be proportional to  $\text{Im}[(\epsilon_2 - 1)/(\epsilon_2 + 1)]$ . The number of channels through which heat can flow is proportional to the product of  $\text{Im}[(\epsilon_1 - 1)/(\epsilon_1 + 1)]$  and  $\text{Im}[(\epsilon_2 - 1)/(\epsilon_2 + 1)]$ . In fact, a rough estimate of the net spectral heat flux for small  $d$  can has been given by Mulet et al. (2002) as

$$q''_{\omega,1-2} - q''_{\omega,2-1} \approx \frac{1}{4\pi^2 d^3} \text{Im}\left(\frac{\epsilon_1 - 1}{\epsilon_1 + 1}\right) \text{Im}\left(\frac{\epsilon_2 - 1}{\epsilon_2 + 1}\right) [\Theta(\omega, T_1) - \Theta(\omega, T_2)] \quad (6.13)$$

From Equation (6.13), it is not surprising that the energy flux in Figure 6.5 is small. Because  $\text{Im}[(\epsilon_2 - 1)/(\epsilon_2 + 1)]$  is small for intrinsic silicon at room temperature. Large energy flux for small  $d$  depends on a large  $\text{Im}[(\epsilon_2 - 1)/(\epsilon_2 + 1)]$ . Come back to the case of Figure 6.5 and consider that medium 2 is doped silicon. The net spectral energy flux is recalculated and the results are shown in Figure 6.6(a) for  $N_{D2} = 10^{20} \text{ cm}^{-3}$  ( $N_{A2} = 10^{20} \text{ cm}^{-3}$  for  $p$ -type) and  $d$  fixed at 10 nm, where the subscript 2 means doping is for medium 2. It can be seen that the net spectral energy flux is greatly improved for the angular frequency  $\omega < 10^{14} \text{ rad/s}$ . The corresponding net energy flux is shown in Figure 6.6(b). From the figure, the net energy flux follows the same trend as in Figure 6.5 (b) when  $d$  decreases from 32  $\mu\text{m}$  to 100 nm, indicating that the number of channels for heat flow is not improved when  $d$  is greater than 100 nm. However, the net energy flux increases rapidly when  $d$  is reduced to less than 20 nm and this increase does not saturate even for



$d = 1$  nm, where the net energy flux is enhanced by more than one order in magnitude compared with Figure 6.5(b).

Equation (6.13) provides a way for optimizing the near-field radiative heat transfer by tuning the optical properties of the emitter and receiver, which can be done in silicon by changing the dopant concentration. In order to see clearly how the dielectric function of silicon will be affected by dopant concentration, the real part  $\varepsilon'$  and the imaginary part  $\varepsilon''$  of the dielectric function of silicon as functions of  $\omega$  are plotted in Figure 6.7 at temperatures of 1000 K and 300 K and for different dopant concentrations.

In essence,  $\varepsilon'$  decreases while  $\varepsilon''$  increases with adding dopants. A negative  $\varepsilon'$  indicates the material is metallic like and  $\varepsilon''$  is very large. From Equation (6.13), a very large  $\varepsilon''$  will result in small density of modes. The optimum net energy flux requires the number density of heat flow channels maximizes around where  $\Theta(\omega, T)$  also maximizes for a

given temperature  $T$ . The result of the material parameter  $\Phi = \text{Im}\left(\frac{\varepsilon_1 - 1}{\varepsilon_1 + 1}\right) \text{Im}\left(\frac{\varepsilon_2 - 1}{\varepsilon_2 + 1}\right)$  as

a function of  $\omega$  for  $T_1 = 1000$  K and  $T_2 = 300$  K is plotted in Figure 6.8. From the figure,

the peak of  $\Phi$  will shift to higher frequencies when the dopant concentrations in medium 1 and medium 2 are increased. But the magnitude of the peak does not always increase

with dopant concentrations. For example, when the dopant concentrations in medium 1

and medium 2 are both equal to  $10^{21} \text{ cm}^{-3}$ , the peak of  $\Phi$  has been smaller than the case

when dopant concentration is equal to  $10^{20} \text{ cm}^{-3}$  in medium 1 but is equal to  $10^{21} \text{ cm}^{-3}$  in

medium 2. The net energy flux is also calculated under the indicated conditions and

shown in Figure 6.9. The largest net energy flux is found for  $N_{D1} = 10^{20} \text{ cm}^{-3}$  and

$N_{D2} = 10^{21} \text{ cm}^{-3}$ , consistent with Figure 6.8. The maximum net energy flux for  $d = 1$  nm

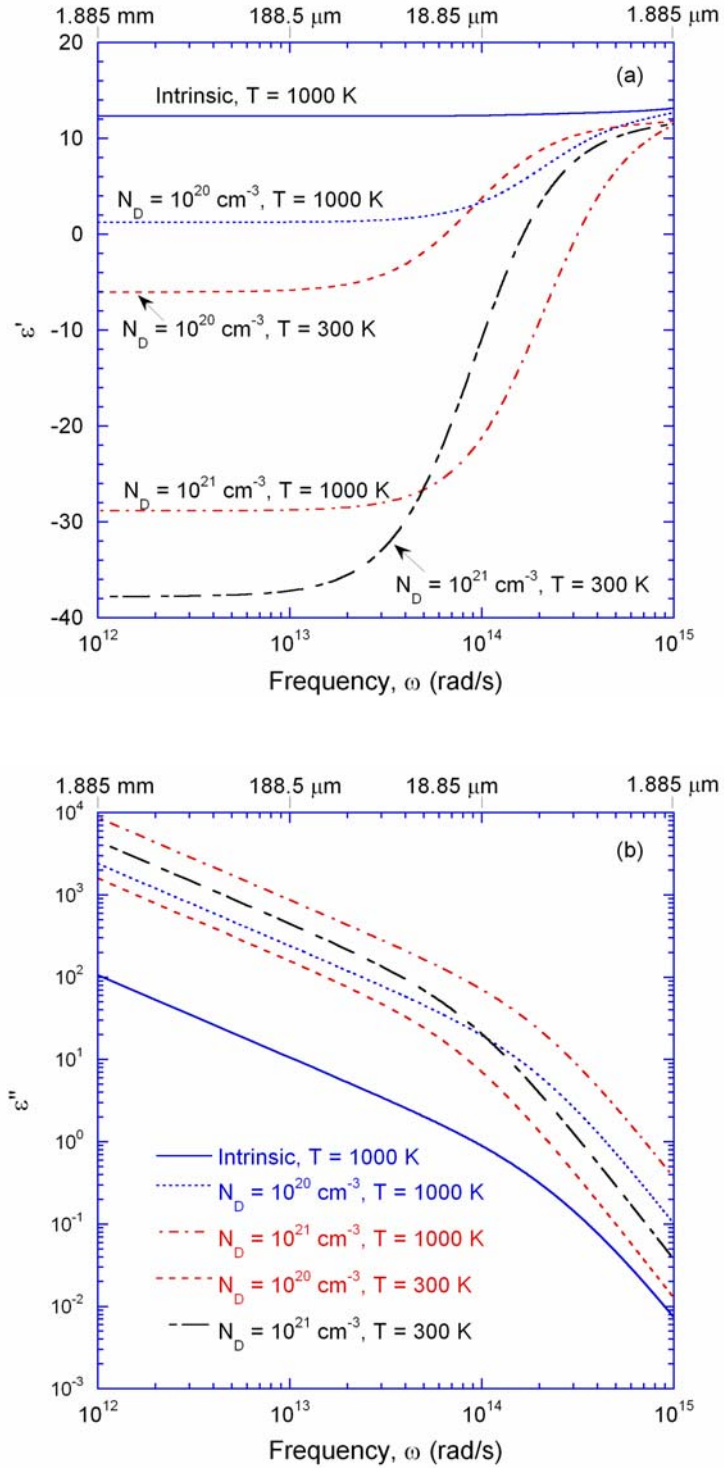


Figure 6.7 The change of the (a) real part and (b) imaginary part of the dielectric function of silicon with angular frequency at different temperatures and dopant concentrations.

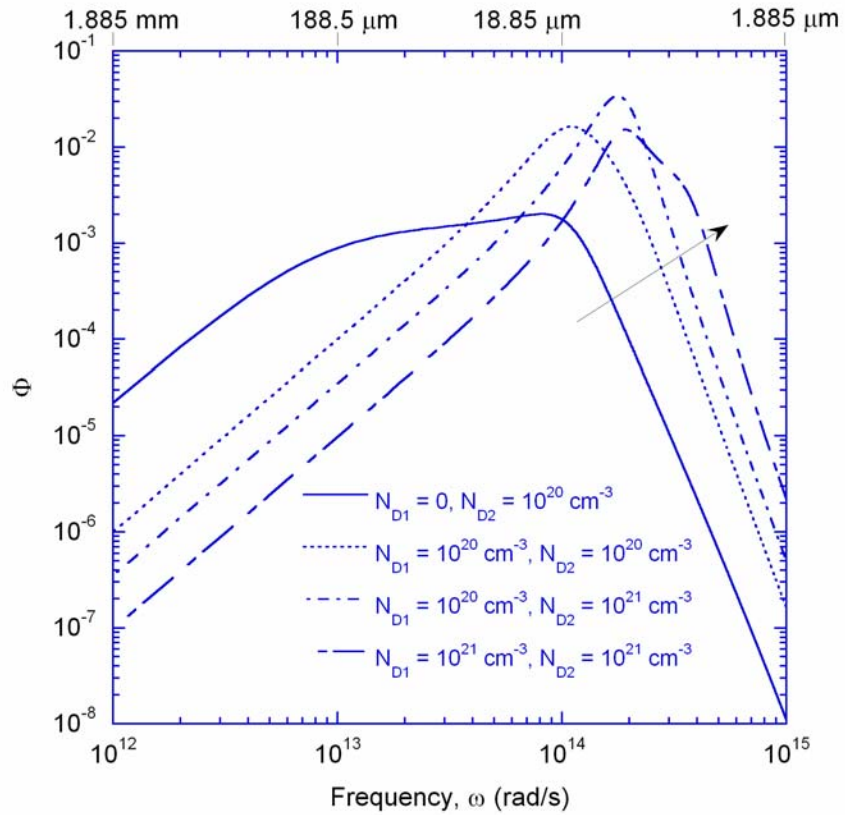


Figure 6.8 The parameter  $\Phi$  drawn as a function of angular frequency showing the change of the number density of heat flow channels at different dopant concentrations. The subscripts 1 and 2 denote medium 1 and medium 2.

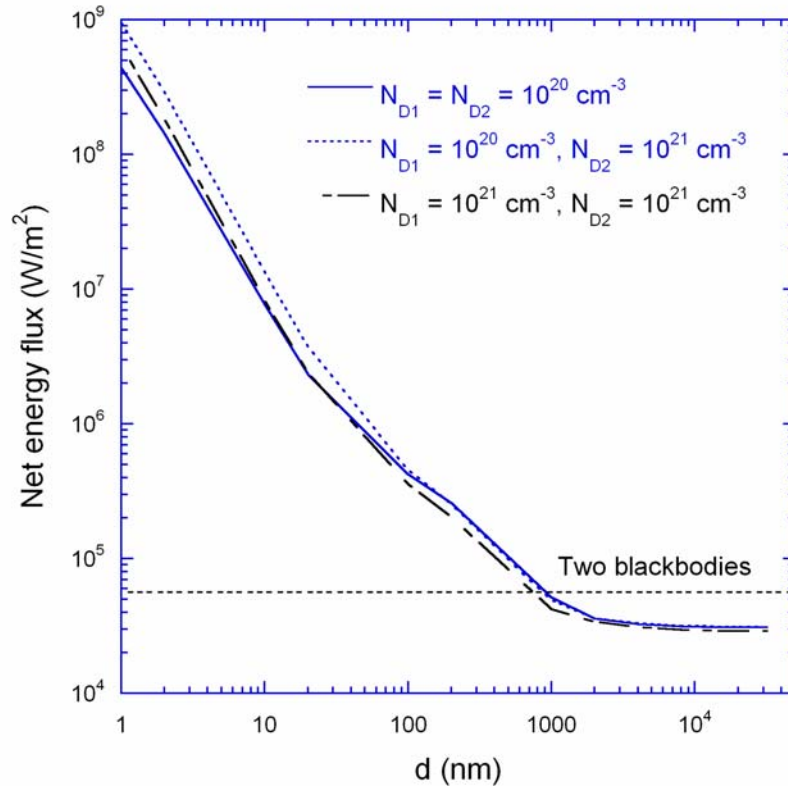


Figure 6.9 Net energy flux obtained for small  $d$  with both media being n-type silicon with dopant concentration between  $10^{20}$  and  $10^{21}$   $\text{cm}^{-3}$ .

is over three orders in magnitude greater than those in Figure 6.5.

In the above investigations, the temperatures of medium 1 and medium 2 are set at  $T_1 = 1000$  K and  $T_2 = 300$  K, respectively, and the net radiation energy flux is calculated for various doping concentrations of silicon. In order to investigate the effect of temperature on the net energy flux, the dopant concentrations of both medium1 and

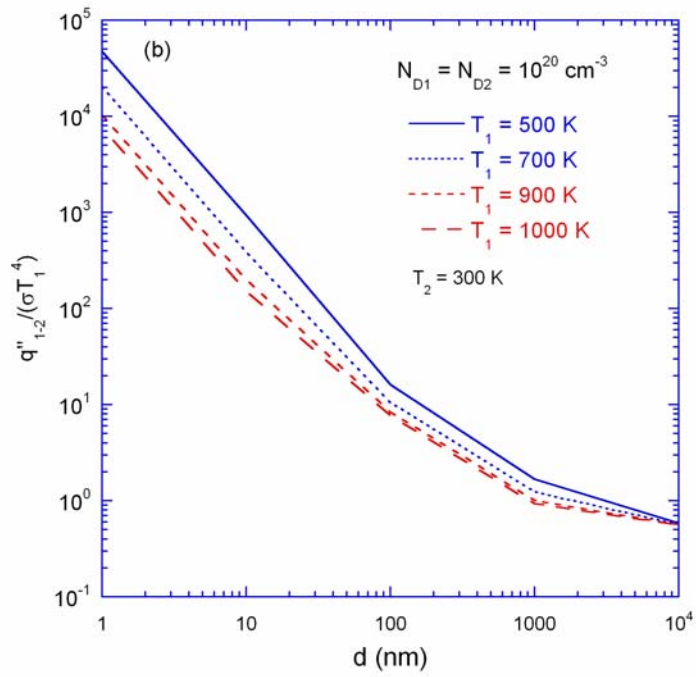
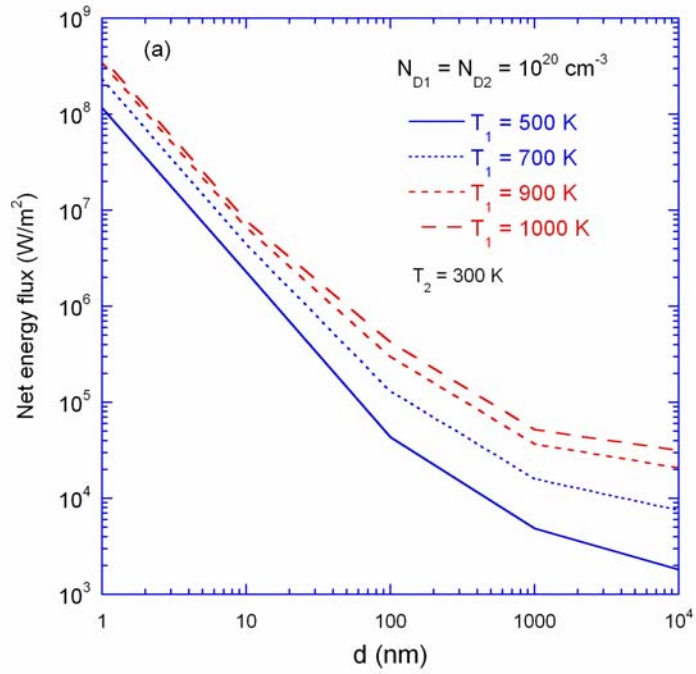


Figure 6.10 The effect of temperature on the radiation energy flux between two doped silicon: (a) the net energy flux and (b) the energy flux from medium 1 to medium 2 normalized by  $\sigma T_1^4$ .

medium 2 are fixed at  $N_{D1} = N_{D2} = 10^{20} \text{ cm}^{-3}$  and the net energy flux is calculated for different values of  $T_1$ . The calculated net energy flux is shown in Figure 6.10(a). It is interesting to find that when  $d$  is equal to  $10 \text{ }\mu\text{m}$ , the ratio of the net energy flux for  $T_1 = 1000 \text{ K}$  to that for  $T_1 = 500 \text{ K}$  is 15.4; but when  $d$  is equal to  $1 \text{ nm}$ , this ratio is only 3.37. The radiation energy flux from medium 1 to medium 2  $q''_{1-2}$  normalized by  $\sigma T_1^4$ , where  $\sigma = 5.67 \times 10^{-8} \text{ W/m}^2 \cdot \text{K}^4$  is the Stefan-Boltzmann constant, is shown in Figure 6.10(b). From this figure, the normalized  $q''_{1-2}$  is almost the same for all the four temperatures at  $d = 10 \text{ }\mu\text{m}$ , but very large differences can be seen at  $d = 1 \text{ nm}$ , where the  $q''_{1-2}$  decreases with increasing the temperature  $T_1$ . These two figures show that a smaller  $T_1$  may be more efficient to achieve large radiation energy flux in the near field.

#### 6.4 Net Energy Flux between Silicon and Silicon Carbide or Metal

Silicon carbide (SiC) has been extensively studied for using to enhance radiative heat transfer in the near field. It has been shown that the excitation of surface phonon polaritons (Surface waves) on SiC surface can significantly enhance the heat transfer (Narayanaswamy and Chen, 2003; Mulet et al., 2002). The heat transfer enhancement is because excitation of surface phonon polariton provides a large number of additional surface modes near the excitation frequency and these surface modes can be coupled to the second material (Shchegrov et al., 2000). However, the density of modes is small for frequencies not close to the excitation frequency because of the small value of  $\epsilon''$  in SiC. In other words, SiC cannot provide a large number of heat flow channels without surface waves. Replacing the room temperature medium (medium 2) with SiC and setting

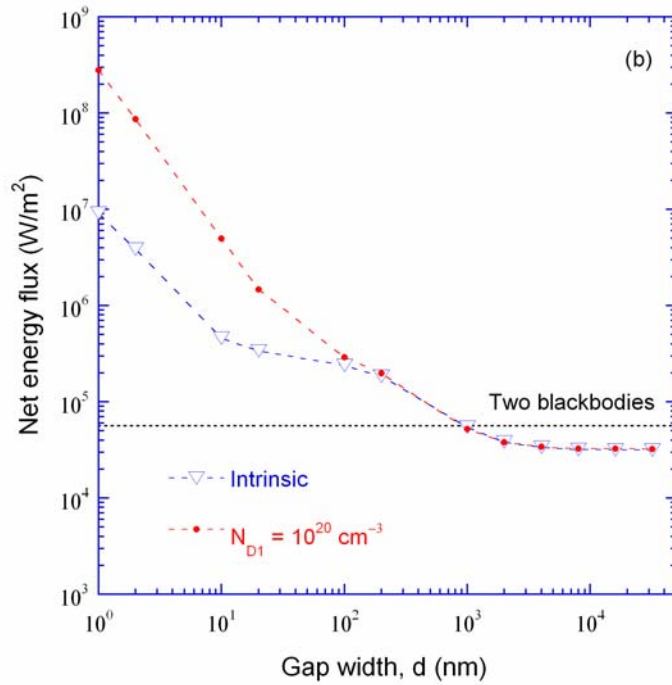
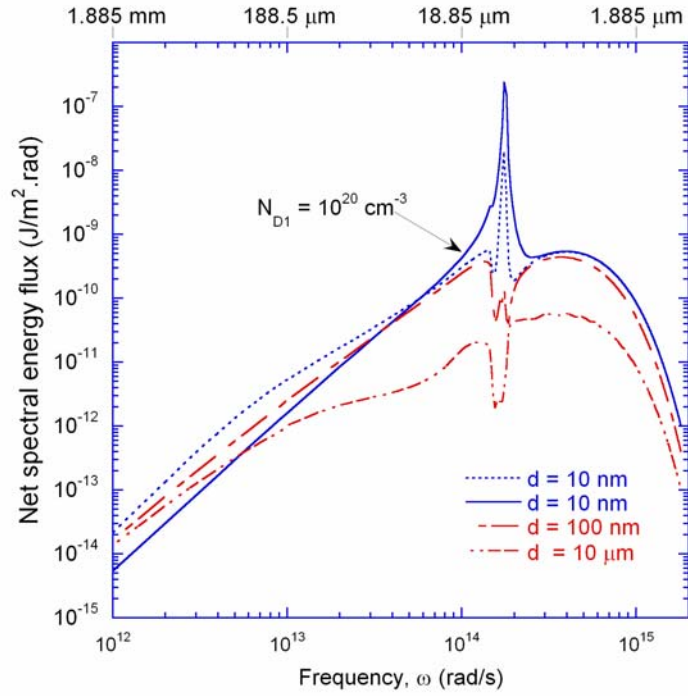


Figure 6.11 The net (a) spectral energy flux and (b) total energy flux between Si at 1000K and SiC at 300 K. The sharp peak in (a) is due to excitation of surface phonon polaritons on the SiC surface.

medium 1 of silicon at 1000 K, the net spectral energy flux of Si-SiC is calculated for different values of  $d$  and shown in Figure 6.11(a). Note that in the frequency range from  $1.5 \times 10^{14}$  rad/s to  $1.82 \times 10^{14}$  rad/s,  $\epsilon'$  of SiC is negative, i.e., small emissivity, the emitted spectrum in this range is low for  $d = 10 \mu\text{m}$  (far field). When  $d$  is decreased to the near-field regime such that evanescent waves come into affect the heat exchange, surface phonon polaritons are excited on the SiC surface at the frequency where  $\epsilon' = -1$  (Mulet et al., 2002). A large number of surface modes excited facilitate to enhance heat transfer, denoted by the sharp peak in Figure 6.11(a). However, the energy flux elsewhere is much lower than in the case of Si-Si. Therefore, heat transfer enhancement is totally confined in a narrow frequency range. As a result, the net total energy flux, shown in Figure 6.11(b), displays a lower value than that in Figure 6.9 for  $d < 100 \text{ nm}$ .

Most metals exhibit high reflection in the infrared region. For thermal radiative in near-field, metals are also bad candidates to have large heat transfer rate due to the small density of modes in the infrared region. Consider the case that a semi-infinite medium of aluminum at room temperature (300 K), whose dielectric function is taken from the work of Smith et al. (1998), is subjected to heat radiation from a 1000 K thermal source of doped silicon. The net energy flux change with  $d$  from the far field regime to the near field regime is shown in Figure 6.12. The enhancement can be up to three orders in magnitude when the net energy flux in the near field regime is compared with that in the far field regime, but the absolute value is so small that even for  $d < 100 \text{ nm}$ , the net energy flux is smaller than the value given by the Stefan-Boltzmann law of two blackbodies. Other metals such as silver and copper have also been investigated; the results are similar to Figure 6.12 and thus will not be discussed here.



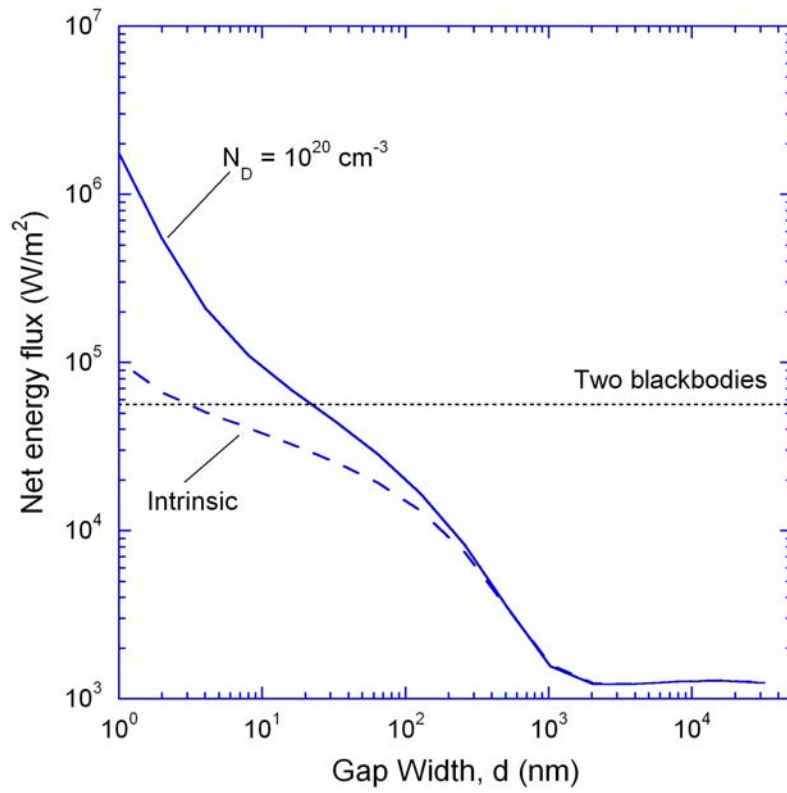


Figure 6.12 The net total energy flux between Si at 1000 K and Al at 300 K.

## CHAPTER 7

### CONCLUSIONS AND RECOMMENDATIONS FOR FUTURE WORK

This dissertation research has unveiled several spectacular features of NIMs with respect to the radiative properties and radiative transfer in multilayer structures. First of all, energy transmission through photon tunneling can be greatly enhanced by the amplification of evanescent waves associated with the surface plasmon polariton. Secondly, the coherence thermal emission has been predicted using a heterogeneous structure constructed by pairing layers of a single negative  $\epsilon$  and a single negative  $\mu$ . Furthermore, a detailed account of the conditions of occurrence of the Brewster angle, at which the reflectance is zero, is theoretically performed. The major conclusions of this dissertation regarding NIMs are summarized below.

Energy transmission in multilayer structures via photon tunneling can be greatly enhanced using a layer of an NIM, especially when the NIM is at the perfect index matching condition. The enhancement is due to the excitation of surface or bulk polaritons, but depends on the thickness of the NIM layer that could be tuned to produce optimal performance. Furthermore, it is found that subdividing the NIM layers into many thinner layers and placing them alternately with vacuum gaps can have greater enhancement, especially at large incidence angles. The enhancement is attributed to the coupling of surface and bulk polaritons that reinforce the EM fields in the structure. By coupling more photons into the structure, a large increase in the transmission of evanescent waves and a reduction of the reflectance are observed using multilayer

structures. The result of the present study may benefit future applications of NIMs in microscale energy conversion and optical communication.

A novel coherent thermal emission source is proposed to construct using a bilayer where a thin layer having a negative  $\epsilon$  but a positive  $\mu$  is paired with a thick substrate having a negative  $\mu$  but a positive  $\epsilon$ . It has been shown that surface polaritons can be excited at the interface of the two layers. The excited surface polaritons can couple directly with thermal emission from the bilayer, resulting in a narrow emission band for a given direction and angular emission lobes for a given frequency. Therefore, thermal emission for the bilayer can be coherent. The merits of such a coherent thermal emission source are that coherent thermal emission of both  $s$ - and  $p$ -polarizations is possible and no grating is needed, while coherent thermal emission from a grating is only possible for  $p$ -polarization. Furthermore, a three-layer structure was also proposed for constructing a coherent thermal emission source, where the top layer and the substrate are made of the negative  $\epsilon$  material and the layer in the middle has a negative  $\mu$  (or vice versa), the advantage of such a three-layer structure over the bilayer is that for a given emission direction, changing the thickness of the mid-layer can control the frequencies of the coherent thermal emission. Potential applications of a coherent thermal emission source may be in radiative cooling and in infrared photovoltaic devices.

It has been shown that a Brewster angle can exist not only for  $p$ -polarization but also for  $s$ -polarization when a plane wave is incident on an NIM; and that the existence of a Brewster angle does not, in general, result in the refracted wave being perpendicular to the reflected/incident wave. Only under the condition that  $\epsilon_1 = \pm\epsilon_2$  or  $\mu_1 = \pm\mu_2$  will the refracted wave be perpendicular to the reflected/incident wave at the Brewster angle. A

regime map that is based on the permittivity and permeability of the two media was developed to delineate the regions a Brewster angle can exist for incidence of certain polarized plane waves. Physical explanations that account for the outcome of the Brewster angle for a plane wave incident upon an NIM have also been derived according to the Ewald-Oseen extinction theorem and induced dipoles re-emission from inside the NIM. The conclusions coming along with the occurrence of a Brewster angle in the case of an NIM may be a useful supplement to the understanding of the material's electromagnetic behavior, and may help the development of potential applications of negative index materials in advanced technologies.

This dissertation also investigates the radiation heat transfer at the nanoscale related to silicon. The net heat flux between two semi-infinite media separated at nanometric distances, of which the high-temperature medium is assumed silicon and the low-temperature medium can be silicon, silicon carbide or aluminum, was calculated using the fluctuational electrodynamics. A Drude model that considers the effects of temperature and dopant concentration on the free carrier concentration and scattering times was used for modeling the dielectric function of silicon. The low-temperature medium was set at 300 K. It was found that when the two media are both intrinsic silicon, the net heat flux will become saturated for the separation distance less than 20 nm and the saturated value is only one order greater in magnitude than that calculated from the Stefan-Boltzmann law. The net energy flux slightly drops off if the emitter is doped silicon. Very large net heat flux appears for both media being doped silicon and the net heat flux does not saturate even for the vacuum gap thickness of 1 nm. A maximum radiative energy flux from an n-type silicon at 1000 K to another n-type silicon at room

temperature was found to exist, with the dopant concentration of both media on the order of  $10^{20} \text{ cm}^{-3}$ . The net heat flux between silicon and silicon carbide or silicon and aluminum is also calculated. But results are smaller than the maximum heat flux between silicon and silicon. The enhancement of radiation heat transfer at the nanoscale may have an impact on the development of near-field thermal probing and nanomanufacturing techniques.

This dissertation demonstrates some unique radiative properties for applications in energy conversion devices. It is important to develop NIMs at higher frequencies in order to experimentally demonstrate the enhancement of photon tunneling and coherent thermal emission. The effect of anisotropy on the radiative properties should be further investigated. Further work is also needed to study the effect of coatings on the net heat flux at the nanoscale. For example, both media may be coated with absorbing and semitransparent films so that the radiation net heat flux can achieve optimized spectral distribution of the transmitted and reflected radiation. This will require the use of a much complicated dyadic Green function. The radiation heat transfer between a nanoobject, such as an AFM cantilever tip, and a flat surface should also be predicted and experimentally determined.

## REFERENCES

- Abeles, F., "Surface Plasmon (SEM) Phenomena," in *Electromagnetic Surface Excitations* (Wallis, R.F., and Stegeman, G.I., eds.), Springer-Verlag, Berlin, 1985.
- Alu, A., and Engheta, N., "Pairing an Epsilon-Negative Slab with a Mu-Negative Slab: Resonance, Anomalous Tunneling and Transparency," *IEEE Trans. Antennas and Propagation*, vol. 51, pp. 2558-2571, 2003.
- Auslender, M., Hava, S., "Zero Infrared Reflectance Anomaly in Doped Silicon Lamellar Gratings. I. From Antireflection to Total Absorption," *Infrared Phys. Technol.*, vol. 36, pp. 1077-1088, 1995.
- Beadle, W.E., Tsai, J.C.C., and Plummer, R.D., *Quick Reference Manual for Silicon Integrated Circuit Technology*, John Wiley, 1985.
- Berman, P.R. "Goos-Hänchen Shift in Negatively Refractive Media," *Phys. Rev. E*, vol. 66, pp. 067603/1-3, 2002.
- Born, M., and Wolf, E., *Principles of Optics*, 7<sup>th</sup> ed., Cambridge University Press, Cambridge, 1999.
- Buckman, B., *Guided Wave Photonics*, Saunders College Publishing, New York, pp. 35-85, 1992.
- Caren, R.P., "Thermal Radiation between Closely Spaced Metal Surfaces at Low Temperatures due to Traveling and Quasi-Stationary Components of the Radiation Field," *Int. J. Heat Mass Transfer*, vol. 17, pp. 755-765, 1974.
- Carminati, R., and Greffet, J.-J., "Near-Field Effects in Spatial Coherence of Thermal Sources," *Phys. Rev. Lett.*, vol. 82, pp. 1660-1663, 1999.
- Cravalho, E.G., Tien, C.L., and Caren, R.P., "Effect of Small Spacing on Radiative Transfer between Two Dielectrics," *J. Heat Transfer*, vol. 89, pp. 351-358, 1967.
- Cubukcu, E., Aydin, K., Ozbay, E., Foteinopoulou, S., and Soukoulis, C.M., "Subwavelength Resolution in a Two-Dimensional Photonic-Crystal-Based Superlens," *Phys. Rev. Lett.*, vol. 91, pp. 207401/1-4, 2003.
- Edwards, D.F., in *Handbook of Optical Constant of Solids* (E. Palik, ed.), Academic Press, New York, pp. 547-570, 1985.

- Engheta, N., "An Idea for Thin Subwavelength Cavity Resonators Using Metamaterials with Negative Permittivity and Permeability," *IEEE Antenn. Wireless Propag. Lett.*, vol. 1, pp. 10-13, 2002.
- Foteinopoulou, S., Economou, E.N., and Soukoulis, C.M., "Refraction in Media with a Negative Refractive Index," *Phys. Rev. Lett.*, vol. 90, pp. 107402/1-4, 2003.
- Fu, C.J., and Zhang, Z.M., "Transmission Enhancement Using a Negative-Refraction Layer," *Microscale Thermophys. Eng.*, vol. 7, pp. 221-234, 2003.
- Fu, C.J., Zhang, Z.M., and Tanner, D.B., "Enhanced Radiation Tunneling of a Multilayer Structure with a Left-Handed Medium by Surface Plasmon Polaritons," *Proceedings of International Mechanical Engineering Congress and Exposition (IMECE 2003)*, Paper No. 41952, Washington DC, 2003.
- Fu, C.J., and Zhang, Z.M., "Prediction of Nanoscale Radiative Heat Transfer between Silicon and Silicon or Another Material," *2004 ASME Heat Transfer/Fluids Engineering Summer Conference (HT-FED2004)*, Paper No. 56332, Charlotte, NC, July 11-15.
- Gao, L., and Tang, C.J., "Near-Field Imaging by a Multilayer Structure Consisting of Alternate Right-Handed and Left-Handed Materials," *Phys. Lett. A*, vol. 322, pp. 390-395, 2004.
- Garcia, N., and Nieto-Vesperinas, M., "Left-Handed Materials Do Not Make Perfect Lens," *Phys. Rev. Lett.*, vol. 88, pp. 207403/1-4, 2002.
- Gaylord, T.K., and Linxwiler, J.N., "A Method for Calculating the Fermi Energy and the Carrier Concentrations in Semiconductors," *Amer. J. Phys.*, vol. 44, pp. 353-356, 1976.
- Gerardin, J. and Lakhtakia, A., "Negative Index of Refraction and Distributed Bragg Reflections," *Microwave Opt. Technol. Lett.*, vol. 34, pp. 409-411, 2002.
- Greffet, J.-J., Carminati, R., Joulain, K., Mulet, J.-P., Mainguy, S., and Chen, Y., "Coherent Emission of Light from Thermal Sources," *Nature*, vol. 416, pp. 61-64, 2002.
- Hebb, J.P., *Pattern Effects in Rapid Thermal Processing*, Ph.D. Dissertation, Massachusetts Institute of Technology, Cambridge, MA, 1997.
- Henderson, G.N., Gaylord, T.K., and Glytsis, E.N., "Ballistic Electron Transport in Semiconductor Heterostructures and Its Analogies in Electromagnetic Propagation in General Dielectrics," *Proc. IEEE* vol. 79, pp. 1643-1659, 1991.

- Hesketh, P.J., Zemel, J.N., and Gehart, B., "Organ Pipe Radiant Modes of Periodic Micromachined Silicon Surfaces," *Nature*, vol. 325, pp. 549-551, 1986.
- Hesketh, P.J., Zemel, J.N., and Gebhart, B., "Polarized Spectral Emittance from Periodic Micromachined Surfaces. II. Doped Silicon: Angular Variation," *Phys. Rev. B*, vol. 37, pp. 10803-10813, 1988.
- Houck, A.A., Brock, J.B., and Chuang, I.L., "Experimental Observations of a Left-Handed Material That Obeys Snell's Law," *Phys. Rev. Lett.*, vol. 90, pp. 137401/1-4, 2003.
- Joulain, K., Mulet, J.-P., Carminati, R., and Greffet, J.J., "Modification of the Thermal Emission Spectrum at Short Distances," in *Proceedings of Heat Transfer and Transport Phenomena in Microsystems Conference*, Banff, Canada, 2000.
- Joulain, K., Carminati, R., Mulet, J.-P., and Greffet, J.J., "Definition and Measurement of Local Density of Electromagnetic States close to an Interface," *Phys. Rev. B*, vol. 68, pp. 245405/1-10, 2003.
- Kaplan, S.G., and Hanssen, L.M., "FT-IR Based Ellipsometer Using High-Quality Brewster-Angle Polarizers," in *Polarization: Measurement, Analysis, and Remote Sensing II*, D.H. Goldstein and D. B. Chenault. eds., Proc. SPIE, vol. 3754, pp. 285-293, 1999.
- King, W.P., Kenny, T.W., Goodson, K.E., Cross, G., Despont, M., Dürig, U., Rothuizen, H., Binig, G.K., and Vettiger, P., "Atomic Force Microscope Cantilevers for Combined Thermomechanical Data Writing and Reading," *Appl. Phys. Lett.*, vol. 78, pp. 1300-1302, 2001.
- Kittel, C., *Introduction to Solid State Physics*, 7<sup>th</sup> ed., Chapter 10, Wiley, New York, 1996.
- Kong, J.A., *Electromagnetic Wave Theory*, 2<sup>nd</sup> ed., Wiley, New York, 1990.
- Kong, J.A., Wu, B.-I., and Zhang, Y., "Lateral displacement of a Gaussian beam reflected from a grounded slab with negative permittivity and permeability," *Appl. Phys. Lett.*, vol. 80, pp. 2084-2086, 2002.
- Kreiter, M., Oster, J., Sambles, Roy, Herminghaus, S., Mittler-Neher, S., and Knoll, W., "Thermally Induced Emission of Light from a Metallic Diffraction Grating, Mediated by Surface Plasmons," *Opt. Commun.*, vol. 168, pp. 117-122, 1999.
- Krishnan, A., Thio, T., Kim, T.J., Lezec, H.J., Ebbesen, T.W., Wolff, P.A., Pendry, J.B., Martin-Moreno, L., and Garcia-Vidal, F.J., "Evanescently Coupled Resonance in Surface Plasmon Enhanced Transmission," *Opt. Commun.*, vol. 200, pp. 1-7, 2001.



- Kumar, A.R., Boychev, V.A., Zhang, Z.M., and Tanner, D.B., 2000, "Fabry-Perot Resonators Built with  $\text{YBa}_2\text{Cu}_3\text{O}_{7-\delta}$  Films on Si Substrates," *J. Heat Transfer*, vol. 122, pp. 785-791, 2000.
- Kutateladze, S.S., Rubtsov, N.A., and Bal'tsevich, Ya. A., "Effect of Magnitude of Gap between Metal Plates on Their Thermal Interactions at Cryogenic Temperatures," *Soviet Physics-Doklady*, vol. 8, pp. 577-578, 1979.
- Lakhtakia, A., "On Perfect Lenses and Nihility," *Int. J. Infrared Millimeter Waves*, vol. 23, pp. 339-343, 2002.
- Lakhtakia, A. "On Planewave Remittances and Goos-Hänchen Shifts of Planar Slabs with Negative Real Permittivity and Permeability," *Electromagnetics*, vol. 23, pp. 71-75, 2003.
- Leskova, T.A., Maradudin, A.A., and Simonsen, I., "Scattering of Electromagnetic Waves from the Random Surface of a Left-Handed Medium," in *Surface Scattering and Diffraction for Advanced Metrology*, Z.-H. Gu and A.A. Maradudin, eds., Proc. SPIE, vol. 4447, pp. 6-16, 2001.
- Leskova, T.A., Maradudin, A.A., and Simonsen, I. "Coherent Scattering of An Electromagnetic Wave from, and Its Transmission through, a Slab of a Left-Handed Medium with a Randomly Rough Illuminated Surface," in *Surface Scattering and Diffraction III*, Z.-H. Gu and A.A. Maradudin, eds., Proc. SPIE, vol. 5189, pp. 22-35, 2003.
- Liu, L., Caloz, C., Chang, C.-C., and Itoh, T., "Forward Coupling Phenomena between Artificial Left-Handed Transmission Lines," *J. Appl. Phys.* Vol. 92, pp. 5560-5565, 2002.
- Loomis, J.J., and Maris, H.J., "Theory of Heat Transfer by Evanescent Electromagnetic Waves," *Phys. Rev. B*, vol. 50, pp. 18517-18524, 1994.
- Loschialpo, P.F., Smith, D.L., Forester, D.W., and Rachford, F.J., "Electromagnetic Waves Focused by a Negative-Index Planar Lens," *Phys. Rev. E*, vol. 67, pp. 025602/1-4, 2003.
- Lu, W.T., Sokoloff, J.B., and Sridhar, S., "Refraction of Electromagnetic Energy for Wave Packets Incident on a Negative-Index Medium is Always Negative," *Phys. Rev. E*, vol. 69, pp. 026604/1-5, 2004.
- Mandel, L., and Wolf, E., *Optical Coherence and Quantum Optics*, Cambridge University Press, UK, 1995.

- Markoš, P., and Soukoulis, C.M., "Transmission Studies of Left-handed Materials," *Phys. Rev. B*, vol. 65, pp. 033401/1-4, 2001.
- Marquier, F., Joulain, K., Mulet, J.-P., Carminati, R., and Greffet, J.-J., "Engineering Infrared Emission Properties of Silicon in the Near Field and the Far Field," *Opt. Commun.*, vol. 237, pp. 379-388, 2004.
- Mulet, J.-P., Joulain, K., Carminati, R., and Greffet, J.-J., "Nanoscale Radiative Heat Transfer between a Small Particle and a Plane Surface," *Appl. Phys. Lett.*, vol. 78, pp. 2931-2933, 2001.
- Mulet, J.-P., Joulain, K., Carminati, R., and Greffet, J.-J., "Enhanced Radiative Heat Transfer at Nanometric Distances," *Microscale Thermophys. Eng.*, vol. 6, pp. 209-222, 2002.
- Müller-Hirsch, W., Kraft, A., Hirsch, M.T., Parisi, J., and Kittel, A., "Heat Transfer in Ultrahigh Vacuum Scanning Thermal Microscopy," *J. Vac. Sci. Technol. A*, vol. 17, pp. 1205-1210, 1999.
- Narayanaswamy, A., and Chen, G., "Surface Modes for Near Field Thermophotovoltaics," *Appl. Phys. Lett.*, vol. 82, pp. 3544-3546, 2003.
- Orfanidis, S.J., *Electromagnetic Waves and Antennas* (book in progress), <http://www.ece.rutgers.edu/~orfanidis/ewa>.
- Osawa, M., "Surface-Enhanced Infrared Absorption," in *Near-Field Optics and Surface Plasmon Polaritons* (Kawata, S. ed.), Springer-Verlag, Berlin, 2001.
- Pacheco, J., Jr., Grzegorzcyk, T.M., Wu, B.-I., Zhang, Y., and Kong, J.A., "Power Propagation in Homogeneous Isotropic Frequency-Dispersive Left-Handed Media," *Phys. Rev. Lett.*, vol. 89, pp. 257401/1-4, 2002.
- Pan, J.L., "Radiative Transfer over Small Distances from a Heated Metal," *Opt. Lett.*, vol. 25, pp. 369-371, 2000.
- Parazzoli, C.G., Greigor, R.B., Li, K., Koltenbah, B.E.C., and Tanielian, M., "Experimental Verification and Simulation of Negative Index of Refraction Using Snell's Law," *Phys. Rev. Lett.*, vol. 90, pp. 107401/1-4, 2003.
- Parimi, P.V., Lu, W.T., Vodo, P., and Sridhar, S., "Imaging by Flat Lens Using Negative Refraction," *Nature*, vol. 426, pp.404, 2003.
- Park, K., Lee, B.J., Fu, C.J., and Zhang, Z.M., "Study of the Surface and Bulk Polaritons with a Negative Index Metamaterial," submitted to *J. Opt. Soc. Am. B*, 2004.

- Pendry, J.B., "Radiative Exchange of Heat between Nanostructures," *J. Phys.: Cond. Matt.*, vol. 11, pp. 6621-6633, 1999.
- Pendry, J.B., "Negative Refraction Makes a Perfect Lens," *Phys. Rev. Lett.*, vol. 85, pp. 3966-3969, 2000.
- Pendry, J.B., Holden, A.J., Stewart, W.J., and Youngs, I., "Extremely Low Frequency Plasmons in Metallic Mesostructures," *Phys. Rev. Lett.*, vol. 76, pp. 4773-4776, 1996.
- Pendry, J.B., Holden, A.J., Rubbings, D.J., and Stewart, W.J., "Magnetism from Conductors and Enhanced Nonlinear Phenomena," *IEEE Trans. Microwave Theory and Techniques*, vol. 47, pp. 2075-2084, 1999.
- Podolskiy, V.A., Sarychev, A.K., and Shalaev, V.M., "Plasmon modes in metal nanowires and left-handed materials," *J. Nonlinear Opt. Phys.* Vol. 11, pp. 65-74, 2002.
- Pokrovsky, A.L., and Efros, A.L., "Lens Based on the Use of Left-Handed Materials," *Appl. Opt.* vol. 42, pp. 5701-5705, 2003.
- Polder, D., and Van Hove, M., "Theory of Radiative Heat Transfer between Closely Spaced Bodies," *Phys. Rev. B*, vol. 4, pp. 3303-3314, 1971.
- Qing, D.-K., and Chen, G., "Goos-Hänchen Shifts at the Interfaces between Left- and Right-Handed Media," *Opt. Lett.* vol. 29, pp. 872-874, 2004a.
- Qing, D.-K. and Chen, G., "Enhancement of Evanescent Waves in Waveguides Using Metamaterials of Negative Permittivity and Permeability," *Appl. Phys. Lett.*, vol. 84, pp. 669-671, 2004b.
- Raether, H., *Surface Plasmons on Smooth and Rough Surfaces and on Gratings*, Chapter 2, Springer-Verlag, Berlin, 1988.
- Ramakrishna, S.A., Pendry, J.B., Wiltshire, M.C.K., and Stewart, W.J., "Imaging the Near Field," *J. Modern Opt.*, vol. 50, pp. 1419-1430, 2003.
- Reddick, R.C., Warmack, R.J., and Ferrell, T.J., "New Form of Scanning Optical Microscopy," *Phys. Rev. B*, vol. 39, pp. 767-770, 1989.
- Ruppin, R., "Surface Polaritons of a Left-Handed Medium," *Phys. Lett. A*, vol. 277, pp. 61-64, 2000.
- Ruppin, R., "Surface Polaritons of a Left-Handed Material Slab," *J. Phys.: Cond. Matt.*, vol. 13, pp. 1811-1819, 2001.

- Rytov, S.M., Kravstov, Yu. A., and Tatarskii, V.I., *Principles of Statistical Radiophysics*, Springer-Verlag, New York. vol.3, chapter 3, 1987.
- Shchegrov, A.V., Joulain, K., Carminati, J.-J., and Greffet, J.-J., “Near-Field Spectral Effect due to Electromagnetic Surface Excitations,” *Phys. Rev. Lett.*, vol. 85, pp. 1548-1551, 2000.
- Shelby, R.A., Smith, D.R., and Schultz, S., “Experimental Verification of a Negative Index of Refraction,” *Science*, vol. 292, pp. 77-79, 2001b.
- Shen, Y., Jakubczyk, D., Xu, F., Swiatkiewicz, J., and Reinhardt, B.A., “Two-Photon Fluorescence Imaging and Spectroscopy of Nanostructure Organic Materials Using a Photon Scanning Tunneling Microscope,” *Appl. Phys. Lett.*, vol. 76, pp. 1-3, 2000.
- Siegel, R., and Howell, J.R., *Thermal Radiation Heat Transfer*, 4<sup>th</sup> ed., Taylor and Francis, New York, 2002.
- Sihvola, A.H., Lindell, I.V., “Novel Effects in Wave Reflection from Biisotropic Media,” *Microwave Opt. Technol. Lett.*, vol. 6, pp. 581-584, 1993.
- Sipe, J.E., “New Green-Function Formalism for Surface Optics,” *J. Opt. Soc. Am. B*, vol. 4, pp. 481-489, 1987.
- Smith, D.R., and Kroll, N.E., “Negative Refractive Index in Left-Handed Materials,” *Phys. Rev. Lett.*, vol. 85, pp. 2933-2936, 2000.
- Smith, D.R., Schultz, S., Markos P., and Soukoulis, C. M. “Determination of Effective Permittivity and Permeability of Metamaterials from Reflection and Transmission Coefficients,” *Phys. Rev. B*, vol. 65, pp. 195104/1-5, 2002.
- Smith, D.R., Schurig, D., Rosenbluth, M., Schultz, S., Ramakrishna, S.A., and Pendry, J.B., “Limitations on Subdiffraction Imaging with a Negative Refractive Index Slab,” *Appl. Phys. Lett.*, vol. 82, pp. 1506-1508, 2003.
- Smith, D.Y., Shiles, E., and Inokuti, M., in: E.D. Palik (ed.), *Handbook of Optical Constants of Solids*, Academic Press, New York, vol. 1, pp. 369-406, 1998.
- Sze, S.M., *Physics of Semiconductor Devices*, Chapter 1, Wiley, New York, 1981.
- Tien, C.L., and Cunningham, G.R., “Cryogenic Insulation Heat Transfer,” *Advances in Heat Transfer*, vol. 9, pp. 349-417, 1973.
- Timans, P.J., “The Thermal Radiative Properties of Semiconductors,” in: F. Roozeboom (ed.), *Advances in rapid thermal and integrated processing*, Kluwer Academic Publishers, The Netherlands, pp. 35-101, 1996.

- Valanju, P.M., Walser, R.M., and Valanju, A.P., "Wave Refraction in Negative-Index Media: Always Positive and Very Inhomogeneous," *Phys. Rev. Lett.*, vol. 88, pp. 187401/1-4, 2002.
- Veselago, V.G., "The Electrodynamics of Substances with Simultaneously Negative Values of  $\epsilon$  and  $\mu$ ," *Sov. Phys. Usp.*, vol. 10, pp. 509-514, 1968.
- Wallis, R.F., "Introduction to Electromagnetic Surface Waves," in *Electromagnetic Surface Excitations* (Wallis, R.F., and Stegeman, G.I., eds.), Springer-Verlag, Berlin, 1985.
- Whale, M.D., and Cravalho, E.G., "Modeling and Performance of Microscale Thermophotovoltaic Energy Conversion Devices," *IEEE Trans. Energy Conversion*, vol. 17, pp. 130-142, 2002.
- Williams, C.C., and Wickramasinghe, H.K., "High Resolution Thermal Microscopy," *IEEE Ultrasonics Symposium Proceedings*, vol. 1, pp. 393-398, 1986.
- Xu, J.B., Lauger, K., Moller, R., Dransfeld, K., and Wilson, I.H., "Heat Transfer between Metallic Surfaces at Small Distances," *J. Appl. Phys.*, vol. 76, pp. 7209-7216, 1994.
- Yang, X., Wagner, D., Piosczyk, B., Koppenberg, K., Borie, E., Heidinger, R., Leuterer, F., Dammertz, G., and Thumm, M., "Analysis of Transmission Characteristics for Single and Double Disk Windows," *Int. J. Infrared Millim. Waves*, vol. 24, pp. 619-628, 2003.
- Yeh, P., "Resonant Tunneling of Electromagnetic Radiation in Superlattice Structures," *J. Opt. Soc. Am. A*, vol. 2, pp. 568-571, 1985.
- Yeh, P., *Optical Waves in Layered Media*, Chapter 2, Wiley, New York, 1988.
- Yen, T.J., Padilla, W.J., Fang, N., Vier, D.C., Smith, D.R., Pendry, J.B., Basov, D.N., and Zhang, X., "Terahertz Magnetic Response from Artificial Materials," *Science*, vol. 303, pp. 1494-1496, 2004.
- Zhang, Z.M., "Reexamination of the Transmittance Formulae of a Lamina," *J. Heat Transfer*, vol. 119, pp. 645-647, 1997.
- Zhang, Z.M., and Fu, C.J., "Unusual Photon Tunneling in the Presence of a Layer with a Negative Refractive Index," *Appl. Phys. Lett.*, vol. 80, pp. 1097-1099, 2002.
- Zhang, Z.M., Fu, C.J., and Zhu, Q.Z., "Optical and Thermal Radiative Properties of Semiconductors Related to Micro/Nanotechnology," *Advances in Heat Transfer*, vol. 37, pp. 179-296, 2003.

Zhang, Z.M., and Park, K., "On the Group Front and Group Velocity in a Dispersive Medium upon Refraction from a Nondispersive Medium," *J. Heat Transfer*, vol. 126, pp. 244-249, 2004.

Ziolkowski, R.W., and Heyman, E., "Wave Propagation in Media Having Negative Permittivity and Permeability," *Phys. Rev. E*, vol. 64, pp. 056625/1-15, 2001.

## VITA

Ceji Fu was born on June 28, 1974 in Hainan Island, China. He received his Bachelor of Science degree in Theoretical and Applied Mechanics from the University of Science and Technology of China (USTC), Hefei, Anhui in July 1997. After that, he began his graduate study at Peking University and received his Master of Science degree in Fluid Mechanics in July 2000. He came to the United States of America in August 2000 to pursue his Ph.D. study in the Department of Mechanical Engineering at the University of Florida. He transferred to the Georgia Institute of Technology in August 2002. His graduate work was partially funded by National Science Foundation. His research interests include microscale heat transfer, electromagnetic wave interactions with novel materials, fluid mechanics, etc.